An implicit Generalised Interpolation Material Point Method for large deformation and gradient elasto-plasticity

Timothy James Charlton

Thesis submitted towards the
degree of Doctor of Philosophy

Department of Engineering
Durham University
United Kingdom

March 2018

An implicit Generalised Interpolation Material Point Method for large deformation and gradient elasto-plasticity

Timothy James Charlton

Abstract

The ability to correctly capture large deformation behaviour in solids is important in many problems in geotechnical engineering such as slope failure or installation of foundations. The Material Point Method (MPM) is a computational method with particular suitability for modelling problems involving large deformations. In the MPM, a domain is modelled using a set of material points at which state variables are stored and tracked. These material points move through a fixed background grid upon which calculations take place with variables being mapped between the material points and the grid. This thesis sets out to develop the MPM as a method with potential for use in geotechnical problems.

Problems are encountered with the original MPM when material points cross between grid cells, and one solution to this is the Generalised Interpolation Material Point (GIMP) method, where material points are able to influence nodes beyond the currently occupied grid cell. Most development of the GIMP method has used an explicit approach, however there are a number of advantages of an implicit approach including larger load steps and improved error control. This thesis focuses on the development of a large deformation elasto-plastic implicit GIMP method. A way of calculating the deformation gradient consistent with the MPM is introduced and convergence is demonstrated using this method which has previously been frequently omitted from MPM research. An alternative way of updating material point domains using the stretch tensor is also proposed.

The MPM has a number of similarities to the FEM, and it is often suggested that FEM technologies are trivial to use with the MPM. The MPM can encounter localisations caused by shear banding and, to overcome this, a gradient plasticity approach previously implemented for the FEM is investigated with the GIMP method for the first time. The addition of gradient plasticity to the GIMP method introduces a length scale parameter which governs the width of these shear bands and removes the mesh dependency which is encountered with conventional approaches. It is shown that implementation is possible however, there are a number of problems that are present in the combination of the two methods which should not be overlooked in the future.

Declaration

The work in this thesis is based on research carried out in the Computational Mechanics Group, Department of Engineering, Durham University. No part of this report has been submitted elsewhere for any other degree or qualification and it is all my own work unless referenced to the contrary in the text. Parts of this work have been published in the following:

Conferences

ACME 2014 - Exeter
Oral Presentation, "A review of the Material Point Method and its links to other computational methods". Paper submitted to proceedings.
ACME 2015 - Swansea
Oral Presentation, "On the implicit implementation of the Generalised Interpolation Material Point Method". Paper submitted to proceedings.
ACME 2016 - Cardiff
Oral Presentation, "Gradient elasticity with the Material Point Method". Paper submitted to proceedings.
ECCOMAS 2016 - Crete Island, Greece
Oral Presentation, "Gradient elasticity with the Material Point Method".
MPM 2017 - Delft, Netherlands
Oral Presentation, "Gradient elasto-plasticity with the Generalised Interpolation Material Point Method". Paper submitted to proceedings.
UKACM 2017 - Birmingham
Oral Presentation, "On the implementation of gradient plasticity with the Material Point Method". Paper submitted to proceedings.

Journal Articles

T. Charlton, W. Coombs and C. Augarde, "iGIMP: An implicit Generalised Interpolation Material Point Method for large deformations", Computers & Structures, vol 190. pp. 108-125, 2017

Acknowledgements

This research was funded by the UK Engineering and Physical Sciences Research Council (EPSRC) for which I am very grateful. I would like to extend thanks to friends and colleagues, past and present, from both the Department of Engineering and Josephine Butler College, for making at least part of the last few years enjoyable. I would also like to give a special thanks to Jen for supporting me and believing in me, especially during the last few difficult months of writing this thesis. Finally, I would like to thank Dr Will Coombs and Professor Charles Augarde for their excellent supervision throughout the entirety of this PhD. Without their combined knowledge, experience, advice, encouragement and patience this work would never have been completed.

Tim Charlton
Durham, March 2018

Contents

List of Figures

List of Tables

List of Algorithms

Nomenclature & abbreviations

Abbreviations

CPDI	Convected Particle Domain Interpolation
cpGIMP	Contiguous particle GIMP
DDMP	Dual Domain Material Point
DEM	Discrete Element Method
EFG	Element Free Galerkin
FEM	Finite Element Method
FLIP	Fluid Implicit Particle
GIMP	Generalised interpolation material point
iGIMP	implicit Generalised Interpolation Material Point
MLPG	Meshless local Petrov Galerkin
MPM	Material Point Method
NR	Newton Raphson
PIC	Particle In Cell
SPH	Smoothed Particle Hydrodynamics
uGIMP	Uniform GIMP
USAVG	Update Stress Average
USF	Update Stress First
USL	Update Stress Last

Identifiers

$(\cdot)_{\mathrm{g}}$	$(\cdot)$ associated with grid node
$(\cdot)_{\mathrm{p}}$	$(\cdot)$ associated with material point
$(\cdot)_{k+1}$	Value relating to the current iteration
$(\cdot)_k$	Value relating to previous iteration
$(\cdot)^n$	Value from previously converged state
$(\cdot)^{n+1}$	Value at current load step
$\dot{(\cdot)}$	Rate of $(\cdot)$
$(\cdot)^{tr}$	Trial value of $(\cdot)$
$\Delta(\cdot)$	Increment in $(\cdot)$
$(\cdot)^{\mathrm{e}}$	Elastic component of $(\cdot)$
$(\cdot)^p$	Plastic component of $(\cdot)$

Other

δ	Dirac delta function
Ω	Problem domain
Ω_p	Material point influence domain

Scalars

c	Gradient parameter
E	Young's modulus (Pa)
f	Yield function
γ	Plastic multiplier
H	Hardening parameter
I_1	First stress invarient
J	Volume ratio
J_2	Second deviatoric stress invarient
J_3	Third deviatoric stress invarient
θ	Lode angle
l_p	Material point length
ρ	Deviatoric stress
ρ_y	Deviatoric yield stress
s	Problem surface
V_p	Material point current volume
ζ	Hydrostatic stress
χ_p	Characteristic function
∇N_g	Spatial derivative of a shape function at a point
∇S_{vp}	Spatial derivative of a GIMP weighting function at a point
ν	Poisson's ratio
ξ	Local coordinate

Vectors

$\{\varepsilon\}$	Strain vector

$\{f_b\}$	Body force
$\{f^{\text{ext}}\}$	External force
$\{f^{\text{int}}\}$	Internal force
$\{f^R\}$	Residual force
$\{h\}$	Hermitian shape functions
$\{p\}$	Laplacian of Hermitian shape functions
$\{\sigma\}$	Cauchy stress vector
$\{t\}$	Applied tractions
$\{u\}$	Displacement
$\{X\}$	Vector of original coordinates
$\{x\}$	Vector of updated coordinates
$\{\tilde{X}\}$	Coordinates at start of step
$\{\Lambda_g\}$	Nodal values of plastic multiplier
$\{\tau\}$	Kirchhoff stress

Matrices

$[I]$	Identity matrix
$[B]$	Strain displacement matrix
$[b]$	Left Cauchy-Green strain
$[C^e]$	Elastic compliance matrix
$[D^{alg}]$	Algorithmic tangent
$[D^{cst}]$	Consistent tangent modulus
$[D^e]$	Elastic stiffness matrix
$[F]$	Deformation gradient matrix
$[G]$	Strain displacement matrix
$[J]$	Jacobian
$[K_{aa}]$	Standard part of stiffness matrix
$[K_{a\lambda}]$	Coupling stiffness matrix
$[K^e]$	Element stiffness matrix
$[K_{\lambda\lambda}]$	Plastic multiplier stiffness matrix
$[K_p]$	Material point stiffness
$[L^p]$	Plastic velocity gradient
$[N]$	Nodal shape functions
$[R]$	Rotational component of deformation gradient
$[s]$	Deviatoric stress matrix
$[S_{vp}]$	GIMP weighting functions
$[U]$	Right stretch matrix
$[V]$	Left stretch matrix
$[x]$	Current coordinates
$[\varepsilon]$	Logarithmic strain
$[\sigma]$	Stress matrix

Operators

$(\cdot)^T$	Transpose of $(\cdot)$
det $[\cdot]$	Determinant of $(\cdot)$
diag $[\cdot]$	Values from leading diagonal of $[\cdot]$
$[\cdot]^{-1}$	Inverse of $[\cdot]$
$[L]$	Differential operator
$\nabla^2(\cdot)$	Laplacian of $(\cdot)$
$\partial(\cdot)$	Partial derivative of
$(\cdot)^T$	Transpose
tr $[\cdot]$	Trace of $[\cdot]$
$\varphi(\cdot)$	Motion
$(\cdot)_{,x}$	derivative of $(\cdot)$ with respect to x

Chapter 1

Introduction

When modelling engineering problems it is often necessary to account for how a change in geometry will affect a structure's response. There are numerous methods for the modelling of continuum solid mechanics problems. Most of these can be described as either Eulerian or Lagrangian with each taking a different approach to accounting for the evolving geometry. Eulerian methods work by having a mesh that is fixed in space and allowing particles to move within it. This approach is more commonly used in fluid mechanics applications and it is difficult to deal with history dependent variables often required in solid mechanics. With this method it is also difficult to apply boundary conditions if the physical domain does not align with the mesh. Lagrangian methods work by splitting a problem into elements, and throughout any deformation this discretisation follows the problem domain. This is advantageous in terms of the tracking of history dependent variables and boundaries as the position, in relation to other elements, is always maintained. However the method has the drawback that with large enough deformations the mesh can become distorted. These large deformations can result in a heavily distorted mesh which, in certain situations, can cause issues with accuracy or result in calculations being unable to be completed.

The Finite Element Method (FEM) is by far the most popular method that is used for computational stress analysis by engineers. The FEM adopts a Lagrangian formulation which, although effective for a large number of situations, encounters problems due to severe mesh distortion with high deformations. Many problems in geotechnical engineering involve extremely large deformations, some examples of these include penetration of

objects into soils, such as installation of piles, slope failures and landslides. Because the behaviour of these problems involve large deformations, it is essential that the methods used to model them are able to handle this without the level of deformation being limited by mesh distortion.

One group of techniques that have recently gained much enthusiasm is known as mesh-free methods. Here a problem is modelled using particles rather than a mesh, this eliminates the mesh distortion problem. Many of these mesh-free methods are computationally expensive. One of the reasons for this is that it is often necessary to recalculate nearest neighbour particles as the values at particles can depend on the values of all other particles within a given radius. This is different to the FEM where the element topology is usually only calculated at the beginning of an analysis. One such mesh-free method which doesn't require this is the Material Point Method (MPM). The MPM combines Eulerian and Lagrangian methods by modelling a material with Lagrangian particles that move through a fixed Eulerian background grid with the aim of keeping the positives of each without the drawbacks. The use of the fixed background grid removes this neighbour searching expense which is present in many other mesh-free methods having only to search for which particles reside in an element, which is simplified further with the choice of a regular background grid.

The MPM models problems over a number of load steps using particles (or material points) at which state variables such as stress, deformation gradient and plastic strains are kept and tracked throughout a simulation. Unlike other mesh-free methods the MPM solves the equilibrium equations on a background grid. These calculations on the background grid can be seen as the same as a step in the FEM but with the material points used as integration points instead of the traditional Gauss quadrature. This leads to the description of the MPM being a FEM where the Gauss points move with the deformation. During each load step state variables are mapped to and from grid nodes and material points; however, this grid can be reset after each step. This means that, as long as the deformation within a single load step does not cause problematic mesh distortion, the restriction on movement is removed thus making it an ideal method for large deformation problems.

This similarity to the FEM is seen as a major advantage in the MPM over other

mesh free methods as many technologies that have been developed for the FEM have the possibility of being used in the MPM.

However, this similarity with the FEM has sometimes resulted in a lack of the same level of rigour in ensuring accuracy of the numerical method being applied to the MPM. In many cases the MPM as a numerical method is presented without demonstrating satisfaction of equilibrium and convergence towards analytical solutions.

Since its inception as a method for solid mechanics there have been numerous developments in the MPM. Much of the research that has taken place has been addressing the grid crossing phenomenon, looking at errors introduced by the movement of material points between elements. The effect on integration caused by the movement of material points has also been investigated. Although a variety of solutions have been proposed, no individual method has gained enough enthusiasm to be universally accepted in the MPM community. Despite this, the recent trend is for work in the MPM to be focused on applications. These have included application to the modelling of granular materials, fluid-structure interactions, and geotechnical problems such as pile installation and modelling of slopes as mentioned above. Often the demonstration of modelling these problems consists of comparing results visually against experimental results, and although good agreement is often observed this lacks the validation and verification which would typically be expected in a numerical method. The range of papers presented at the 2017 MPM conference [149] highlight this fact that a large focus within the MPM community is on applications rather than developing the fundamentals of the method. Four further points which have received less attention than they might otherwise have done are listed below:

- The imposition of boundary conditions can indeed be the same as in the FEM but this is only when the problem domain aligns with the background grid. When this is not the case the same problems that arise in other mesh-free methods arises; there has been work on boundary condition enforcement in the MPM [19, 45], however there is no agreed general way to impose boundary conditions.

- The MPM is chosen for its ability to model large deformation problems, however many research papers on the subject do not present their finite deformation formulation or instead utilise an incremental small strain solution within each step. An incorrect formulation could lead to lack of convergence to equilibrium within each

step and use of an incremental small strain solution will due to the very nature of it, be unable to converge towards either a small strain or full finite deformation solutions.

- A specific example of a problem encountered frequently in geotechnical problems is localisations caused by shear banding. This has been tackled in a variety of different ways in the FEM which leads to statements such as in [186]: "*the proposed method [MPM] is based on a FEM formulation, the same regularisation techniques as used in FEM can be used to address this issue*". One of the suggested methods here is through the use of gradient theories, the combination of which with MPM has not been done yet.

- The focus of the majority of research on the MPM has been using an explicit approach. While some work has been done on implicit approaches to MPM, it is under represented in the overall development of the method. Specifically, until work done by the author [30] there was no implementation of an implicit large deformation, elasto-plastic Generalised Interpolation Material Point (GIMP) method.

The focus of this thesis will be on the latter three of these four points and aims to develop the MPM as a numerical method capable of handling large deformations suitable for geotechnical problems. This includes developing a finite deformation formulation suitable with the MPM and investigating the implementation of gradient methods used in FEM with the MPM. There will be specific detail on constitutive aspects needed for both large strain and localisation problems and the integration associated with these.

1.1 Thesis Outline

This thesis consists of the following chapters which can be split into three sections:

- The first section will present relevant background information and an introduction to the MPM which will then be built upon further in the remainder of the thesis.

  Chapter 1, this Chapter has presented an overall introduction to the thesis, including an outline of the choice of MPM as a numerical method for use with geomechanical problems and identification of areas of improvement in current MPM research.

Chapter 2 will present an introduction to the MPM including a detailed review of relevant existing work and the implementation of an implicit, incrementally linear elastic MPM to allow demonstration of the method in the simplest possible way.

- The second part of this thesis will introduce the new developments. Each Chapter here will begin by extending the theory leading to the development of an implicit Generalised Interpolation Material Point (iGIMP) method. This method will then be verified using numerical examples with analytical solutions.

  Chapter 3 will extend the MPM to an iGIMP method and introduce a finite deformation framework that is compatible with the reference states available in the MPM.

  Chapter 4 will extend the work in Chapter 3 to large deformation elasto-plasticity including linearisation of the equilibrium equations to ensure optimum convergence of the implicit solver.

  Chapter 5 will introduce a gradient plasticity method that has previously been used in the FEM as a way of allowing mesh-independent modelling shear bands with the iGIMP method.

- The final part of the thesis sees the methods developed in Chapters 3-5 demonstrated on further numerical examples and conclusions will be drawn.

  Chapter 6 demonstrates the large deformation elasto-plastic iGIMP method working for further numerical examples. Examples also highlight issues encountered in the combination of gradient plasticity with MPMs which were not evident from the examples in Chapter 5.

  Chapter 7 presents conclusions of the thesis and makes recommendations for future work.

1.2 Notation

Throughout this thesis, in order to be as clear as possible, the majority of quantities will be displayed in matrix/vector notation, denoted with $[\cdot]$ and $\{\cdot\}$ respectively. Any deviations

from this convention will be expressed in the text. All numerical methods used in this thesis were developed and run in MATLAB. MATLAB was chosen for its advantages in making it easy to develop new algorithms and debug code; there was no focus on optimising individual algorithms or parallelisation for use in large problems, and for this reason this thesis contains no direct comparisons in terms of speed. Where applicable, all notation in this thesis adopts a tension positive convention as is common within the solid mechanics community.

Chapter 2

The Material Point Method

The Material Point Method (MPM) has established itself as a useful computational method for numerous applications in solid mechanics particularly those involving large deformations and non-linearity. This chapter will present an overview of developments in the MPM since its inception in Section 2.1 and an outline of the implementation of the MPM for linear elasticity in Section 2.2 as a base for introducing geometric and material non-linearity in Chapters 3 and 4.

2.1 Review of the Material Point Method

The MPM was first developed by Sulsky *et al.* [168, 171] as an extension to solid mechanics of the Fluid Implicit Particle (FLIP) method [20, 21], which itself was an extension to the Particle In Cell (PIC) method [62] used in fluid dynamics. In the PIC method, presented by Evans and Harlow [62], a domain is split into a number of particles representing a fluid. Each particle is assigned a mass and position and moves with a Lagrangian description of motion. The domain is also divided into a number of background cells forming an Eulerian mesh which the particles travel through. Information from the particles is interpolated to this background mesh. This same idea is used in the FLIP method where each particle is assigned all properties of the fluid including momentum and energy. The extension to solid mechanics by Sulsky *et al.* [168], now referred to as the MPM, allows solids to be similarly represented by particles (or material points). The difference to FLIP is that, to allow models with history-dependent variables to be easily implemented, the full stress tensor and any history dependent variables are carried by the material points. This results

in a method that combines advantages of both Lagrangian and Eulerian methods, allowing history dependent variables to be tracked while not encountering the problems associated with mesh distortion in large deformation problems seen in other methods such as the Finite Element Method (FEM).

2.1.1 Initial development of the MPM

When a material exhibits geometric or material non-linearity, one approach is to linearise the problem and solve incrementally over a series of time or load steps. When modelling a problem over multiple steps there is a choice to be made whether to use an explicit or implicit scheme which affects how the governing partial differential equation is solved. Initially the MPM was constructed with an explicit formulation and much early work on the method also adopted this approach [14, 170, 197, 207]. Since then, the majority of previous research on development of the method [13, 33, 78, 121, 154, 155, 189], extensions to the method [11, 23, 34, 72, 85, 89, 91, 104, 105, 123] and applications of the MPM [38–40, 71, 79, 80, 87, 88, 99–101, 107, 120, 135, 153, 169, 188, 192, 194, 200, 204, 205] have also focused on explicit formulations. Here, the solution for the next step is based only on values at the current step and equilibrium is not directly enforced. An advantage of the explicit scheme is that the inversion of the stiffness matrix is not required meaning each load step is less computationally expensive than with an implicit approach. However, the scheme relies on a suitably small time step to ensure stability and to achieve results with desired accuracy. The explicit approach is useful for dynamic problems where the duration of the simulation is small, this means that the total number of load steps required does not become excessive. In [13] it was noted by Bardenhagen that although mass and momentum are conserved in the MPM, energy conservation is not explicitly enforced and errors exist associated with this. The differences in updating stresses at the beginning or end of a step were also explored, demonstrating the effect of Update Stress First (USF) and Update Stress Last (USL) algorithms. It was concluded that neither of the two methods give better results for an unknown problem, however it is stated that the USL experiences a higher dissipation of energy where as in the USF interpolation error cancels out algorithm error. Buzzi *et al.* [24] reiterated that USF approach is a better option due to the better conservation of energy. Nairn introduced the Update Stress Average (USAVG) algorithm, which is an average of the USF and USL methods leading to a more accurate result [135].

An implicit formulation of the MPM was first introduced by Cummins and Brackbill in [48] to advance the work in the modelling of granular materials. This allowed larger time steps than in previously implemented explicit methods. In implicit formulations the solution for a step is based both on the previous step but also the solution of the current step being found. Iterations within each step ensure that equilibrium is achieved. The result of this is that the restriction of small time steps is removed, however this does come at the cost of each individual step being more expensive. The advantages of adopting an implicit approach also include improved stability and error control, in comparison to explicit methods. Following on from the work of Cummins and Brackbill, Guilkey and Weiss developed another implicit integration approach for the MPM [76], which has been shown to achieve superior accuracy when compared to explicit MPM schemes. It can be seen clearly in this approach that the implicit MPM and implicit FEM have much in common. Because of this, for static stress analysis problems, which are often tackled using an implicit FEM, it is beneficial to use an implicit MPM approach. Sulsky and Kaul evaluated and used implicit MPM in [166] again reporting the method to be more efficient than the explicit method. Other examples of implicit MPMs include [17, 77, 186] as well as a method labelled as a "Lagrangian Integration Point Finite Element formulation" which is based on implicit MPM [131] where geological problems with extremely large deformations are modelled, and [115, 116] where conservation of momentum and energy within the MPM are investigated.

2.1.2 Grid crossing error

In the standard MPM, for both implicit and explicit schemes, a problem can arise when a material point crosses the boundary between one background grid cell and another. This is due to the fact that shape function derivatives are not continuous between elements and this results in incorrect stresses being calculated when material points cross between elements. This problem is well documented in the literature and is often referred to as the grid crossing error, as errors are introduced to values at material points. It can be seen in Figure 2.1 how the highlighted material point in the top left element crosses into the element below after deformation. This causes a sudden change in which element it contributes stiffness to. There has been a large amount of work on reducing this error

and there are a selection of methods that have been proposed to address this issue and improve the MPM. These methods are largely based around modifying the properties of the material points themselves or by modifying the underlying grid basis functions. A study separating these errors from errors relating to quadrature and choice of explicit time step was performed in [163].

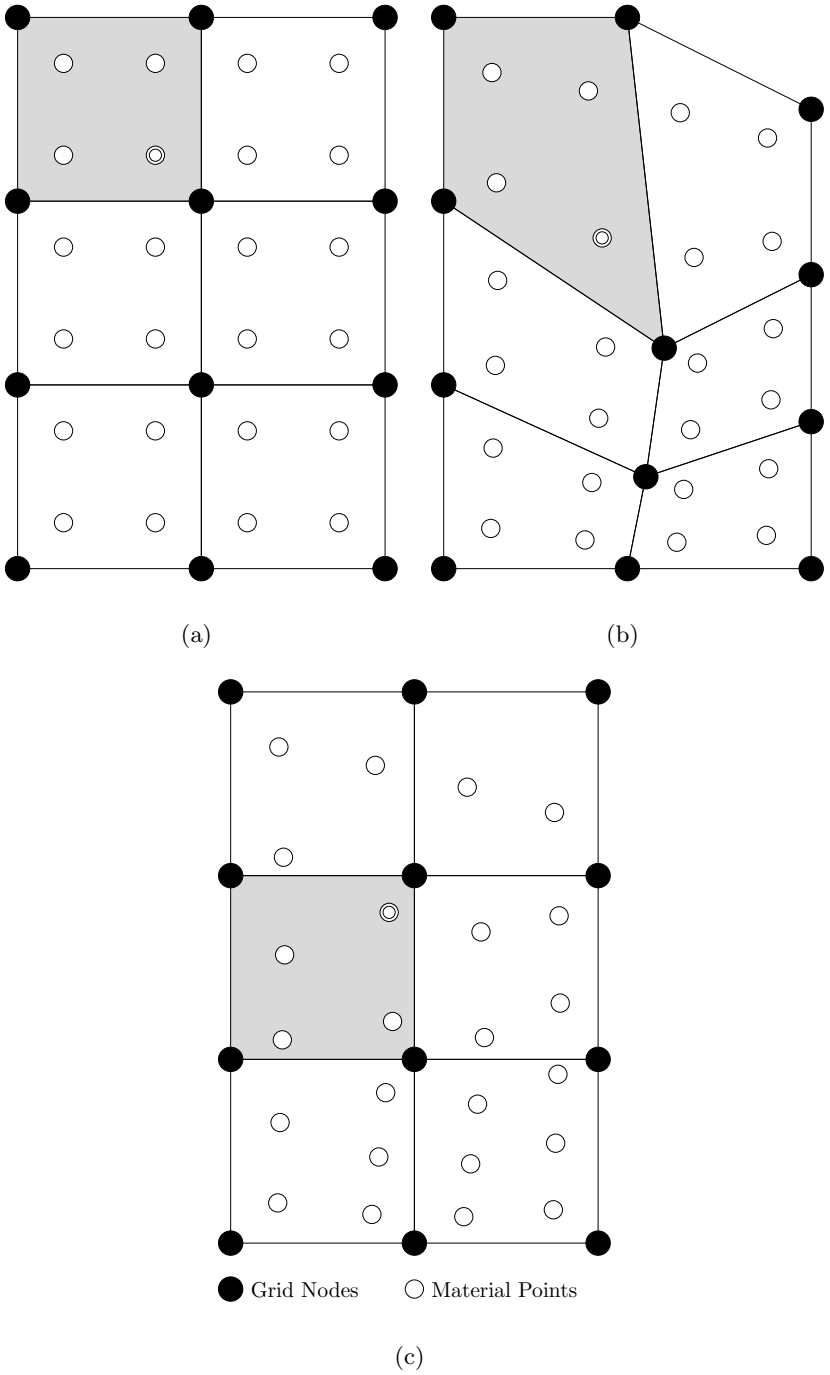

Figure 2.1: Grid crossing in MPM shown with (a) initial undeformed grid, (b) deformed grid and (c) reset grid with updated material point positions.

The Generalised Interpolation Material Point (GIMP) method

A major advance in the MPM was made in [15] where the Generalised Interpolation Material Point (GIMP) method was introduced in an attempt to reduce the erroneous stress oscillations caused by grid crossing. To alleviate some of the error caused by this problem, the GIMP method introduces an area or volume associated with each individual material point which can be seen in Figure 2.2. These "influence domains" are described by material point characteristic functions which will be covered further in Chapter 3. This change from the standard MPM means that it is possible that a material point can influence nodes other than those associated with the element it is inside. This occurs when the material point is close enough to the edge of an element that the domain overlaps adjacent elements. The introduction of the GIMP method is shown in [15], for mechanics problems, to give an improved stress response compared to the MPM. It was seen in this example, that as material points cross element boundaries in the MPM there was an increasing deviation from the analytical solution due to spurious stress oscillations, however in the GIMP this was not the case. It is also shown that it is possible to derive the original MPM as a special case of the GIMP method by replacing the particle characteristic function with the Dirac delta function, reducing the domain of the material point to a discrete point.

In [162] it is shown however that the GIMP method only offers a partial remedy to the errors introduced when material points cross element boundaries. In that paper the quadrature errors within the MPM are investigated and it is shown the underlying problem is not completely removed by the GIMP method as it does not change the underlying basis functions in general. Despite this, the GIMP method offers a considerable improvement, worthy of investigation.

Previous research into the GIMP method has also almost exclusively used an explicit approach, for example [1, 4, 6, 7, 12, 15, 24, 49, 119, 160, 180, 182, 183] with one notable exception [133] where the GIMP method is implemented implicitly using a Jacobian free Newton-Krylov method for dynamic problems using hyperelasticity. The explicit integration methods used in the GIMP method were evaluated by Guilkey and Wallstedt [183], where it was confirmed that the GIMP method is most accurate when material points remain contiguous and non-overlapping. The GIMP method has recently been implemented

in an implicit manner [30] for both elastic and elasto-plastic large deformation problems. This approach will be detailed further in Chapters 3 and 4.

At the end of each load step there is an opportunity to update the introduced influence domains of the material points. Two variations were presented in [183] labelled uniform Generalised Interpolation Material Point (uGIMP) and contiguous particle Generalised Interpolation Material Point (cpGIMP). In uGIMP particle domains are assumed to not change in size or shape throughout a simulation as indicated in Figure 2.2(a). This is the simplest approach to take, however, it can result in many of the particle domains overlapping with each other or separating. In the cpGIMP approach the particle domains evolve based on the diagonal components of the deformation gradient so they continue to be rectangular. This rectifies the problem when deformation is aligned with the background grid but still causes problems when material rotations occur; a simple modification to this will be proposed in Chapter 3.

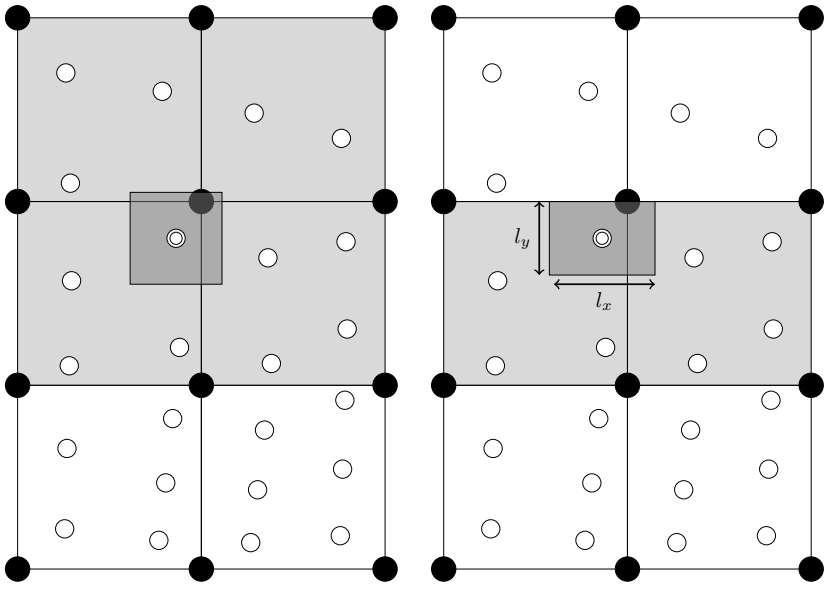

Figure 2.2: Material point influence domains in (a) uGIMP and (b) cpGIMP.

Convected Particle Domain Interpolation (CPDI) method

The Convected Particle Domain Interpolation (CPDI) method can be thought of as an extension of the cpGIMP method. First developed by Sadeghirad *et al.* [151], the technique also improves the MPM by specifying particle domains associated with material points

and updating them after each loadstep. In the CPDI method material point domains are initially rectangular but are allowed to deform into parallelograms, thus removing the limitation that exists with the standard GIMP method when rotations occur, this can be seen in Figure 2.3(a). A further extension allows material point influence domains to evolve into more general quadrilaterals (in 2D) which is achieved by tracking the domain corners as shown in [133, 152]. This ensures that the material point influence domains remain contiguous throughout the simulation, this can be seen in Figure 2.3(b). To achieve this the CPDI method includes an additional approximation in the way that the basis functions of a material point are determined: a linear approximation between domain corners is used to obtain the integration of the shape functions over each particle domain. Because of this, errors can be introduced when the corners of the particle domain are in different elements. This does not occur in the GIMP method as the basis functions are calculated analytically. CPDI methods where the rectangular domains can be extended to polygons have also been investigated in [140]. The popularity of the CPDI method has recently gained momentum and has been used in a number of studies including cracking [86], axisymmeteric problems [81, 138] and saturated porous media [206].

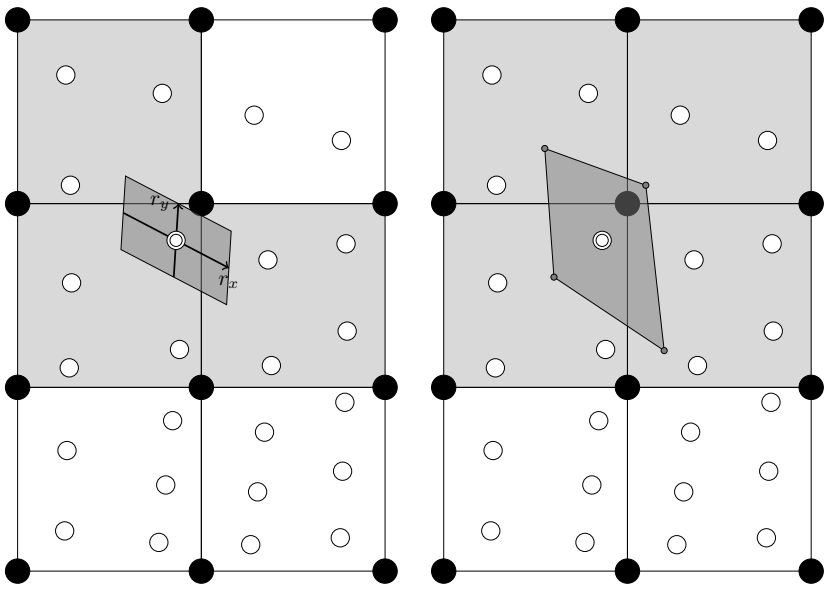

(a) (b)

Figure 2.3: Material point influence domains in (a) CPDI and (b) CPDI2.

Dual Domain Material Point (DDMP) method

Another alternative method to the GIMP method was proposed in [201], and is referred to as the Dual Domain Material Point (DDMP) method. The objective was still to address the instability caused by material points crossing grid element boundaries. In the DDMP method, material points also influence neighbouring background grid cells, however the way this is done is different as only the gradients of shape functions are altered meaning that the material points have different influence domains for quantities relating to a gradient than those not. This helps to alleviate some problems encountered when it is necessary to track material point domains. In [22] the DDMP is modified to utilise second order functions and has also been used for representing ductile damage [114]. A comparison of the above methods is given in [56] using a simple one-dimensional shock problem as an example.

Other modifications to the MPM

The grid crossing error exists due to the fact that the shape function derivatives are not continuous between elements therefore another possible way to reduce this error is using higher order continuity basis functions. Implementation choices within the MPM are examined in [161] where the use of B-splines as basis functions is investigated. Andersen and Andersen investigated the possibility of using different interpolations including quadratic elements and cubic splines [5]. It was stated that for large deformation problems, where the MPM is particularly advantageous, the use of C^0 quadratic elements becomes limited due to the partially negative shape functions present resulting in the sign of the mass used (in the explicit dynamic formulation) interpolated to the grid nodes changing for some nodes. Higher order basis functions have recently been implemented for implicit [132] and explicit [176] MPM both showing excellent improvement over the standard MPM.

Wallstedt and Guilkey presented a method based on MPM and GIMP in [181] that used weighted least squares and was claimed to have superior accuracy to both GIMP and MPM however suffers from being more complex to implement than the MPM and GIMP method. In another alternative approach [186] implicit MPM was used, however rather than tackling the instabilities using GIMP, an additional non-physical stiffness term was introduced. Although this improves the numerical stability of the method, it destroys its

ability to converge to the original analytical solution.

2.1.3 Improving the MPM

In addition to addressing the grid crossing error there are several other problems that have been identified when using the MPM. A solution mitigating shear and volumetric locking was developed by Mast and co-workers [125]. It was identified that the problem that can occur in the MPM; however, errors caused by this are often hidden due to the grid crossing instability error dominating. Another new method for updating Material Points that reduces noise and enhances stability has been proposed in [84]. Another problem which can occur in the dynamic, explicit, formulation related to small masses on nodes near material interfaces was investigated by Ma *et al.* [121]. An algorithm is presented to prevent the numerical instability associated with this.

The accuracy of the MPM is linked to the discretisation of the background grid, however to refine the whole grid when deformation is local can be unnecessarily expensive. Work by Lian *et al.* [106] describes a method allowing for a grid to have local refinement for problems with extreme localised deformation. When selecting the size of the background grid in the MPM it is necessary to know the position of the final material. This causes a problem when modelling a body in a domain where the deformation is unknown beforehand such as landslides and debris flow. A technique for managing the mesh in these situations was proposed in [155].

Dealing with boundaries

Applying boundary conditions in the MPM has been claimed to be more straightforward than in many other meshless methods due to the existence of the background grid meaning that boundary conditions can be applied directly to grid nodes. There is a significant flaw in this that this is only the case if the material boundary is, and remains, aligned with the chosen background grid.

One approach to impose boundary conditions is using a multi-grid method is used in [174] with the GIMP method for modelling coupled thermo-mechanical processes. This method effectively refines the grid at the boundaries but would not help if the domain did no align with the grid. More recently, a novel approach for MPM, based on implicit boundaries is given in [46] and a B-spline based approach is investigated in [19].

An alternative method which reduces the need for implementing boundary conditions not aligned with the grid is to utilise what is known as a moving mesh approach [163]. This seems counterintuitive as distorting the mesh appears to remove the advantage the MPM has over the FEM, however it is not necessary for the moving mesh to be fixed to the material points. The moving mesh method has been implemented for modelling the installation of displacement piles [145, 146] and screw piles [187].

Addressing computational expense

A criticism of the MPM (as with many other mesh free methods) is its increased computational expense when compared to mesh-based methods such as the FEM, which is especially noticeable in three dimensional simulations. The additional steps of identifying material point locations and mapping to and from the grid mean that for large analyses the MPM can have very long run times. This is amplified in some explicit methods where a very large number of load steps are required. Because of this, several authors have attempted to speed up the MPM. An object-oriented MPM framework has been proposed in [122] to help speed up the MPM, and more recently the MPM has been implemented in Julia [158] which uses a similar syntax to MATLAB but with significant speed ups. Parallelisation strategies have been introduced along with a mesh-grading method in [103] and applied to the CPDI method for fracture problems in [86]. The MPM has also been adapted for GPU acceleration in [37] and [57]. Although many of these methods are of use when running large simulations in three dimensions, the MPM does not have the same neighbour searching expenses of many meshless methods making smaller investigations possible in reasonable timeframes.

2.1.4 Applications of the MPM

Throughout its development, the MPM has been used in a wide range of applications, many of which specifically make use of the large deformation capabilities of the MPM.

Granular materials

One area that the MPM has been applied to is the modelling of granular materials. First presented in [14], models based on continuum representations are solved for macroscopic granular particles in a manner that allows modelling of interactions between these grains as well as internal deformations. Granular materials were modelled in [48] using an implicit

formulation of the MPM showing advantages including, as stated above, i.e. the ability to use larger time steps than explicit approaches. The collapse of a granular column under gravity was modelled in [124, 159] as well as in [64, 65] where the focus was on the failure mechanisms when using more complicated constitutive models including partial saturation. A fully coupled hydro-mechanical MPM for saturated dense granular materials is also used in [108].

Fluid and solids

The ability to model both fluid and solid parts of a soil is necessary in many applications, and because of this it is an area which has attracted much focus within the MPM community. There have been two main schools of thought on implementing this within the MPM framework, the first of which is to have a coupled approach where there is a single set of material points. In work by Colom [41] a coupling between mechanical and hydraulic aspects is presented, allowing interaction between a soil skeleton and pore water to be modelled for saturated porous media. A two phase soil and pore water model is also demonstrated in [91] as well as in [27, 28] where cone penetration tests are modelled. Zabala and Alonso used the MPM to model the progressive failure of the Aznalcollar dam in Spain [200] where hydro-mechanical coupling was used to deal with pore water in a saturated soil. The model was then compared to the actual observed failure of the dam. As well as two phases of soil and water, it is also possible to model partially saturated soils by considering the air voids. Higo *et al.* coupled the MPM with the Finite Difference method to analyse air-water-soil three-phase porous media [85], to allow the modelling of partially saturated soils. The soil skeleton was modelled using the MPM with the pore water pressure stored at the centre of each grid element. This version of the MPM where each material point is used for all three-phases was also employed in [196].

A different approach to modelling hydro-mechanical problems is taken by Abe *et al.* [1]. Here the soil and water particles are both modelled by their own sets of material points, and by computing movements of fluid particles in the soil the water table location can be changed. Modifications are made to this by Bandara to allow modelling of partially saturated soils [10] and the degree of saturation of the soil can be altered by simulating rainfall. The two particle formulation has also been used in [11]. The approach of having a separate set of material points for each material has also been used in modelling saturated

porous media [204] and study at multiphase flow problems [123]. The two approaches are compared in [3] where it is stated that the single-particle two-phase MPM formulation is more efficient than the two-particle formulation, however when a single layer of material points is considered the mass conservation of water is not guaranteed, whereas both masses are conserved using the two layer formulation.

The MPM is also used in [202] to model multiphase flow problems and in [72] to model fluid structure interactions. When solving problems involving fluids there is a limitation when materials exhibit incompressibility, this was addressed using the MPM in [203] and [96].

Geotechnics

Many geotechnical problems will involve complexities of both granular materials and fluid-soild interactions. Additionally, the nature of geotechnical problems such as slopes and landslides means that large displacements and nonlinear material behaviour are a regular occurrence, particularly if one is interested in post failure behaviour. In mesh-based methods such as the FEM this causes problems due to the distortion of elements often requiring re-meshing. As grid distortion is not an issue in the MPM it has proved to be a popular tool for modelling landslides and because of this has attracted a large amount of attention.

Landslides and slope stability problems have been modelled using the MPM in a number of papers. In [7] the stress distribution before collapse is shown to agree with a FEM analysis and the ability of the MPM to model large deformation post failure behaviour highlights the usefulness of the method in being able to model interactions of this slope failure with a building. The capability of the MPM to handle both initialisation and post failure run out behaviour is also highlighted in [195]. It was shown in [58] that a MPM analysis of a submarine landslide was able to match a large deformation finite element analysis which used re-meshing and in [185] different failure modes of slopes were demonstrated, both of these papers acknowledged that there was dependency of the solution on the background mesh. In the modelling of seismic slope failure, [18] utilised additional particles to model the moving boundary. Slope failure was also investigated using MPM in [63] and in [184] where the MPM was combined with random field theory.

In addition to the modelling of landslides and slope failures the MPM has been used

in a number of other geotechnical applications. Settlement in landfills was modelled in [207] using the MPM stating that the large deformation nature of the problem can cause problems in FEM analyses. A 'partition method' is also introduced where material points cross boundaries in a more gradual manner. A quasi-static formulation of the MPM (suitable for situations where loading is slow enough that time and inertial effects can be ignored) was used in [16] for problems including modelling a retaining wall. In this approach elements that are fully filled with material points are integrated using standard Gauss quadrature, with only those partially filled elements using the material points for this purpose. Wieckowski in [189] also modelled a retaining wall along with a selection of other large strain problems such as cutting and granular flow and like many other studies found the MPM's ability to not suffer the mesh distortion of the FEM appealing. The larger computation time required was stated as a disadvantage albeit one which could possibly be addressed with parallelization. Coetzee *et al.* [40] used the MPM to model anchors in soil and pull out tests that are difficult to model using FEM, and compared these results to experimental work. The MPM is compared against modelling using the Discrete Element Method (DEM) in two papers [39] and [38], for uses in excavator bucket filling and soil cutting respectively. In [82] the MPM was used for modelling of the release of geocontainers from a barge.

Other applications

A contact algorithm for granular material using the MPM was introduced in [78]. Contact has also been investigated for the MPM in [191] where a multi mesh approach is used, in [89] to improve simulations of impact and penetration and in [99] where adhesive contact was modelled. A geo-contact algorithm for contact between structural elements and soil, for uses in geotechnical engineering [119] allows for rough contact; this is to reduce oscillations that previously occurred when materials of varying stiffness were in contact. A frictional contact algorithm for the implicit MPM was proposed in [35]. Another area that has caused interest in the MPM is the modelling of cracks and fractures in materials. The MPM is particularly suited to these analyses compared to fully mesh based methods as the fracture path is unconstrained by the mesh. The MPM has been applied to this area by a number of authors [12, 49, 71, 79, 80, 86, 93, 135, 136, 139, 173]. Contact fracture are beyond the scope of this thesis and will not be discussed beyond this paragraph.

The MPM has also been used for a large number of other applications. These applications include modelling of sea ice dynamics [169], gas dynamics [180], modelling of spur gears [87], dynamic material failure [32, 167], high velocity impact [112], explosions [88, 107, 144, 188, 192], biomechanics [77, 90], modelling materials for use in animation [164, 165], modelling of membranes [83, 193, 197, 198], heat transfer [75, 174], cutting [4, 137], composite materials [134, 153, 194], chemical/mechanical coupling [74] and modelling of foams [199].

2.1.5 The MPM combined with other methods

Key advantages of the MPM include its ability to handle large deformations without element distortion. This however comes at the additional expense of mapping variables to and from the background grid and identifying which element material points are in. Sometimes only a section of a problem may benefit from these advantages and it is often undesirable to model an entire problem using the MPM in this case. In situations like this, the user is faced with a choice: whether another method would be more suited to the particular application or if there is a possibility to combine existing methods together.

FEM

The MPM has many similarities with the standard FEM [33]. In fact it is possible to think of the MPM as a finite element method with moving integration points instead of fixed Gauss points in each element. The shape functions used to map between the grid and the material points in the standard MPM are the same as the shape functions used in the FEM . If material points are located at the positions of Gauss points in the FEM and if the mesh is not reset after each step then the MPM becomes identical to the FEM. A version of the FEM known as the press replace method is compared against the MPM for jacked piles in [175]. This method works by repeatedly displacing a finite element mesh by a pre-specified amount and replacing a slice of soil material by pile material while assuming small strains and is not suitable for the wide range of problems that the MPM can be used for.

A coupling between the MPM and the FEM was introduced in [205] using the FEM to model a problem while taking advantage of the MPM for areas with large deformation. Coupling of MPM and FEM was also implemented by Lian *et al.* [104, 105] and improved

on in [36].

Mesh-free methods

It is possible to make comparisons between the MPM and other mesh-free methods such as the Meshless Local Petrov Galerkin (MLPG), Element Free Galerkin (EFG) and Smoothed Particle Hydrodynamics (SPH) methods. One key advantage that the MPM has over many of these mesh-free methods is that there is no need for a specific search to locate nearest neighbours to define nodal connectivity. Instead, use can be made of the element topology of the background grid and this can make the MPM less computationally expensive than the other methods. Particle weighting functions are often needed to calculate the support and influence of each points in mesh-free methods whereas the background grid is used for this in MPM. There are many texts on the topic of mesh-free methods in general such as [102, 110, 111] and it is not the focus of this review.

SPH [118] is one particular Lagrangian meshfree method that has received attention in MPM publications. In SPH the domain is represented by a set of distributed particles needing no connectivity, rather than a set of nodes based around elements in a grid. Functions at these points are approximated and smoothed as a weighted average over neighbouring particles using a kernel function which weights contributions based on density and distance from the point of interest. There have been a number of comparisons between MPM and Smoothed Particle Hydrodynamics (SPH) [120, 147, 172] where the key advantages of the MPM was been reinforced as not requiring a computationally expensive particle searching algorithm. The ability to apply boundary conditions directly to the grid is also given as an advantage however this is only the case if the boundaries in question align with the grid. [3] compares a number of computational methods for landslide type problems including mesh-free methods and concluded that although there were many geotechnical tools for prediction of failure there is often little information about the post failure response needed to assess catastrophic damage. A coupled analysis using MPM could be useful here however an incorporation of unsaturated soil models would be needed for modelling landslides more accurately.

Modelling at multiple scales

Being a continuum method the MPM does not account for explicit modelling of a microstructure of a material. One way in which work has been undertaken to facilitate this is through multi-scale modelling. Here the MPM is combined with other methods that concentrate on a much smaller scale such as molecular dynamics [31, 34, 92, 117]. The advantage of using a coupled MPM approach here is the ability to model larger problems. Many methods that focus on a smaller scale are so computationally expensive they cannot be applied to any but the smallest of problems. The MPM has also been combined with the Discrete Element Method (DEM) [109] where each material point is used as a representative volume element.

An alternative way to incorporate a measure of the underlying microstructure of a material is to account for non-local effects such as has been investigated in [23, 73]. The use of a non-local methods is useful for removing the mesh dependancy which occurs in certain problems such as shear bands and singularities. Another method for accounting for material structure is using gradient methods. This has not previously been developed within the MPM and will be explored further in Chapter 5.

2.2 Material Point Method implementation

In order to explain the methodology of the MPM in more detail, an outline of the problem to be solved will be introduced. This section will begin with linear elasticity as a the most basic theory of describing material deformation before showing an example using the MPM.

2.2.1 Linear elasticity

When a stress is applied to a solid material, the material will undergo a deformation or strain. In situations where this applied stress is less than the amount which would cause a material to yield it behaves elastically. This means that when the stress is removed, the material will return to its original shape. In many real world problems deformations can be complex and displacements large. However, as a starting point, for small deformations and infinitesimal strains an approximation can be made that the stress is linearly related to the stress. This linear elastic relationship between stress and strain can be expressed

as

$$\{\sigma\} = [D^{\mathrm{e}}]\{\varepsilon\}. \tag{2.1}$$

Working in a 3D cartesian frame (x,y,z), $\{\sigma\}$ is the Cauchy stress vector,

$$\{\sigma\} = \begin{Bmatrix} \sigma_{xx} & \sigma_{yy} & \sigma_{zz} & \sigma_{xy} & \sigma_{yz} & \sigma_{zx} \end{Bmatrix}^T, \tag{2.2}$$

$[D^e]$ is the elastic material stiffness matrix which is given as

$$[D^e] = \frac{E}{(1+\nu)(1-2\nu)} \begin{bmatrix} (1-\nu) & \nu & \nu & 0 & 0 & 0 \\ \nu & (1-\nu) & \nu & 0 & 0 & 0 \\ \nu & \nu & (1-\nu) & 0 & 0 & 0 \\ 0 & 0 & 0 & (1-2\nu)/2 & 0 & 0 \\ 0 & 0 & 0 & 0 & (1-2\nu)/2 & 0 \\ 0 & 0 & 0 & 0 & 0 & (1-2\nu)/2 \end{bmatrix}, \tag{2.3}$$

where E is the Young's Modulus and ν is Poisson's ratio. $\{\varepsilon\}$ is the strain vector

$$\{\varepsilon\} = \begin{Bmatrix} \varepsilon_{xx} \\ \varepsilon_{yy} \\ \varepsilon_{zz} \\ \varepsilon_{xy} \\ \varepsilon_{yz} \\ \varepsilon_{zx} \end{Bmatrix} = \begin{Bmatrix} \frac{\partial u}{\partial x} \\ \frac{\partial v}{\partial y} \\ \frac{\partial w}{\partial z} \\ \frac{\partial u}{\partial y} + \frac{\partial v}{\partial x} \\ \frac{\partial v}{\partial z} + \frac{\partial w}{\partial y} \\ \frac{\partial w}{\partial x} + \frac{\partial u}{\partial z} \end{Bmatrix} \tag{2.4}$$

where u, v and w are the components of the displacement vector $\{u\}$.

For a body to be in equilibrium, the forces applied must be balanced by stresses within the material. Taking $\{f_b\}$ to be body force per unit volume in each direction, and defining the differential operator matrix $[L]$, as

$$[L]^T = \begin{bmatrix} \frac{\partial}{\partial x} & 0 & 0 & \frac{\partial}{\partial y} & 0 & \frac{\partial}{\partial z} \\ 0 & \frac{\partial}{\partial y} & 0 & \frac{\partial}{\partial x} & \frac{\partial}{\partial z} & 0 \\ 0 & 0 & \frac{\partial}{\partial z} & 0 & \frac{\partial}{\partial y} & \frac{\partial}{\partial x} \end{bmatrix}, \tag{2.5}$$

equilibrium of a body can be written as

$$[L]^T\{\sigma\} + \{f_b\} = \{0\}. \tag{2.6}$$

MPM discretisation

The MPM discretises a problem into a set of Lagrangian material points which move through an Eulerian background grid made up of connected nodes. In this thesis, where appropriate, quantities associated with grid nodes will be identified $(\cdot)_{\mathrm{g}}$ and those at material points will be identified $(\cdot)_{\mathrm{p}}$. The material points carry all the necessary information including the stresses and their current global positions. This information is then mapped to the background grid where calculations are carried out and the new values are then mapped back to the material points. To be able to interpolate from the grid nodes to the material points and vice versa, nodal shape functions must be introduced. A straightforward choice would be linear Lagrange shape functions as used in linear finite elements. Each background grid element is given a set of local coordinates ξ in a domain from -1, +1 in each direction.

The remainder of this thesis employs a plane strain approach, by assuming all strains in an out of plane direction to be zero. Many problems can be modelled by only considering two dimensions or for simple examples one dimension. The shape functions N for a given position within the element can then be given for nodes i=1,2 for a 1D, 2-noded line element as

$$N_i = \frac{1 \pm \xi}{2} \tag{2.7}$$

The matrix $[N]$ contains the values of the shape functions associated with each node once for each dimension. Using these shape functions, the displacement $\{u\}$ at any point within the element can be calculated from a set of nodal displacements $\{u_g\}$ at grid nodes through

$$\{u\} = [N]\{u_{\mathrm{g}}\}. \tag{2.8}$$

Using the shape functions and the differential operator in (2.5) it is possible to write the strain displacement matrix $[B]$ which contains the derivatives of the shape functions with

respect to the global coordinates ($[N_{,x}]$) as

$$[B] = [L][N] \tag{2.9}$$

Using (2.8), the definitions of strain in (2.4) and the strain displacement matrix, it is possible to say that

$$\{\varepsilon\} = [B]\{u_{\mathrm{g}}\}. \tag{2.10}$$

In practice it is only possible to analytically determine the derivatives with respect to the local coordinates ($[N_{,\xi}]$). To transform between the two sets of coordinates it is necessary to compute the Jacobian matrix $[J]$,

$$[J]^T = \frac{\partial x_{\mathrm{g}}}{\partial \xi} = [N_{,\xi}][x_{\mathrm{g}}] \tag{2.11}$$

where $[x_{\mathrm{g}}]$ are the current coordinates of the grid nodes. It is then possible to calculate the derivatives of shape functions with respect to global coordinates through application of the chain rule

$$[N_{,x}] = [J]^{-T}[N_{,\xi}]. \tag{2.12}$$

By substituting (2.10) into (2.1) and this into (2.6) the strong form of equilibrium can be found to be

$$[L]^T[D^e][L][N]\{u_{\mathrm{g}}\} + \{f_b\} = \{0\}. \tag{2.13}$$

Multiplying the strong form by a test function $\{c\}^T$ and integrating over the volume of an element Ω gives the weak form

$$\int_\Omega \{c\}^T[L]^T[D^e][L][N]\{u_{\mathrm{g}}\}d\Omega + \int_\Omega \{c\}^T\{f_b\}d\Omega = 0. \tag{2.14}$$

By applying the Gauss-Green theorem to the first term in (2.14) it is possible to obtain

$$\int_S \{c\}^T[D^e][L][N]\{u_{\mathrm{g}}\}\{n\}dS - \int_\Omega (\{c\}[L])^T[D^e][L][N]\{u_{\mathrm{g}}\}d\Omega + \int_\Omega \{c\}^T\{f_b\}d\Omega = 0. \tag{2.15}$$

Applying the same discretisation to $\{c\}$ as $\{u\}$ and replacing $\{c\}$ with $[N]\{a\}$, where $\{a\}$

are nodal values, it is possible rearrange (2.15) and arrive at

$$\int_{\Omega}[B]^{T}[D^{e}][B]d\Omega \ \{u_{\mathrm{g}}\} = \int_{S}[N]^{T}\{t\}dS + \int_{\Omega}[N]^{T}\{f_{b}\}d\Omega, \tag{2.16}$$

where $\{t\}$ are traction forces equal to $[\sigma]\{n\}$ and $\{n\}$ are normals to the surface. This weak form can be written more concisely as

$$[K]\{u_{\mathrm{g}}\} = \{f_{\mathrm{g}}\}, \tag{2.17}$$

where $[K]$ is the global stiffness matrix and $\{f_{\mathrm{g}}\}$ are nodal forces made up of external tractions and body forces. This global stiffness matrix and global force vector can be assembled from contributions from background grid elements to obtain the equation that needs to be solved for $\{u_{\mathrm{g}}\}$ in the MPM. The integration in (2.16) is performed numerically using the material points as quadrature points and will be described in more detail in the next section.

2.2.2 MPM algorithm

At the beginning of a MPM analysis it is necessary to define the problem domain by specifying the background grid nodal coordinates and the initial particle positions. In regard to choosing the background grid, it is not restricted to any particular shape however it can be useful for it to be made of regular uniform elements for ease of initial location of material points within each grid element. The grid must also extend to where any material points are expected to move into during the simulation. Fixed boundary conditions can be applied directly to grid nodes at this point.

The initial material point locations can also be chosen freely however it is desirable to locate material points equally within background elements as this simplifies identifying how much volume should be associated with each material point and therefore its weight. Each material point is assigned a volume V_p based on the volume of material it represents in the global coordinate system as shown in Figure 2.4. In the standard MPM the weight (or volume) associated with each material point is fixed and stays with the particle throughout the simulation.

For linear elastic problems it is not usually necessary to model over a number of load

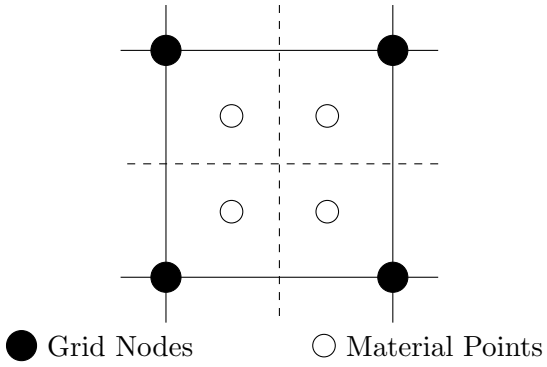

Figure 2.4: Four material points in a 2D element each with a weight equal to a quarter of the element area.

steps, however to demonstrate the MPM in its full capacity it will be assumed that the simulation will be split over a number of steps. The result of this is a method which, although linear within a step, over multiple load steps begins to account for finite deformations. This is due to the geometry being constantly updated as material points move. With this in mind, the first thing that is necessary to do in a load step is to identify which background grid elements contain which material points.

Particle element locations

To identify in which element each material point is currently located has the potential to be expensive. However, by keeping the background mesh a uniform grid aligned with the coordinate axis, it is possible to use a simple algorithm to calculate each particle's element by comparing the coordinate values in each dimension of with those of the background grid. For situations where this is not the case it is possible to use other more sophisticated routines, however this task then becomes more expensive than for a regular rectangular grid. As material points can move between elements it is possible to have elements containing no material points; if an element contains no material points that element is ignored from the calculations in that load step.

Local coordinate identification

Once it has been identified in which element a particle lies, it is necessary to compute the local coordinates (ξ, η in 2D) of the particle relative to the element. If the material points have been positioned at selected local coordinates originally this is trivial for the first step, however once the material points have moved the local positions within elements requires

calculation. For a regular grid aligned with the coordinate axes it is again possible to simplify this by comparing the overall global coordinates. Otherwise, to calculate this, an initial estimate is made as to the local coordinates and shape functions are calculated for this point. These shape functions are then multiplied by the grid node coordinates and compared to the actual material point global coordinates. The actual local coordinates are then iterated towards using the Newton Raphson (NR) method until correct local coordinates are converged upon (doing this with linear elements, this should converge in a single iteration due to the underlying element basis).

Mapping external forces

Once the local coordinates of a material point are known within an element, the shape functions $[N]$ can then be computed. With these, any external forces that are being applied at material points can be mapped to the background grid nodes through

$$\{f_{\mathrm{g}}^{\mathrm{ext}}\} = \sum_{i=1}^{n_{mp}} \{f_{\mathrm{p}_i}^{\mathrm{ext}}\}[N_i], \tag{2.18}$$

where n_{mp} is the number of material points in the element and N_i are the shape functions for each of the material points associated with grid nodes in that element, as shown in Figure 2.5. Body forces can be similarly mapped using

$$\{f_{\mathrm{g}}^{\mathrm{ext}}\} = \sum_{i=1}^{n_{mp}} \{f_b\}[N_i]V_i, \tag{2.19}$$

however, tractions are more difficult to apply as they require a representation of the material boundary. See [45] or [19] for further details.

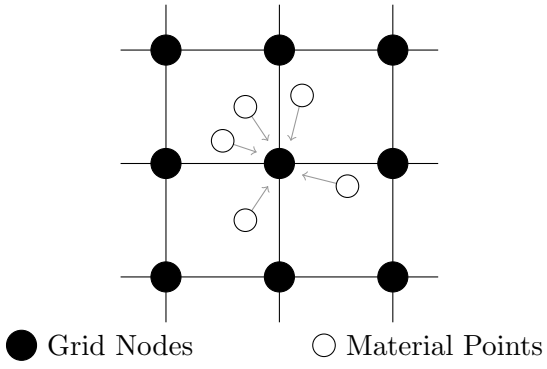

Figure 2.5: Mapping of forces from material points to grid nodes in an element in 2D.

Calculating stiffness

The element stiffness derived in (2.17) can be written as

$$[K^e] = \int_\Omega [B]^T [D^e][B] d\Omega \tag{2.20}$$

This can be approximated numerically by replacing the integral above with a summation over all material points within an element

$$[K^e] = \sum_{i=1}^{n_{mp}} [B]_i^T [D^e][B]_i V_{\mathrm{p}_i}. \tag{2.21}$$

where n_{mp} is the number of material points in the element. By adding contributions for all active elements within the domain an overall stiffness can be computed. It is now possible to solve a linear system of equations on the background grid to determine the nodal displacements.

$$[K_g]\{u_g\} = \{f_g\}. \tag{2.22}$$

From these nodal displacements strains and stresses can be calculated at material points using (2.10) and (2.1). If performing a calculation over a number of steps the strain should also be stored at each material point. The stress and strain are then updated incrementally based on the increment from the current loadstep and the total strain from previous loadsteps. Using the stress at the material points, it is then possible to calculate internal forces at grid nodes

$$\{f^{\mathrm{int}}\} = \int_\Omega [B]^T \{\sigma\} d\Omega. \tag{2.23}$$

This integral is also calculated as a summation of material points

$$\{f^{\mathrm{int}}\} = \sum_{i=1}^{n_{mp}} [B]_i^T \{\sigma\}_i V_{\mathrm{p}_i}. \tag{2.24}$$

For a linear elastic model these internal forces should balance out immediately if one were to check equilibrium with applied external forces. At the end of a loadstep the position of the material points are required to be updated. Displacements at material points can be

calculated as

$$\{u_p\} = \sum_{i=1}^{n_{\text{nodes}}} [N]_i \{u_{g_i}\}. \tag{2.25}$$

The global positions of material points are then updated by

$$\{x_p\}^{n+1} = \{x_p\}^n + \{u_p\}^n. \tag{2.26}$$

as shown in Figure 2.6. As the grid nodal positions are reset after each loadstep they are not updated here giving the newly positioned material points and the original grid as shown in Figure 2.7. A summary is given in Algorithm 2.1.

2.2.3 Numerical example

This subsection describes an initial investigation of the MPM based on the algorithm described above. Given the similarities between the MPM and the FEM the method was implemented by modifying an existing small strain finite element code [44], which allowed the overall structure to be mirrored in the implementation. The code was run with a simple example to verify its ability to model a simple problem and to demonstrate issues highlighted in the literature such as the grid crossing instability. The code was used to replicate the simple one dimensional problem of uniaxial quasi-static compression of a column under self weight presented in [15]. The column had a initial height of 50 units and a Young's modulus of $E = 10^6$ as can be seen in Figure 2.8. Gravity was applied by increasing the body force from zero to 40000 units, enough for the height of the column

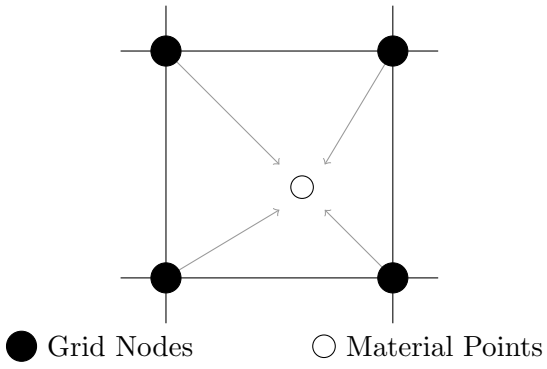

Figure 2.6: Mapping of displacments from grid nodes back to material points.

Algorithm 2.1 Implicit MPM algorithm

$lstp$	1	2	...lstps	FOR EACH Loadstep	
				Calculate which elements each particle is in, and therefore free degrees of freedom	
$\{f_{n+1}^{ext}\}$				increment and map the external forces $\{f_g^{ext}\} = \{f_p^{ext}\}[N]$	(2.19)
$nels$	1	2	$...n_{els}$	FOR EACH element	
i	1	2	$...n_{mp}$	FOR EACH Material Point	
$[B]$				strain displacement matrix $[B] = \left[\frac{\partial N}{\partial X}\right]$	(2.9)
$[K^e]$				particle contribution to element stiffness $[K^p] = [B]^T[D][B]V_p$	(2.21)
$\{\Delta u_g\}$				solve for displacements $\{\Delta u_g\} = [K]^{-1}\{f\},$	(2.22)
$nels$	1	2	$...n_{els}$	FOR EACH element	
i	1	2	$...n_{mp}$	FOR EACH Material Point	
$\{\Delta u_p\}$				particle displacement $\{\Delta u_p\} = [N]\{\Delta u_g\}$	(2.25)
$[B]$				strain displacement matrix $[B] = \left[\frac{\partial N}{\partial \tilde{X}}\right]$	(2.9)
$\{\Delta\varepsilon\}$				calculate strain increment $\{\Delta\varepsilon\} = [B]\{\Delta u_g\}$	(2.10)
$\{x_p^{n+1}\}$				update particle positions $\{x_p^{n+1}\} = \{x_p^n\} + \{\Delta u_p\}$	(2.26)
$\{\varepsilon^{n+1}\}$				update particle strains $\{\varepsilon^{n+1}\} = \{\varepsilon^n\} + \{\Delta\varepsilon\}$	

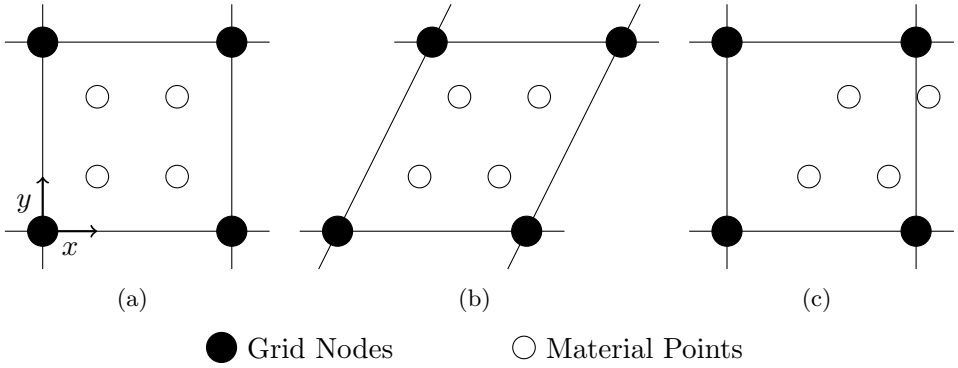

Figure 2.7: Material Point Method. Initial position of material points (a), deformed mesh and material points (b) and reset mesh with updated material points (c).

to reduce by 1 unit. The analytical solution as given in [15] is

$$\sigma(z) = E\left\{\sqrt{\frac{2\rho_0 b}{E}(\Delta - z) + 1} - 1\right\}, \tag{2.27}$$

where $\rho_0 b$ is the body force, and z is the current position in the column of current height Δ.

As the analysis is linear the correct solution can be obtained in a single step. In this situation, the MPM is identical to the FEM with the Gauss points being replaced by material points which do not necessarily have the same positions as the quadrature points. In this study the effects of a number of different factors were investigated. To begin with, the number of elements and the number of loadsteps were changed, the results of which are shown in Figure 3.6. It can be seen that when using a single loadstep, the results agreed well with the analytical solution as expected. The stepped response of the MPM is due to

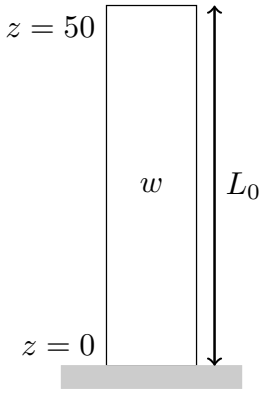

Figure 2.8: 1D column under self weight.

the linear basis functions giving a constant stress in each element (a single material point in the centre of each element would give zero error for this specific case). When increasing the number of loadsteps to 2, and further to 20, the results when modelling the problem with 10 elements do not significantly change. However, when the number of elements is larger (as shown with 100 elements) then there exist spurious oscillations in the stress response. This can be attributed to the fact that with larger numbers of elements and movement of material points possible between steps it is possible to introduce the grid crossing error that is noted in the literature [15].

To show more clearly the effect of material point grid crossing an error measure can be introduced, this is again taken from the work in [15] and is written as

$$\text{Error} = \sum_{p} \frac{|\sigma(Z_p) - \sigma_p| V_p}{W L_0}. \tag{2.28}$$

Using this error measure, the number of load steps, elements and material points were varied and the convergence was plotted. It can be seen from Figure 2.10 that changing the number of material points does not affect the accuracy in this instance due to only requiring a single point to integrate the stiffness and body force correctly. It can also be seen that for a single load step the convergence rate, the rate at which the error reduces with the increase in background grid elements, is approximately 1, the same rate that would be seen using linear finite elements. When the number of load steps is increased it is observed that for low numbers of elements, where no grid crossing occurs, the same convergence properties can be seen. When the number of elements increases to a point where grid crossing begins to occur the convergence plot plateaus. One reason for this is that by using a finer background grid additional crossing between grid elements occurs which introduces additional errors. However, this is not the only cause of the degradation of convergence rate. A key point which is often overlooked in the MPM is the fact that the formulation presented here is using an incrementally linear (but globally non-linear) algorithm to model a small strain problem. This is due to the geometry updating due to the movements of material points. Because of this it is not possible to converge towards a solution which is fully linear but it will also not converge to a fully large deformation solution due to being incrementally linear. This will be discussed further in Chapter 3.

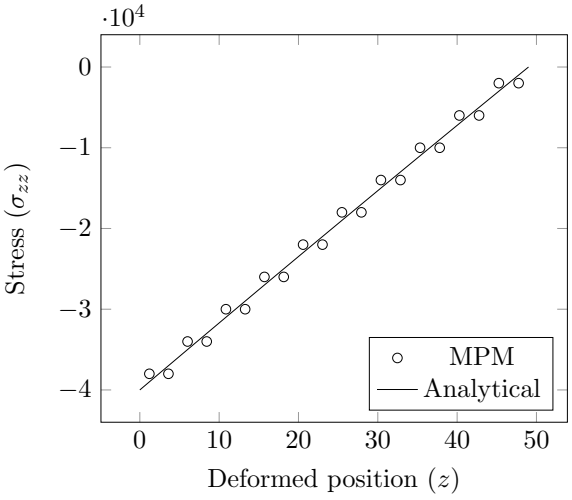

(a) 10 elements, 2MPs, 1 loadstep

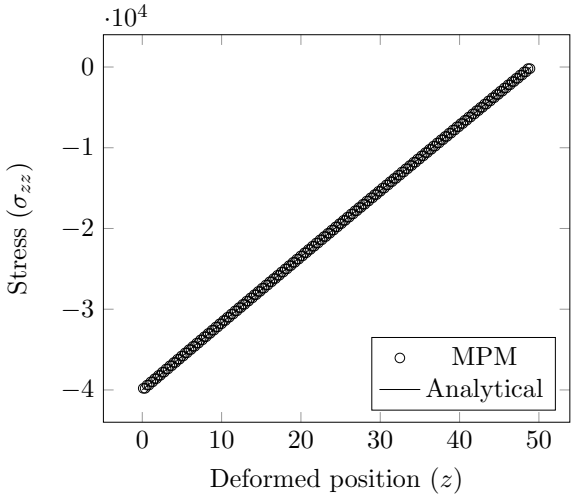

(b) 100 elements, 2MPs, 1 loadstep

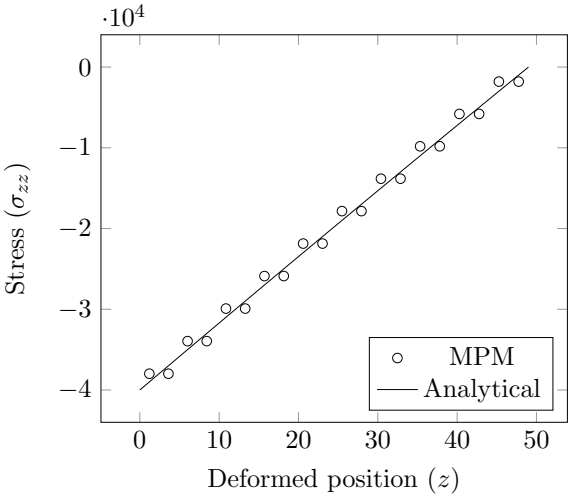

(c) 10 elements, 2MPs, 2 loadsteps

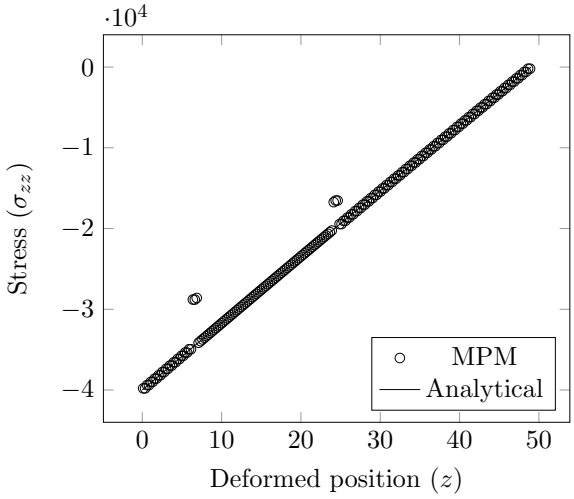

(d) 100 elements, 2MPs, 2 loadsteps

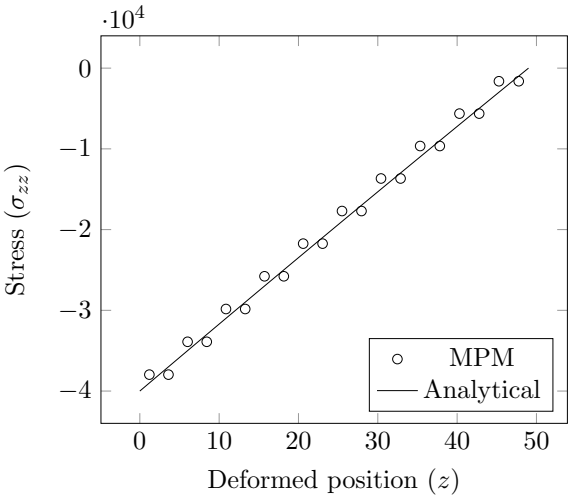

(e) 10 elements, 2MPs, 20 loadsteps

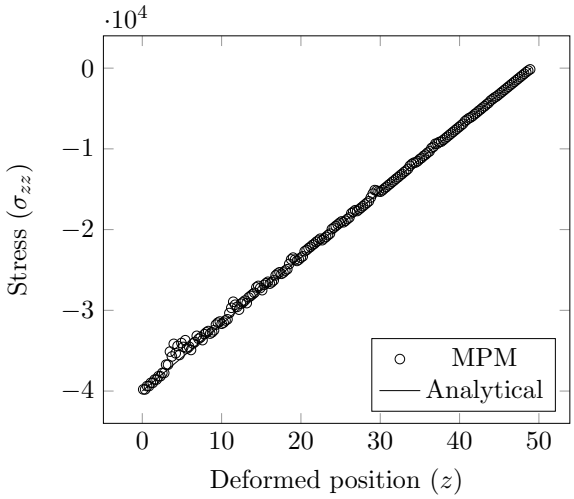

(f) 100 elements, 2MPs, 20 loadsteps

Figure 2.9: Variation of stress in a column under self weight with different loads applied, using 2 material points (MPs) per element.

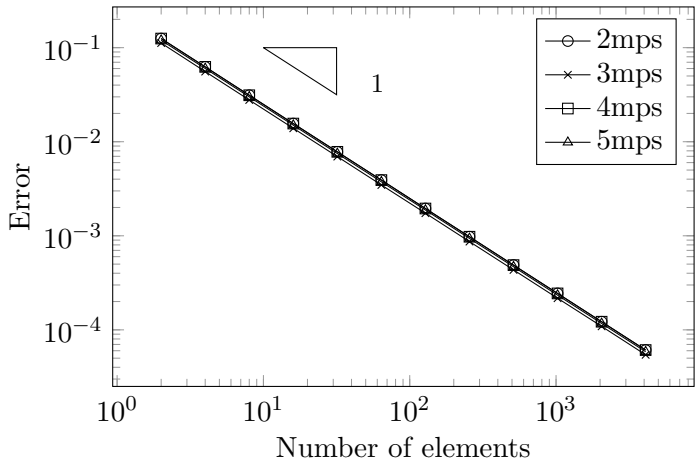

(a) 1 Loadstep

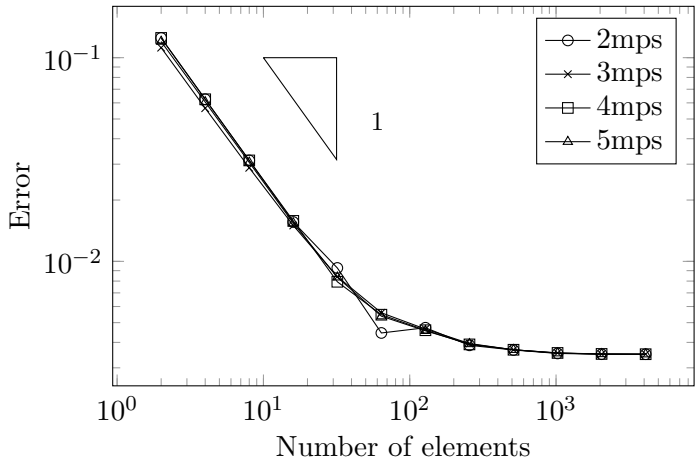

(b) 2 Loadsteps

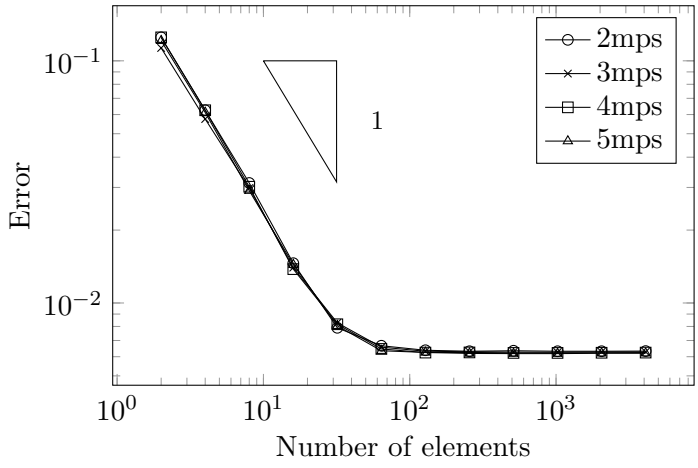

(c) 20 Loadsteps

Figure 2.10: Convergence of MPM analysis with increasing numbers of background grid elements for 2-5 material points per element for (a) 1, (b) 2 and (c) 20 loadsteps.

From these results it can be taken that the MPM can model linear elastic problems well using a single load step. This is not a surprising statement as for a single step it is equivalent to the FEM. The correct implementation of the method has been shown by achieving the correct convergence rate. For large deformation problems where the MPM will be more advantageous however, it is essential to use multiple loadsteps. It has been confirmed that for multiple load steps even for a problem modelled well in a single step the MPM introduces errors which limit overall accuracy. As discussed in Section 2.1.2 this has been previously addressed using a number of different techniques including the GIMP method.

2.3 Observations

In this chapter the background of the MPM has been discussed in detail including many of its current applications. The existence of well known grid crossing error has been highlighted from the literature. It has been shown that for linear elasticity the MPM can be implemented easily as a modification of the FEM, and it has been demonstrated that for small deformations it can provide good results. The grid crossing error that appears when material points begin to cross between element boundaries caused by more elements (or larger deformations) is also demonstrated and it is found that notable errors are introduced into the stress response which limit convergence towards an analytical solution. To combat this, the introduction of a method such as the GIMP method should be considered. It was also identified that this lack of convergence is partly down to the MPM being linear within a load step but globally non-linear meaning that it is not possible to agree with a purely linear analytical solution or a fully geometrically non-linear solution. As the advantages of the MPM lie in modelling large deformation problems a consistent non-linear finite deformation framework must be introduced. In the next chapter, the MPM formulation given in this chapter will be extended to a GIMP method including geometric non-linearity.

Chapter 3

iGIMP for large deformation elasticity

In the previous Chapter, two reasons that the Material Point Method (MPM) could not converge to an analytical solution for a simple one dimensional compression problem were identified. The first of these reasons is an error which occurs when material points move between background grid elements causing a sudden transfer of stiffness in these elements. To address this, an implicit formulation of the Generalised Interpolation Material Point (GIMP) method, originally proposed in an explicit formulation by Kober and Bardenhagen [15], will be introduced as a way of reducing the grid crossing error. The GIMP method has been chosen as it is the most straightforward way to introduce domains of influence into the MPM. The second reason the MPM would not converge to an analytical solution is that the MPM is linear within each step but non-linear globally, this means that the MPM is unable to converge to either a linear or geometrically non-linear analytical solution. To achieve convergence to a finite deformation solution a fully geometrically non-linear framework must be introduced so that the method is also non-linear within each step. In this chapter the implicit Generalised Interpolation Material Point (iGIMP) method will be introduced in Section 3.1, calculating new weighting functions and demonstrating the effectiveness of these changes. iGIMP refers to the implicit implementation of the GIMP method that is used in this thesis, GIMP does not imply the previously implemented explicit version and is used to refer to the method in general. A large deformation framework will then be derived in Section 3.2 and explained for the iGIMP method and algorithms will be

presented. The effectiveness of the geometrically non-linear iGIMP method will then be demonstrated using numerical examples in Section 3.3.

3.1 Implicit Generalised Interpolation Material Point method

The GIMP method [15] extends each material point from being a discrete point at a single location representing a volume of material to each material point having an associated area or volume in the form of an influence domain. This modification allows material points that are close enough to an element edge that the domain overlaps, to influence nodes associated with elements other than the one they are inside. These influence domains are described using a characteristic function (χ_p) which is then used to modify the shape functions. The influence domains are defined to initially cover the whole of the material with no gaps or overlaps wherever possible. A drawback of the method can be highlighted here in that if a domain has a curved or sloped boundary it is not possible to model this exactly using the GIMP method in the standard way. This is outside the scope of this thesis but useful progress on modelling boundaries in the MPM can be found in [45].

3.1.1 Shape functions

In the GIMP method the standard linear shape functions $[N_g]$ that are used in the MPM given in (2.7) are replaced by weighting functions notated as $[S_{vp}]$ to be consistent with the majority of the literature. These functions are constructed in one dimension using the existing shape functions in addition to the material point characteristic functions. To construct weighting functions in two or three dimensions, the tensor product of one dimensional functions can be taken. The most commonly used characteristic function is a top hat function with a value of unity within the material point's influence domain and zero elsewhere. This characteristic function, which is used in the development below, can be expressed as

$$\chi_p(\xi) = \begin{cases} 1, & \text{if } \xi \cap \Omega_p \\ 0, & \text{otherwise.} \end{cases} \tag{3.1}$$

where ξ is the local coordinate of the material point within an element and Ω_p is the material point's influence domain. The weighting function (S_{vp}) can then be calculated in

the local coordinate system as

$$S_{vp} = \frac{1}{V_p} \int_{\Omega_p \cap \Omega} \chi_p(\xi) N_g(\xi) d\xi, \tag{3.2}$$

where V_p is the material point volume (or length in 1D) and Ω is the problem domain. An advantage of this approach is that it is possible in the GIMP method to calculate these modified shape functions analytically whereas other methods such as Convected Particle Domain Interpolation (CPDI)[151] require additional approximations. The gradient of the weighting functions (∇S_{vp}), can also be calculated using

$$\nabla S_{vp} = \frac{1}{V_p} \int_{\Omega_p \cap \Omega} \chi_p(\xi) \nabla N_g(\xi) d\xi. \tag{3.3}$$

The standard MPM shape functions can be recovered as a special case of the GIMP shape functions by setting the characteristic function equal to the Dirac delta function, that is

$$\chi_p(\xi) = \delta(\xi) V_p. \tag{3.4}$$

This reduces the material point's influence domain to a discrete point. The GIMP weighting functions (3.2) can be thought of as being constructed in one dimension from a convolution of the linear shape functions and the characteristic function. This is shown graphically in Figure 3.1. The weighting function at a particular point can be calculated as the overlapping area between a material point's influence domain and the standard shape functions of the associated background grid node. The standard shape functions (solid lines) and GIMP weighting functions (dashed lines) are shown for a one dimensional set of adjacent nodes in Figure 3.2. The GIMP weighting functions shown use the characteristic function, χ_p as a top hat function described in (3.1). Here it can be seen how a material point contributes to not only the nodes of the element it is in but also to surrounding nodes. It can be observed that when summing the GIMP functions, they still possess partition of unity. When material point influence domains overlap multiple elements it is necessary to ensure that each material point contributes the correct amount to each node. It is possible to calculate these contributions on an element by element basis, as is done in the Finite Element Method (FEM) but it must be considered that only the part of a

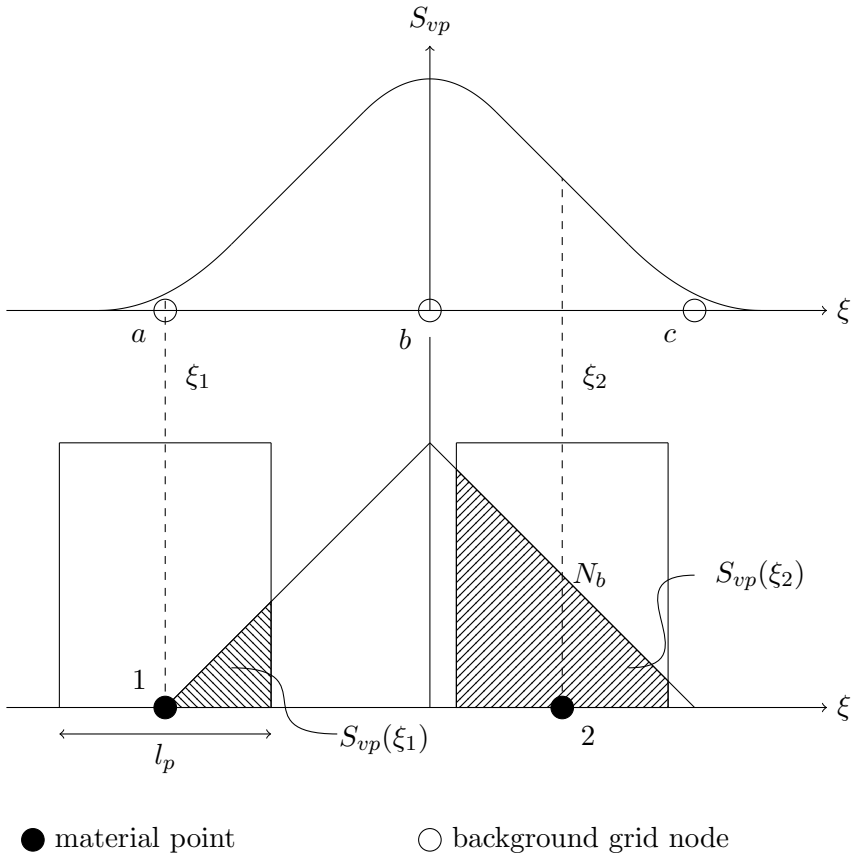

Figure 3.1: Weighting function associated with a node b shown as a convolution of the standard shape function at (N_b) and material point characteristic function χ_p, with width l_p.

material point domain which overlaps is considered. This can be achieved by constructing modified weighting functions where the integrations in (3.2) and (3.3) are only calculated over the area of each element. Figure 3.3 shows (in a similar manner as Figure 3.1) how the new functions S_{vp_a} and S_{vp_b} can be constructed from the overlapping area between the characteristic functions and the standard shape functions within an element. The weighting functions associated with the element a-b in Figure 3.3 are

$$S_{vp_a} = \frac{1}{4l_p} 2\xi_2 - \xi_2^2 - 2\xi_1 + \xi_1^2 \quad \text{and} \quad S_{vp_b} = \frac{1}{4l_p} 2\xi_2 + \xi_2^2 - 2\xi_1 - \xi_1^2, \tag{3.5}$$

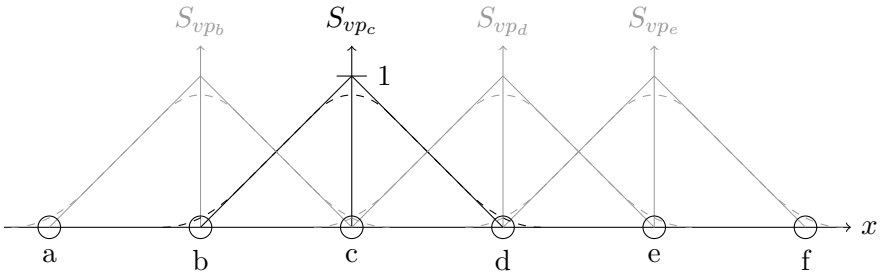

Figure 3.2: Weighting functions shown for grid nodes b, c, d and e in one dimension.

where ξ_1 and ξ_2 are the integration limits for (3.2) in the local coordinates of the current element which can be expressed as

$$\xi_1 = \begin{cases} -1, & \text{if } \xi_p - \frac{l_p}{2} < -1 \\ \xi_p - \frac{l_p}{2}, & \text{if } \xi_p - \frac{l_p}{2} > -1 \end{cases} \tag{3.6}$$

and

$$\xi_2 = \begin{cases} 1, & \text{if } \xi_p + \frac{l_p}{2} > 1 \\ \xi_p + \frac{l_p}{2}, & \text{if } \xi_p + \frac{l_p}{2} < 1 \end{cases} \tag{3.7}$$

where ξ_p is the material point location and l_p is the material point domain size. By summing these weighting functions at nodes from the contributions from different elements it is possible to recover the GIMP weighting functions as introduced earlier. This is shown in Figure 3.4, where S_{vp_b} (shown by the solid dark line) is reconstructed from contributions from elements $a-b$ and $b-c$ (shown by the dashed lines). The gradients of the weighting functions are calculated similarly using (3.3). Figure 3.5 shows the overlap between the material point characteristic function and the gradients of the standard shape functions within each element as dashed lines and the sum of these at node b shown as a solid line. It can again be seen that these functions extend beyond the element but the gradients of the GIMP shape functions are recovered when contributions from both elements are considered. The area with a constant gradient is the section where the material point's influence domain is fully inside the element; at this point it is equal to the standard linear shape functions. The gradient weighting functions for element $a - b$ in Figure 3.5 can be

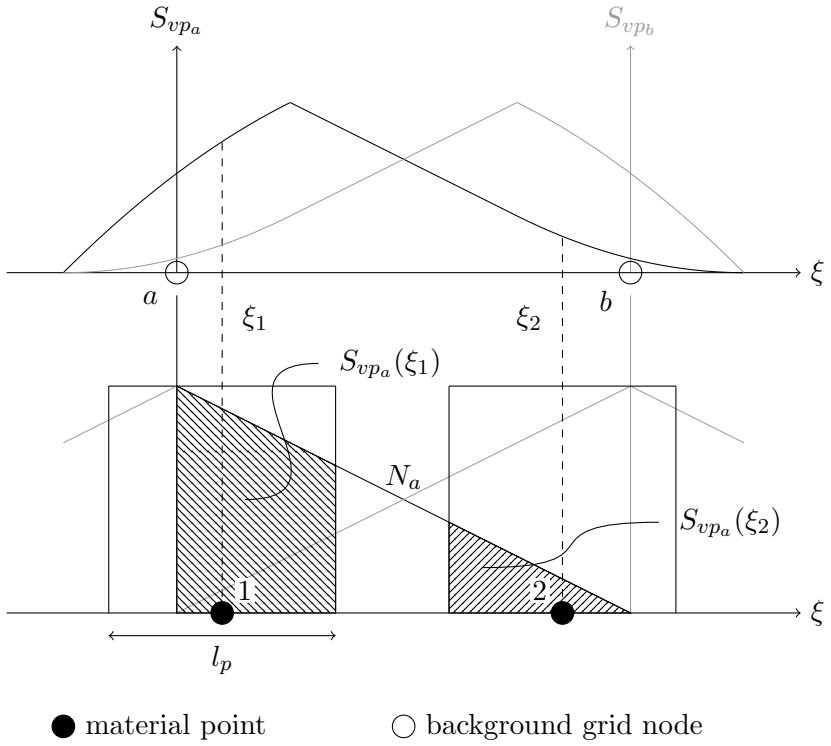

Figure 3.3: Construction of element based weighting functions shown from the convolution of the material point characteristic function with shape functions of nodes of the element.

expressed as

$$\nabla S_{vp_a} = \frac{\xi_1 - \xi_2}{2l_p} \quad \text{and} \quad \nabla S_{vp_b} = \frac{\xi_2 - \xi_1}{2l_p} \tag{3.8}$$

where ξ_1 and ξ_2 are given by (3.6) and (3.7). This means that the strain displacement matrix $[B]$ has to be constructed from each element that a material point overlaps and now is formed as.

$$[B] = \left[\left[\frac{\partial S^a_{vp1}}{\partial X} \right] \quad \left[\frac{\partial S^a_{vp2}}{\partial X} \right] + \left[\frac{\partial S^b_{vp2}}{\partial X} \right] \quad \left[\frac{\partial S^b_{vp3}}{\partial X} \right] \right]. \tag{3.9}$$

where X is the global coordinate. Other than these modifications, Equations (2.8 to 2.26) outlined in Chapter 2 remain the same with $[S_{vp}]$ replacing $[N]$. In the iGIMP method it is necessary to assemble the stiffness through material point contributions rather than element contributions; this is to ensure that terms coupling nodes in adjacent elements that are not directly connected are not ignored when material domains overlap multiple elements. The nodal stiffness components of a single material point can thus be obtained

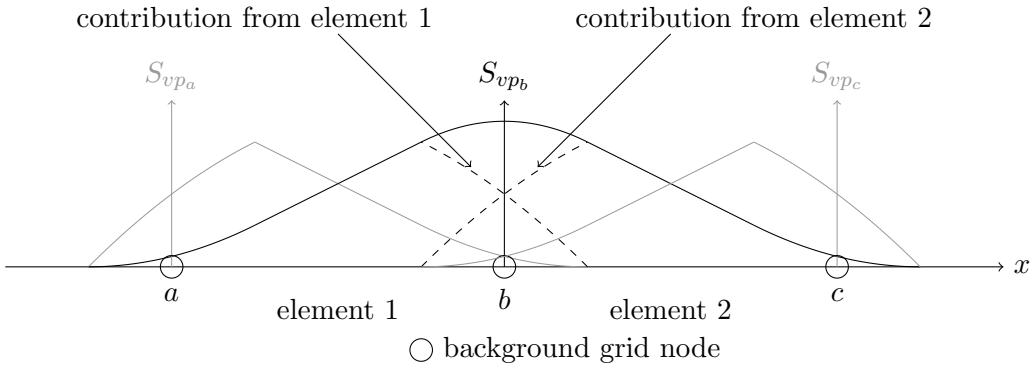

Figure 3.4: The GIMP weighting function shown for a node b constructed from the sum of the weighting functions in two elements.

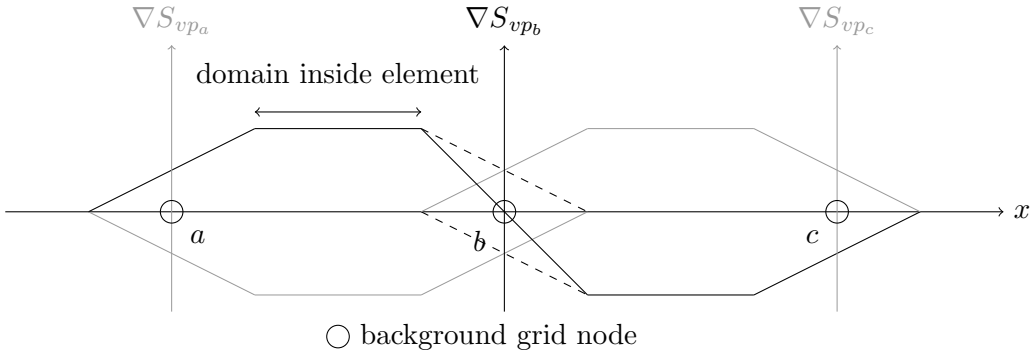

Figure 3.5: The GIMP gradient weighting function shown constructed from the sum of the gradient weighting functions in two elements.

through

$$[K_p] = [B]^T[D^e][B]V_p, \tag{3.10}$$

The algorithm for iGIMP with linear elasticity can be seen in Algorithm 3.1.

3.1.2 Numerical example

The same problem of the compression of a column under self weight, as outlined in Section 2.2.3, is modelled again, this time using the iGIMP method. The column has a height initially of 50 units and a Young's modulus of $E = 10^6$ this time modelled on a background grid split into 100 elements. The column is again compressed by increasing the body force up to 40000 units in order to reduce the height of the column by 1 unit. Figure 3.6 shows the stress variation throughout the deformed column for 2 and 20 load steps. Here it can be seen that the stress oscillations due to the grid crossing are no longer observed. This does not however fix the lack of convergence as the GIMP method is still linear within a

Algorithm 3.1 Elastic iGIMP algorithm.

$lstp$	1	2	...lstps	FOR EACH Loadstep	
				Calculate which elements each particle overlaps, and therefore free degrees of freedom	
$\{f_{n+1}^{ext}\}$				increment and map the external forces $\{f_g^{ext}\} = \{f_p^{ext}\}[S_{vp}]$	(2.19)*
i	1	2	...n_{mp}	FOR EACH Material Point	
$nels$	1	2	...n_{els}	FOR EACH overlapping element	
$[B]$				strain displacement matrix $[B] = \left[\frac{\partial S_{vp1}^a}{\partial X}\right] \dots$	(3.9)
$[K_p]$				particle stiffness $[K_p] = [B]^T[D][B]V_p$	(3.10)
$\{\Delta u_g\}$				solve for displacements $\{\Delta u_g\} = [K]^{-1}\{f\},$	(2.22)
i	1	2	...n_{mp}	FOR EACH Material Point	
$nels$	1	2	...n_{els}	FOR EACH overlapping element	
$\{\Delta u_p\}$				particle displacement $\{\Delta u_p\} = [S_{vp}]\{\Delta u_g\}$	(2.25)*
$[B]$				strain displacement matrix $[B] = \left[\frac{\partial S_{vp1}^a}{\partial X}\right] \dots$	(3.9)
$\{\Delta\varepsilon\}$				calculate strain increment $\{\Delta\varepsilon\} = [B]\{\Delta u_g\}$	(2.10)
$\{x_p^{n+1}\}$				update particle positions $\{x_p^{n+1}\} = \{x_p^n\} + \{\Delta u_p\}$	(2.26)
$\{\varepsilon^{n+1}\}$				update particle strains $\{\varepsilon^{n+1}\} = \{\varepsilon^n\} + \{\Delta\varepsilon\}$	

Equations marked with a * indicate where $[N]$ has been replaced by $[S_{vp}]$.

step but globally non-linear meaning that it cannot converge to either the linear solution (2.27) or the finite deformation solution detailed in Section 3.3.1. This is shown for both two and 20 loadsteps in Figure 3.7. The MPM convergence using 2 material points is also shown and highlights that although a very small improvement is shown by using GIMP, in order to correctly converge to an analytical solution over multiple loadsteps, the GIMP method must be extended to use a finite deformation framework.

3.2 Large deformation iGIMP

Now that the grid crossing error has been alleviated, it is possible to model problems where material points move significantly from their initial positions. To model this correctly, a large deformation framework must be introduced. In this section an updated Lagrangian formulation with a linear relationship between logarithmic strains and Kirchhoff stresses will be introduced. This is one of the most straightforward ways to implement large strain elasticity [94]. In the updated Lagrangian approach, variables are calculated with reference to a previously converged state, not the original state as in a total Lagrangian approach. This is particularly useful for material point methods as the mesh is discarded after each load step so the original state is not available.

3.2.1 Extending elasticity for large deformations

When accounting for the evolving geometry of a body the linear relationship assumed between infinitesimal strains and small displacements no longer holds. To achieve a result closer to the true response a non-linear relationship between strains and displacements is required. To do this, the concept of the deformation gradient, $[F]$, is introduced as the main variable tracked at each material point throughout a simulation. Given a material point with original coordinates $\{X\}$ that after deformation $\varphi(\{X\})$ has current updated coordinates $\{x\}$, the deformation gradient can be defined as

$$[F] = \frac{\partial\{x\}}{\partial\{X\}}. \tag{3.11}$$

From the deformation gradient it is possible to calculate the left Cauchy-Green strain tensor as

$$[b] = [F][F]^T, \tag{3.12}$$

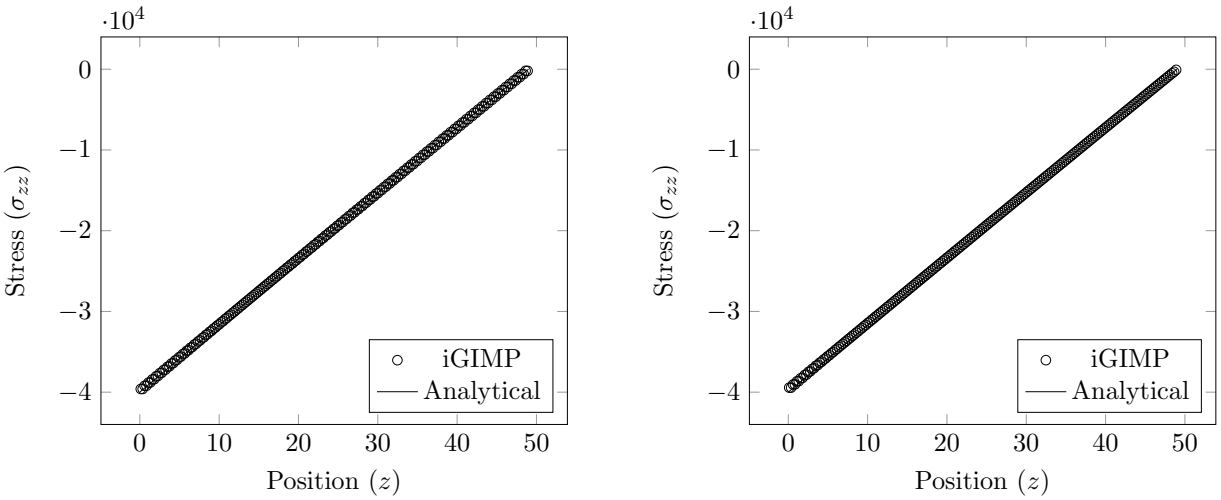

(a) 100 elements, 2 MPs, 2 loadsteps

(b) 100 elements, 2 MPs, 20 loadsteps

Figure 3.6: Variation of stress in a column under self weight using elastic iGIMP.

and from this define the logarithmic strain as

$$\{\varepsilon\} = \frac{1}{2}\ln(\{b\}). \tag{3.13}$$

The Kirchhoff stress can then be calculated as

$$\{\tau\} = [D^{\mathrm{e}}]\{\varepsilon\}, \tag{3.14}$$

where $[D^{\mathrm{e}}]$ is the conventional linear elastic isotropic material stiffness tensor introduced in Equation (2.3). The Cauchy stress can then be retrieved from the Kirchhoff stress using the standard relationship

$$\{\sigma\} = J^{-1}\{\tau\}, \tag{3.15}$$

where $J = \det([F])$ is the volume ratio. This choice of stress and strain measures allows a straightforward use of the small strain constitutive model for large deformation problems as shown in Algorithm 3.3. This approach also allows implementation of elasto-plastic constitutive models within the same framework.

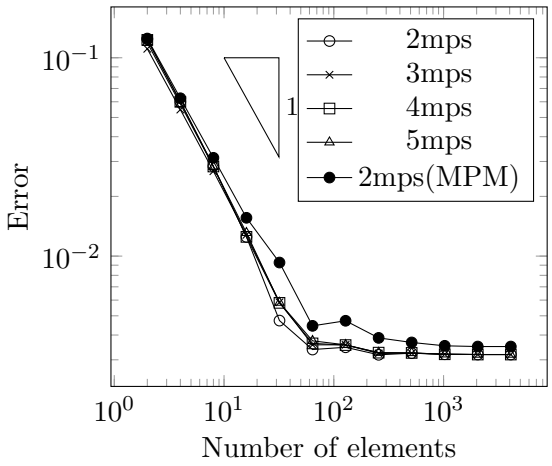

(a) 2 loadsteps (linear analytical solution)

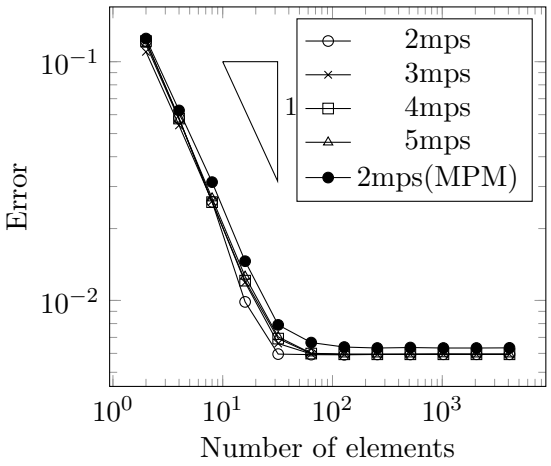

(b) 20 loadsteps (linear analytical solution)

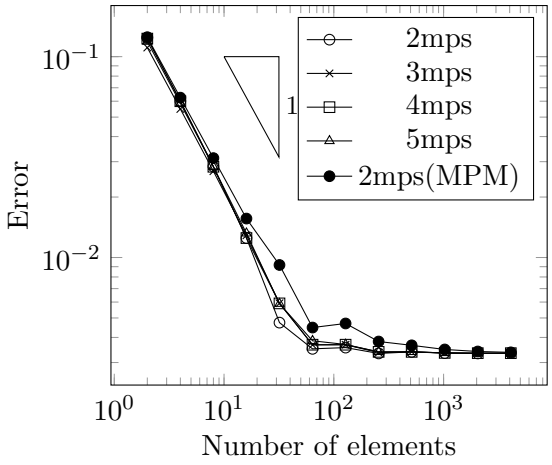

(c) 2 loadsteps (non-linear analytical solution)

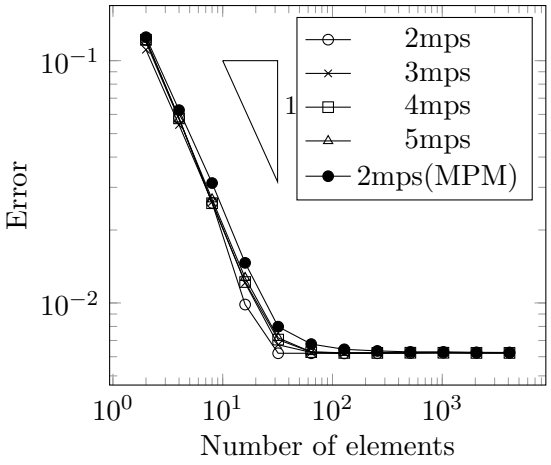

(d) 20 loadsteps (non-linear analytical solution)

Figure 3.7: Convergence to linear and non-linear analytical solutions using elastic iGIMP.

3.2.2 Equilibrium for large deformation elasticity

For this updated Lagrangian approach, the Galerkin form of the weak statement of equilibrium for GIMP can be expressed as

$$\{f^R\} = \int_{\varphi(\Omega)} [G]^T \{\sigma\} d\Omega - \int_{\varphi(\Omega)} [S_{vp}]^T \{f_b\} d\Omega - \int_{\varphi(s)} [S_{vp}]^T \{t\} ds = \{0\}. \tag{3.16}$$

This is the same as (2.16), however, the integrations now take place over the current updated domain and surface, $[S_{vp}]$ is the GIMP shape function matrix and $[G]$ is the strain-displacement matrix containing the derivatives of the GIMP shape functions with respect to the updated nodal coordinates. This is required as the consistent tangent matrix, linking force and displacement, will no longer necessarily be symmetric. Now that (3.16) is non-linear in terms of the unknown displacements it cannot be solved directly. A Newton-Raphson (NR) procedure is chosen to solve these equations. This will require a number of iterations within each load step; in the development below, k will refer to the previous iteration and $k+1$ will refer to the current iteration. The incremental nodal displacements within a load step, $\{\Delta u\}$, are obtained by iteratively updating the displacements until (3.16) is satisfied within a given tolerance.

$$\{\delta u_{k+1}\} = [K]^{-1} \{f_k^R\}, \tag{3.17}$$

where $\{\delta u_{k+1}\}$ are the iterative nodal displacements, $\{f_k^R\}$ is the global residual out-of-balance force vector (3.16) from the kth iteration and $[K]$ is the stiffness matrix evaluated at the current displacement. This must be constructed in full so that the system of equations can be solved for displacements. The current displacement increment within a load step can be obtained through the sum of the increments of displacement in each iteration

$$\{\Delta u_{k+1}\} = \sum_{n=1}^{k+1} \{\delta u_n\}. \tag{3.18}$$

This procedure can be seen in Figure 3.8. Given an applied force of f_n^{ext}, the converged displacement is u_n at point A. The external force is then incremented in the next load step by f_0^R to f_{n+1}^{ext} and using $[K_n]$ predicts an incremental displacement of Δu_1 to an overall displacement of $u_{1_{n+1}}$ indicated by the black symbol. However, after this first iteration the

internal forces caused by this displacement are too small ($f_1^R > tol$), indicated by the white symbol at point B, so another iteration is required. This time the internal force residual reduces to f_2^R and the displacement increases by δu_2 to $u_{2_{n+1}}$ giving a total incremental displacement for the load step of Δu_2. Iterations continue until a given tolerance is reached. The element stiffness matrix for the updated Lagrangian GIMP method is given as

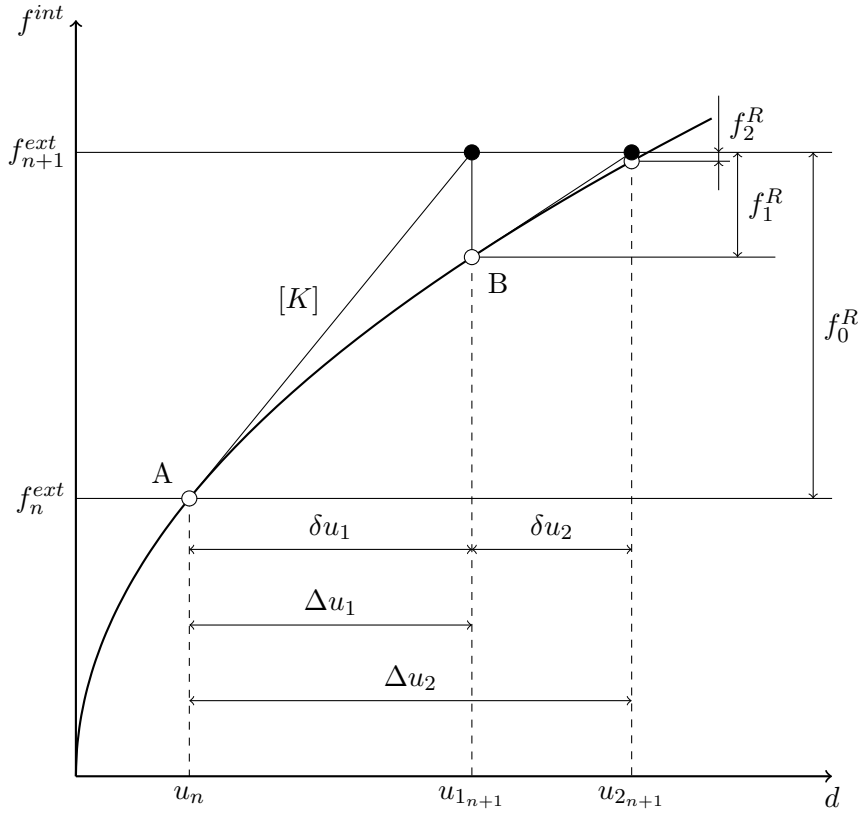

Figure 3.8: Newton Raphson method.

$$[K^E] = \int_{\varphi(\Omega)} [G]^T [D^{cst}][G] d\Omega. \tag{3.19}$$

The non-symmetric spatial material tangent modulus of a material point is given by [157]

$$[D^{cst}] = \frac{1}{2J}[D^{\mathrm{e}}][L^D][B^D] - [S^D], \tag{3.20}$$

where (expressed in index notation for compactness)

$$L^D_{mnpq} = \frac{\partial \ln(b_{mn})}{\partial b_{pq}}, \qquad B^D_{pqkl} = \delta_{pk} b_{ql} + \delta_{qk} b_{pl} \qquad \text{and} \qquad S^D_{ijkl} = \sigma_{il}\delta_{jk}. \tag{3.21}$$

L^D_{mnpq} can be determined as a specific case of the derivative of a general symmetric second order tensor function with respect to its argument, details of which can be found in [126]. It is essential that this tangent modulus is consistent with the integration procedure used in order to achieve correct convergence within the NR scheme. As in small strain GIMP, the stiffness can be summed over material points rather than elements and for each material point the nodal stiffness contributions are

$$[K^p] = [G]^T[D^{cst}][G]V_p, \tag{3.22}$$

where V_p is the current material point volume. A material point's contribution to the internal force vector is given by

$$\{f^{int}\} = [G]^T\{\sigma\}V_p \tag{3.23}$$

where $\{\sigma\}$ is the Cauchy stress at the material point.

Calculation of the deformation gradient

The deformation gradient calculation can be split by multiplicative decomposition into the deformation gradient from a previous converged state, $[F^n]$, and the increment in deformation gradient $[\Delta F]$, that is

$$[F] = [\Delta F][F^n]. \tag{3.24}$$

Usually in an updated Lagrangian formulation $[\Delta F]$ is calculated through [55]

$$[\Delta F] = \left([I] - \frac{\partial\{\Delta u\}}{\partial\{x\}}\right)^{-1}, \tag{3.25}$$

where $[I]$ is a three by three identity matrix and $\{\Delta u\}$ is the increment in displacement. However, in the MPM and GIMP methods the concept of the current coordinates of the nodes does not exist. This is because the shape functions and their derivatives are defined assuming that the global coordinates of the background mesh remain in a regular grid which is reset on each loadstep. It is therefore not possible to use (3.25) to determine the

deformation gradient increment. Instead it must be calculated using

$$[\Delta F] = [I] + \frac{\partial\{\Delta u\}}{\partial\{\tilde{X}\}}, \tag{3.26}$$

(see [55] amongst others) where $\{\tilde{X}\} = \{x\} - \{\Delta u\}$ are the coordinates at the start of the loadstep. Equation (3.26) allows the determination of the increment in the deformation gradient based on a regular (undeformed) background grid. In order to form the stiffness matrix and internal force vector for an updated Lagrangian formulation the derivatives of the shape functions with respect to the updated coordinates, $\{x\}$, are required. It is possible to get this from the coordinates at the start of the load step through

$$\frac{\partial\{\tilde{X}\}}{\partial\{x\}} = [I] - \frac{\partial\{\Delta u\}}{\partial\{x\}} = [\Delta F]^{-1}, \tag{3.27}$$

where $[\Delta F]^{-1}$ is the inverse of the increment in the deformation gradient which can be obtained from (3.26)). The derivatives of the shape functions with respect to the updated coordinates can then be obtained as

$$\frac{\partial(S_{vp})_a}{\partial\{x\}} = \frac{\partial(S_{vp})_a}{\partial\{\tilde{X}\}}\big([\Delta F]\big)^{-1}, \tag{3.28}$$

When calculating $[G]$ from the sum of the different contributions from elements the material point overlaps it is important to take into account the mapping outlined in (3.28). Due to material points potentially having influence over different numbers of nodes, the size of $[G]$ can change between material points. The structure of $[G]$ in 1D for a material point overlapping two elements is

$$[G] = \left[\left[\frac{\partial S^a_{vp1}}{\partial\{\tilde{X}\}}\right] \quad \left[\frac{\partial S^a_{vp2}}{\partial\{\tilde{X}\}}\right] + \left[\frac{\partial S^b_{vp2}}{\partial\{\tilde{X}\}}\right] \quad \left[\frac{\partial S^b_{vp3}}{\partial\{\tilde{X}\}}\right]\right][\Delta F]^{-1}, \tag{3.29}$$

where superscripts a and b refer to the derivatives of the weighting functions in elements a and b.

Updating of material point influence domains

In order to ensure the correct order of convergence of the NR process it is essential to use the volume in the current spatial frame (3.30) in both (3.22) and (3.23). This is achieved

through

$$V_p = \det([\Delta F])V_p^n, \tag{3.30}$$

where V_p^n is the material point volume at the previously converged state, obtained from the product of the global influence domain lengths in each direction l_i^p. In order to calculate this updated volume the influence domains lengths must be updated at the end of each loadstep. This has previously been referred to as cpGIMP [183], and has the advantage of reducing gaps and overlaps which can occur between material point domains if they are not updated (referred to as uGIMP). One option is to update the domain lengths, l_i^p, using diagonal components of the deformation gradient

$$\{l_p\} = \{l_p^0\}\text{diag}([F]), \tag{3.31}$$

where $\{l_p^0\}$ are the original domain lengths. However, problems arise when the rotational component of the deformation gradient is non-zero [151]. Instead here a new approach is taken where the domain lengths are updated according to the symmetric material stretch tensor

$$[U] = \sqrt{[F]^T[F]}, \tag{3.32}$$

where $[F] = [R][U]$ and $[R]$ is the rotational component of the deformation gradient. It should be clear from the above equation that the material stretch tensor is equivalent to the deformation gradient rotated back into the original reference frame. It should also be noted that the right stretch matrix is used here due to the fact that the domains being updated are in the unrotated state. Figure 3.9 shows the decomposition of the deformation gradient into the stretch and rotational components. The material point domains can then be updated according to

$$\{l_p\} = \{l_p^0\}\text{diag}([U]). \tag{3.33}$$

The importance of this modification to previous approaches such as [183] will be demonstrated numerically in Section 3.3.3.

At the end of each loadstep, once the NR process has converged to within the designated tolerance, the material point positions and domains are updated and the background grid is reset. The iGIMP algorithm is outlined in more detail in Algorithms 3.2 and 3.3.

Algorithm 3.2 Implicit GIMP algorithm, main structure

$lstp$	1	2	...lstps	FOR EACH Loadstep		
				Calculate which elements each particle overlaps, and therefore free degrees of freedom		
$\{f_{n+1}^{ext}\}$				increment and map the external forces	$\{f_g^{ext}\} = \{f_p^{ext}\}[S_{vp}]$	(2.19)*
$NRit$	1	2	...	WHILE $\|f^R\| < tol$		
$\{\Delta u_g\}$				solve for displacements	$\{\delta u_{k+1}\} = [K]^{-1}\{f_k^R\}$, $\{\Delta u_{k+1}\} = \{\Delta u_k\} + \{\delta u_{k+1}\}$	(3.17)
$\{\Delta u_p\}$				particle displacement	$\{\Delta u_p\} = [S_{vp}]\{\Delta u_g\}$	(2.25)*
i	1	2	$...n_{mp}$	FOR EACH Material point		
$[\frac{\partial S_{vp1}^a}{\partial X}]\{\Delta u_{n+1}\}$				calculate derivatives of displacements by looping through overlapping elements		
i	1	2	$...n_{mp}$	FOR EACH Material point		
				see Algorithm 3.3		
$\{f^R\}$				out of balance force	$\{f^R\} = \{f^{int}\} - \{f^{ext}\}$	
$\{l_p\}$				update particle domain lengths	$\{l_p\} = \{l_p^0\}\text{diag}([U])$	(3.33)
$\{x_p^{n+1}\}$				update particle positions	$\{x_p^{n+1}\} = \{x_p^n\} + \{u_p\}$	(2.26)

Algorithm 3.3 Implicit GIMP algorithm, material point loop

i	1	2	$...n_{mp}$	FOR EACH Material point		
$[\Delta F]$				deformation gradient increment	$[\Delta F_{n+1}] = [1] + \left[\frac{\partial \Delta u_{n+1}}{\partial \tilde{X}}\right]$	(3.26)
$[F]$				updated deformation gradient	$[F_{n+1}] = [\Delta F_{n+1}][F_n]$	(3.25)
$[b]$				left Cauchy Green strain	$[b] = [F_{n+1}][F_{n+1}]^T$	(3.12)
$[\varepsilon]$				logarithmic elastic strain	$[\varepsilon] = \frac{1}{2}\log([b])$	(3.13)
$[\tau]$				Kirchhoff stress	use small strain constitutive model	
$[\sigma]$				Cauchy stress	$[\sigma] = J^{-1}[\tau]$	(3.15)
$[D^{cst}]$				spatial tangent	$[D^{cst}] = \frac{1}{2J}[D^{\text{alg}}][L^D][B^D] - [S^D]$	(3.20)
$nels$	1	2	$...n_{els}$	FOR EACH overlapping element		
$[G]$				strain displacement matrix	$[G] = \left[\frac{\partial S^a_{vp1}}{\partial \tilde{X}}\right][\Delta F]^{-1} \dots$	(3.29)
$\{f_p^{int}\}$				particle internal force	$\{f_p^{int}\} = [G]^T\{\sigma\}V_p$	(3.23)
$[K_p]$				particle stiffness	$[K_p] = [G]^T[D^{cst}][G]V_p$	(3.10)

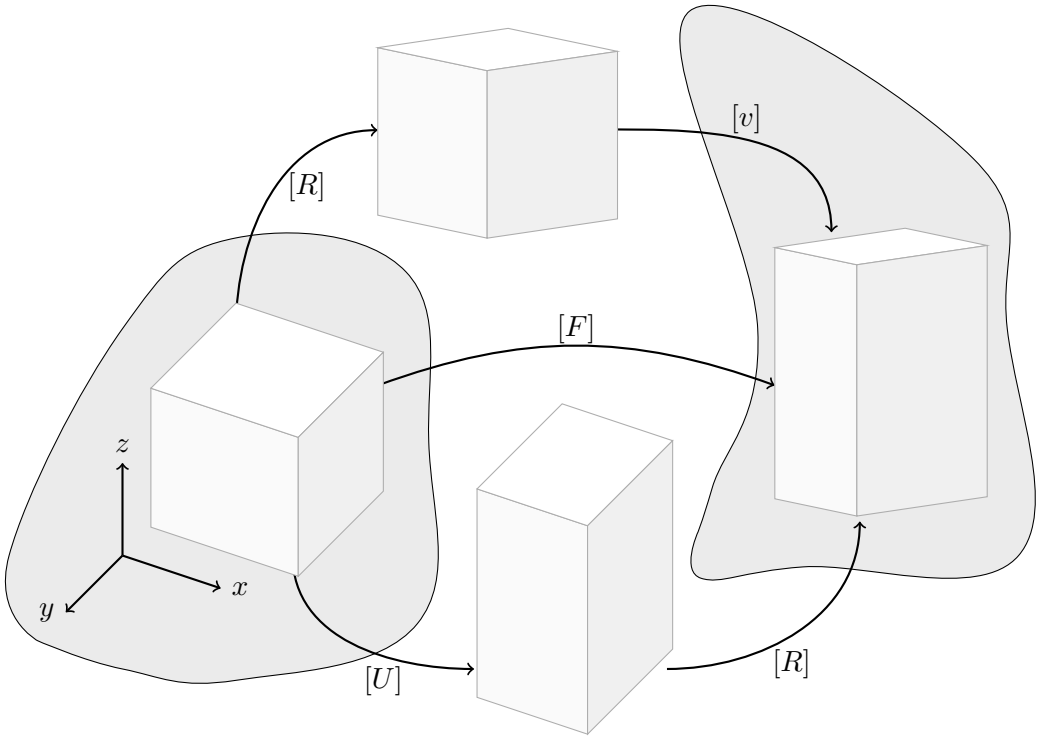

Figure 3.9: Visualisation of the deformation gradient split into rotational and stretch components.

3.3 Numerical examples

In this section, numerical examples are presented to demonstrate the geometrically non-linear updated Lagrangian iGIMP method. The method will be verified in one dimension before examining a number of two dimensional problems.

3.3.1 One dimensional compression under self weight

The response of a column to the application of a body force due to increasing gravity (from 0 to 40000 units) is again modelled using the same geometry (height of 50 units) and material properties (Young's modulus of $E = 10^6$), as in Section 3.1.2. For the case shown in Figure 3.10, the background grid is discretised into 50 elements with each element initially containing two material points positioned so that the influence domain of each material point consists of half the element, or $V_p = 0.5$ units. The stresses at the end of the simulation using the geometrically nonlinear iGIMP method are shown in Figure 3.10. For comparison, the stresses using the standard MPM with a geometrically non-linear framework are also shown using the same discretisation and the analytical solution. Now

that the method is nonlinear within a step as well as globally the analytical solution for the Cauchy stress can be determined from the initial vertical position within the column, Z, by

$$\sigma = \rho_0 b(l_0 - Z), \tag{3.34}$$

where ρ_0 is the initial density of the material l_0 is the original height of the column and b is the body force. The Cauchy stress can be calculated from the Kirchhoff stress by (3.15). The MPM and iGIMP simulations were both run using 20 loadsteps. It can be seen that the MPM simulation experiences an oscillation in its stress response due to grid crossing and deviates significantly from the analytical solution, even more so than for the linear elastic case. In the iGIMP method this problem is alleviated as the transfer of stiffness and internal force between elements happens more gradually giving a smoother change in stiffness as opposed to a sudden jump in the MPM. As before, the error measure can be

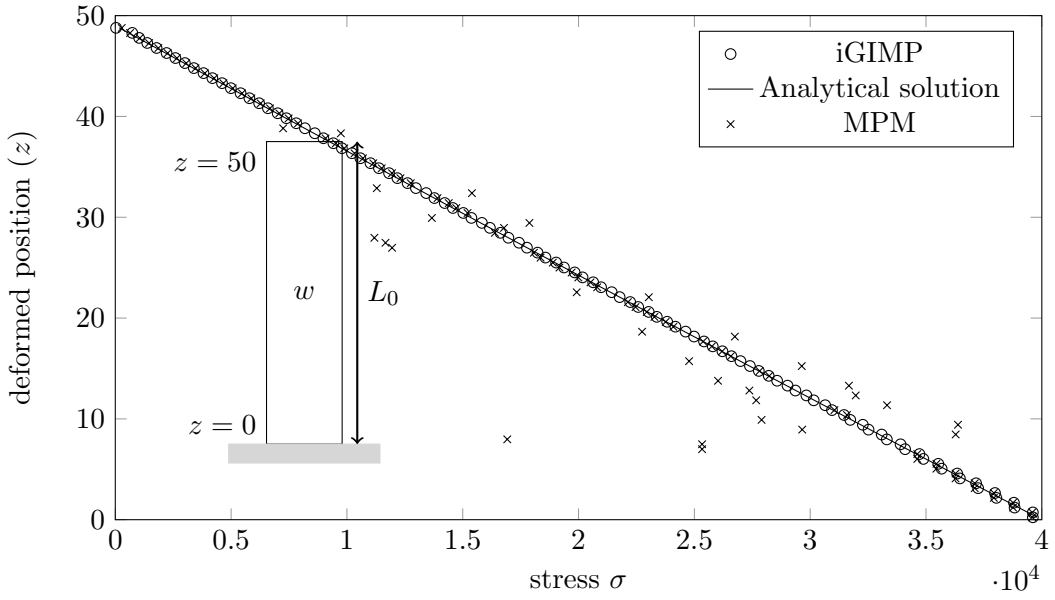

Figure 3.10: Numerical solutions using iGIMP and implicit MPM of a column under self weight plotted against the analytical solution.

defined as

$$\text{error} = \sum_p \frac{|\sigma(z_p) - \sigma_p| V_{p0}}{W L_0}, \tag{3.35}$$

where $\sigma(z_p)$ is the calculated analytical stress for the position, V_{p0} is the initial influence domain size and W is the weight of the column. Figure 3.11 shows the convergence for 2 and 20 loadsteps for both the MPM and iGIMP methods using the large deformation

framework. Now that both methods are now non-linear within each step as well as globally it can be seen that the iGIMP method now continues to converge to the analytical solution whereas the MPM still is restricted by grid crossing.

It can be seen in Figure 3.11 that varying the number of material points does not have a large influence for this problem. The convergence rate for the iGIMP method varies between 1 and 2 for most numbers of elements with a degradation towards higher numbers of elements. It is possible that this can be attributed to the fact that there will be more material points crossing boundaries contributing additional error which cancels out the benefit of additional elements. This highlights the fact that the GIMP method reduces the grid crossing error, but does not remove it completely.

The same problem is also modelled with weights of $w = 100,000$, $w = 200,000$, $w = 300,000$ and $w = 400,000$, up to ten times larger than the initial problem to show the large deformation capabilities of the method. Figure 3.12 shows the stress against position and the corresponding analytical solutions for each of these simulations, all exhibiting good agreement with their respective analytical solutions. Figure 3.13 shows the convergence of the error with increasing number of background grid elements for the largest case. Here the convergence was also compared against linear and quadratic geometrically non-linear FEM solutions. It can be seen that for a given number of elements, the error for the GIMP code is less than the linear FEM simulation with 2 Gauss points per element. The convergence rate for the FEM simulation with linear elements is constant at 1 whereas the convergence rate for the GIMP simulations varies between 1.8 and 0.6. The convergence rate for the FE code with quadratic elements and 3 Gauss points per element is 2 (if 2 Gauss points per element is used then the code achieves machine precision for any number of elements). This is because the two sampling points are correctly positioned to approximate the solution exactly, for a linear element the same applies to a single Gauss point in the centre of the element. Due to the positioning of material points this is not the case for the GIMP method. In one dimension the logarithmic strain (3.13) can be defined as

$$\varepsilon = \frac{1}{2}\ln(F^2) = \ln(F) \tag{3.36}$$

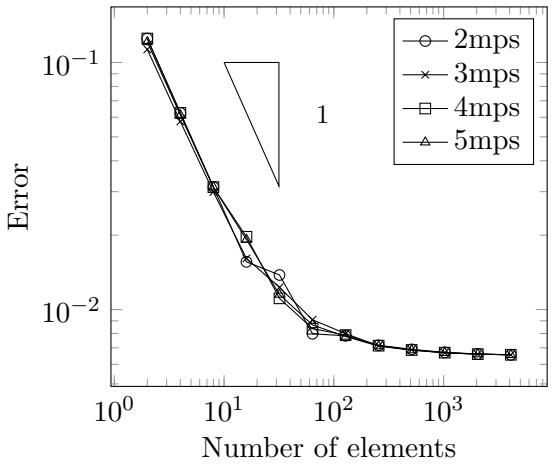

(a) 2 loadsteps, MPM

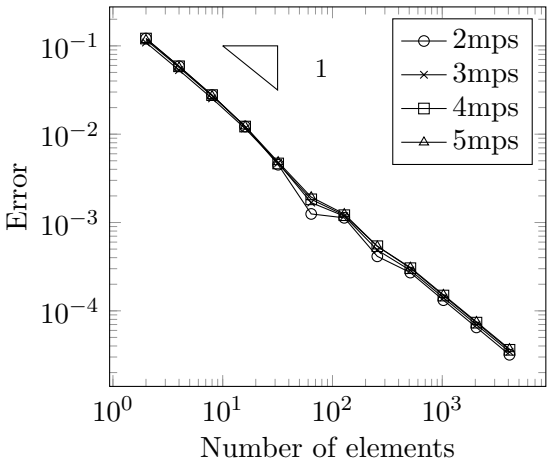

(b) 2 loadsteps, iGIMP

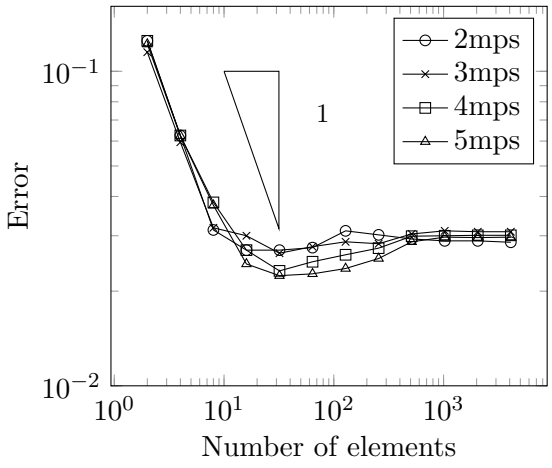

(c) 20 loadsteps, MPM

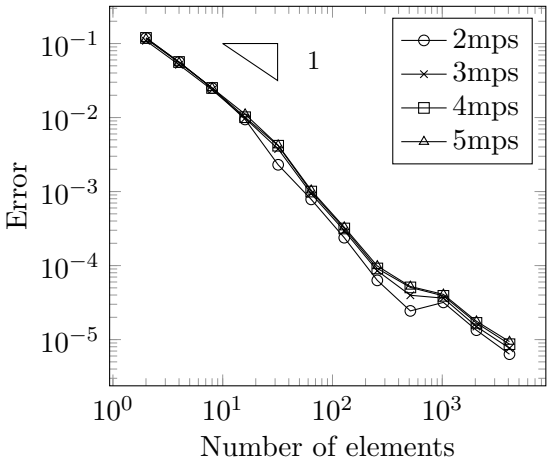

(d) 20 loadsteps, iGIMP

Figure 3.11: Comparison of convergence rates for geometrically nonlinear iGIMP and MPM

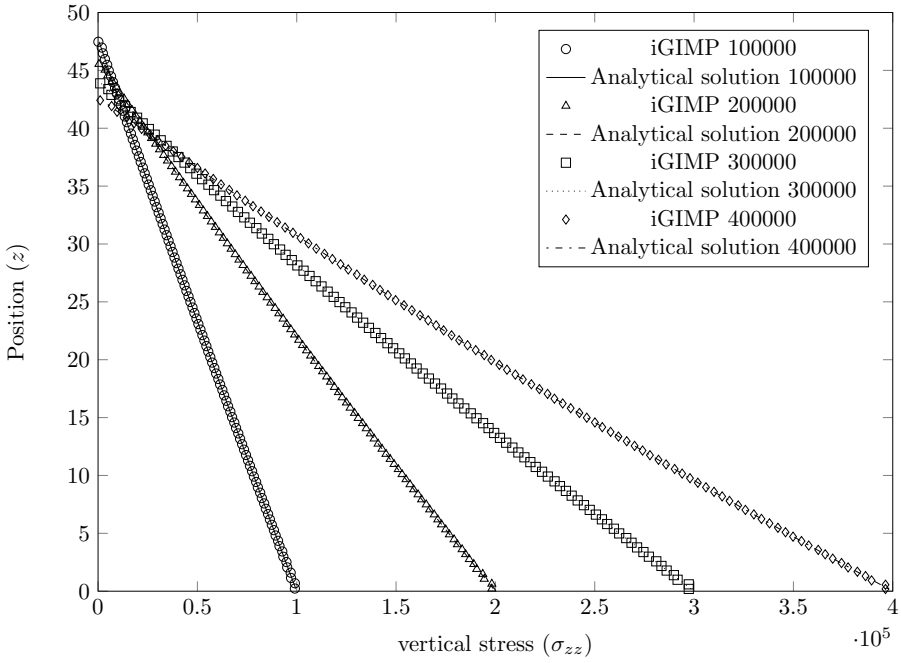

Figure 3.12: Stress against position for 1D column with larger weights.

and the Kirchhoff stress is linked to the logarithmic strain through

$$\tau = E\varepsilon. \tag{3.37}$$

Combining the above equations, the Cauchy stress in one dimension can be expressed in terms of the deformation gradient as

$$\sigma = \frac{1}{F} E \ln(F). \tag{3.38}$$

Knowing σ from (3.34) for any point in the problem domain, it is possible to find the deformation gradient by using a Newton process to solve for F in (3.38). It is not possible to solve this directly due to both F and $\ln F$ appearing in (3.38). From this analytical solution, the deformation gradient at the base of the column for the largest deformation is calculated to be 0.74292. By integrating the deformation gradient over the height of the column, the displacement at the top of the column is calculated to be -7.3347. Using two material points per element, and taking the top displacement from the top material point and bottom deformation gradient from the bottom most material point it can be seen in Table 3.1 that the displacement is accurate to 5 significant figures for all numbers of grid

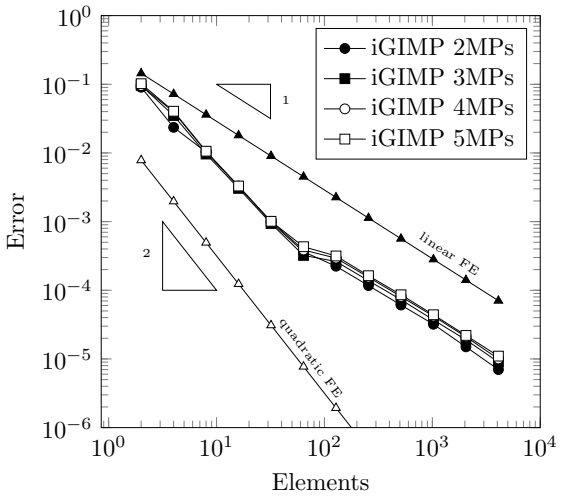

Figure 3.13: Convergence with increasing numbers of elements for column loaded under self weight ($w = 400,000$).

elements shown, and the error in deformation gradient decreases with increasing elements with a linear rate of convergence, where the deformation gradient error is given as

$$F_{\text{error}} = |F_p - F_{(0)}|/F_{(0)}. \tag{3.39}$$

where F_p is the computed deformation gradient and $F_{(0)}$ is the analytical deformation gradient.

3.3.2 2D simply supported beam

The second example is a 2D analysis of a simply supported beam loaded with a uniform pressure on the upper surface. The beam has a depth of 5.08 mm and a length of 254

Table 3.1: Error in deformation gradient and displacement, 2mp/gp per element

number of elements	256	512	1024	2048
iGIMP				
top displacement (m)	-7.3347	-7.3347	-7.3347	-7.3347
base deformation gradient	0.74322	0.74307	0.74300	0.74296
displacement error	-	-	-	-
deformation gradient error	4.091×10^{-4}	2.041×10^{-4}	1.017×10^{-4}	5.040×10^{-5}
Linear FEM				
top displacement (m)	-7.3347	-7.3347	-7.3347	-7.3347
base deformation gradient	0.74325	0.74308	0.74300	0.74296
displacement error	-	-	-	-
deformation gradient error	4.477×10^{-4}	2.237×10^{-4}	1.118×10^{-4}	5.593×10^{-5}

mm although only half of this is modelled due to symmetry as can be seen in Figure 3.14(a). The pressure equivalent to 276 kPa is applied by applying equal forces to each of the top layer of material points in the beam and is incremented over 20 load steps. The beam is modelled using 320 material points initially positioned in 80 background grid elements. The material properties used are a Young's modulus of 68.95 GPa and Poisson's ratio of 0.25. Figure 3.15 shows a graph of the applied pressure against the normalised displacement for the simulation conducted using iGIMP and values corresponding to the analytical solution which can be found in [177]. The iGIMP results show in general good agreement with the analytical solution, although it is observed that the displacement is slightly larger in the simulation than for the analytical solution. One explanation of this could be the application of the pressure at material points rather than to the actual top surface of the beam.

The convergence of the global Newton process can be seen in Table 3.2. The asymptotically quadratic convergence exhibited here indicates a correct implementation.

3.3.3 2D cantilever beam

The final example in this chapter is an elastic cantilever beam of length 10m and depth 1m. The beam is loaded with a point load of 100kN applied at the vertical mid-point on its free end over 50 load steps. As currently this is difficult to achieve in the GIMP and MPM, due to there being no explicit tracking of the material boundary when it is not aligned with the mesh, the load is split between the two material points closest to this point above and below the neutral axis. The material properties of the beam are a Young's modulus

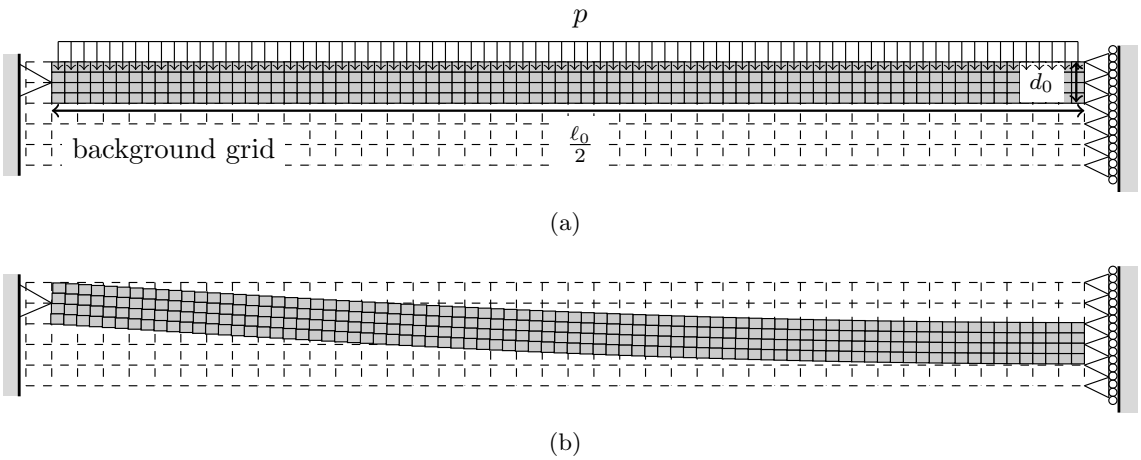

Figure 3.14: Geometry and deformation of simply supported beam under uniform pressure

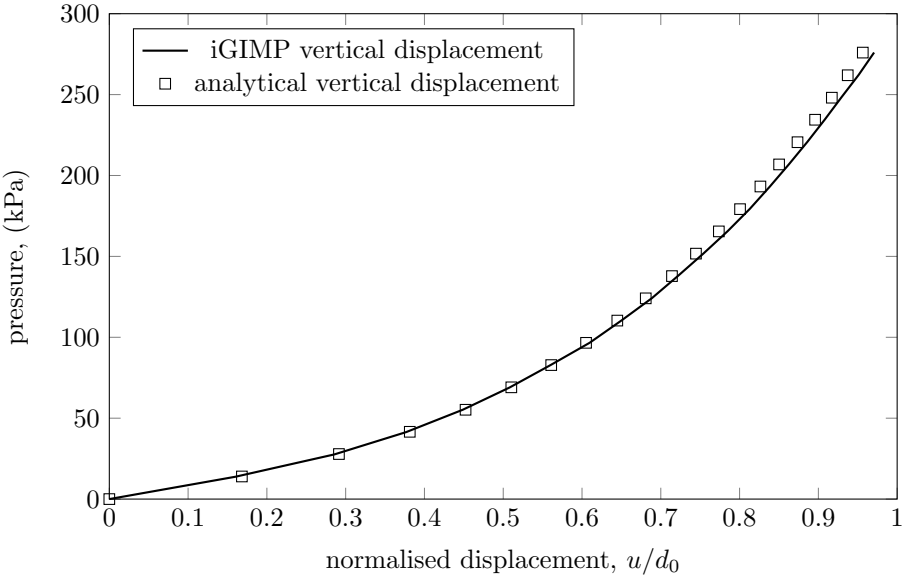

Figure 3.15: Graph of pressure against normalised displacement for simply supported beam.

Table 3.2: Newton Raphson residuals showing near asymptotic quadratic convergence.

Step	16	17	18	19	20
Iteration 1	5.867×10^{-3}	4.604×10^{-3}	4.143×10^{-3}	5.179×10^{-3}	3.169×10^{-3}
Iteration 2	3.039×10^{-6}	2.055×10^{-6}	1.641×10^{-6}	1.956×10^{-6}	1.001×10^{-6}
Iteration 3	8.331×10^{-12}	3.495×10^{-12}	2.412×10^{-12}	4.133×10^{-12}	1.001×10^{-12}

of 12MPa and Poisson's ratio of 0.2. The initial discretisation of the background grid was 21 x 21 elements to give the beam room to deform. The beam was represented by filling 40 of these elements each with 3 x 3 material points. Boundary conditions are applied to the grid at the lefthand end of the beam restricting displacement in both directions at the neutral axis and restricting horizontal displacement elsewhere. Figure 3.16 shows the beam at the beginning of the simulation and its final deformed configuration, with the loading and boundary conditions highlighted for clarity. As mentioned in Section 3.2 it is necessary to update the material point influence domain lengths using the stretch tensor ($[U]$) rather than the full deformation gradient to be able to handle material rotations. Figure 3.17 shows why this is important, Subfigure 3.17(a) shows how the analysis collapses as material point domains are updated using the deformation gradient (highlighted by the circled region on the right hand figure) and Subfigure 3.17(b) shows the same loadsteps of an equivalent analysis where the domains are updated using $[U]$ showing the correct response. Figure 3.18 shows the horizontal and vertical displacement at the point where the beam is loaded, normalised by the length of the beam. For GIMP this is the average of the two loading points shown in Figure 3.16. The solution using the geometrically non-linear iGIMP method with the domains updated using $[U]$ is plotted alongside a FEM analysis using 8 noded quadratic elements and 3 x 3 Gauss quadrature with the same boundary conditions and element discretisation of the initial geometry. The analytical solution which is provided in [130] is also given. It can be seen that the GIMP method agrees well with both the finite element solution and the analytical solution.

3.4 Observations

In this chapter it has been observed that by introducing the GIMP method, nonphysical stress oscillations caused by the grid crossing in the MPM are reduced, however for a simple problem, this is insufficient to achieve convergence towards analytical solutions due to the incrementally linear nature of the small strain iGIMP method. A geometrically nonlinear framework using logarithmic strains and Kirchhoff stresses has been introduced and it is shown that using this convergence can be achieved for the 1D column problem. This is the first time an implicit GIMP method has been implemented in this way, particular novelties lie in the correct updating of the deformation gradient and mapping of

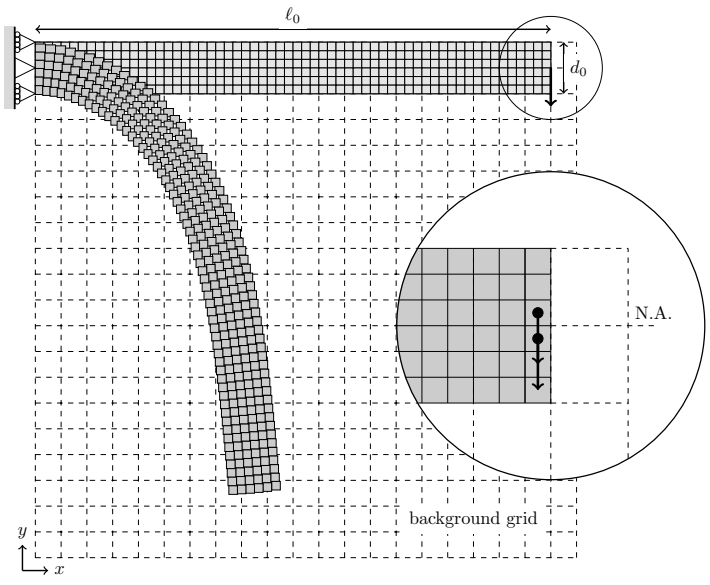

Figure 3.16: Initial and final material point positions and boundary conditions shown for cantilever beam.

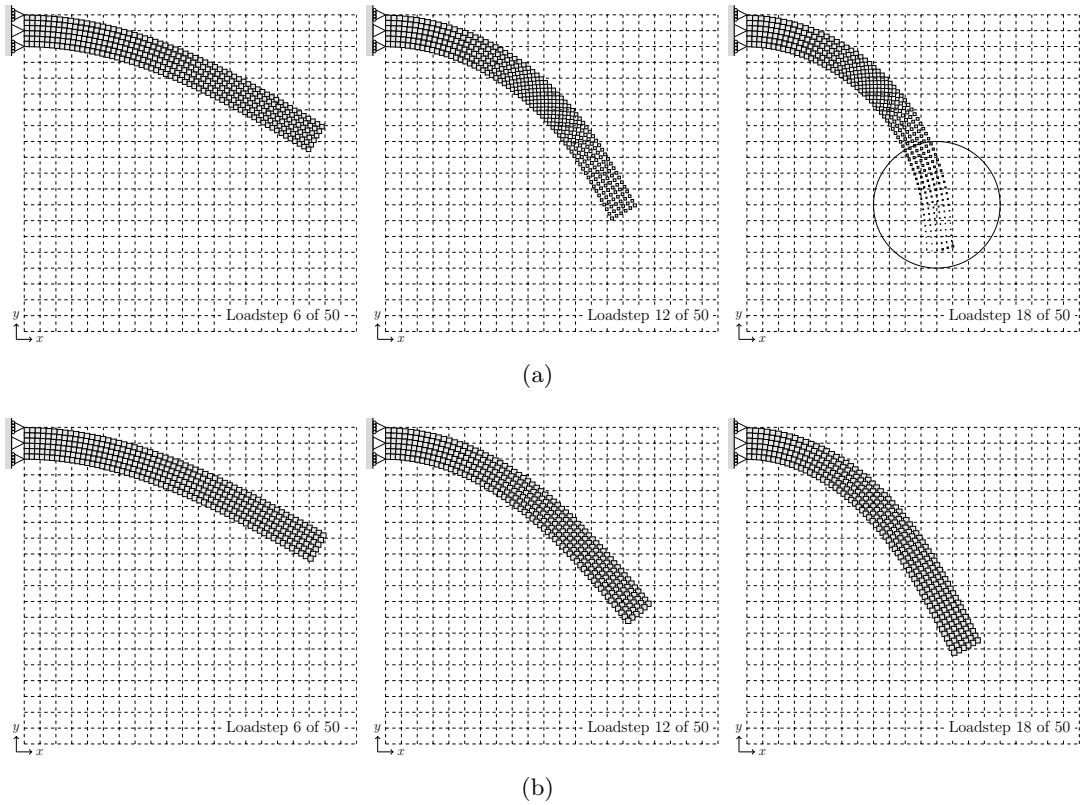

Figure 3.17: Comparison of simulation of cantilever beam the deformation gradient $[F]$ (a) and using the right symmetric stretch matrix $[U]$ (b) to update influence domains.

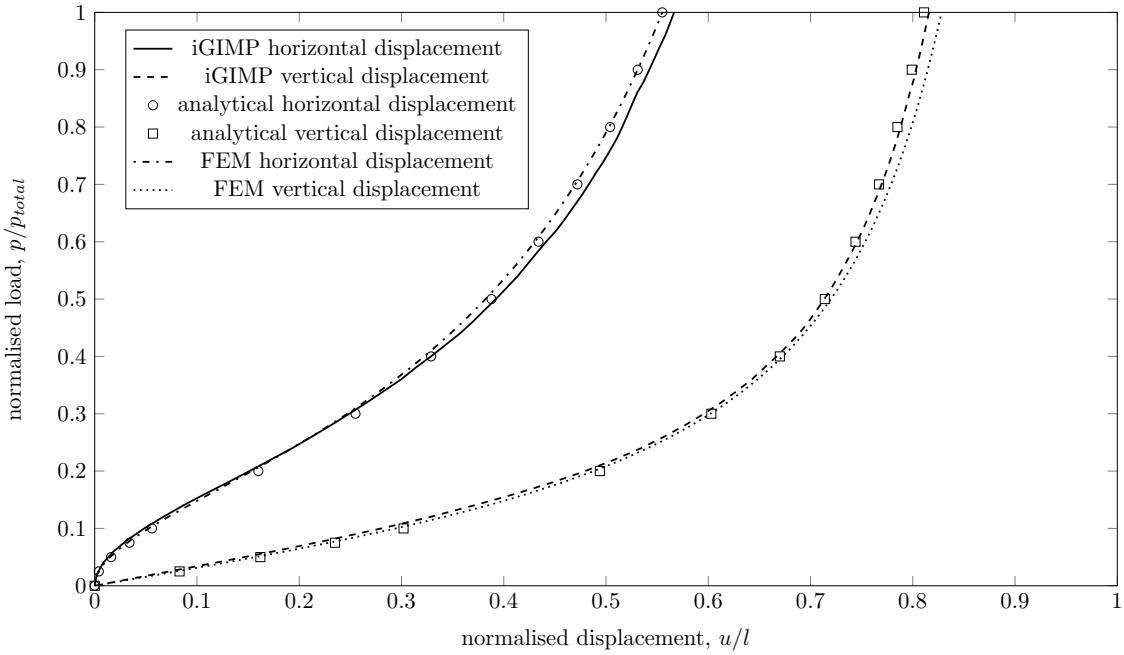

Figure 3.18: Horizontal and vertical displacement of tip of cantilever beam.

the basis spatial derivatives to ensure that equilibrium is satisfied in the correct frame. Additionally, novel updating of influence domains using the stretch tensor has been used. The convergence of the method with mesh refinement has been shown, and correct implementation has been demonstrated through the optimum convergence within the non-linear NR process. Further two-dimensional examples have demonstrated the iGIMP method's ability to correctly handle large deformations. In this chapter, only elastic material behaviour has been explored. Using the non-linear framework set out in this chapter it will now be possible to implement elasto-plastic behaviour with the GIMP method which is essential if the method is to be used for geotechnical modelling. For more general constitutive models including anisotropy, some further modifications beyond what is included in this thesis would be required.

Chapter 4

iGIMP with material non-linearity

In the previous chapter, an elastic finite deformation framework was implemented with the implicit Generalised Interpolation Material Point (iGIMP) method based on the work of [156] and [54]. In this chapter, this finite deformation framework will be extended to allow elasto-plasticity. The Generalised Interpolation Material Point (GIMP) method has been used with elasto-plasticity (for example see [70, 113, 190]), however all of these have used explicit time integration with the sole exception of the work of the author [30]. This chapter will begin with the introduction to elasto-plasticity in Section 4.1. This will introduce idea of elastic and plastic strains, stress invariants and the concept of a yield surface in principal stress space in which isotropic plasticity models can be constructed. Classical perfect plasticity will be introduced in Section 4.1.2 using a rate relationship, additive decomposition and a plastic flow rule. The stress integration procedure necessary to arrive at an incremental formulation will be explained including the importance of the algorithmic consistent tangent. The use of an elasto-plastic constitutive model within the finite deformation framework for iGIMP will then be shown in Section 4.2 to be no more complicated than in FEM before verifying the method using numerical examples in Section 4.3.

4.1 Introduction to elasto-plasticity

So far in this thesis a linear elastic relationship between stress and strain has been used. This was introduced in Chapter 2 as

$$\{\sigma\} = [D^e]\{\varepsilon\}, \tag{4.1}$$

where $\{\sigma\}$ is a vector containing the Cauchy stresses, $[D^e]$ is the elastic stiffness matrix and $\{\varepsilon\}$ is the strain vector. In Figure 4.1 the 1D stress-strain plot for an elastic material can be seen as the behaviour between points 1 and 2, the gradient is equal to the Young's modulus and any strains applied are reversible and if a load is removed then the material will revert to its initial state. In order to more realistically model problems involving

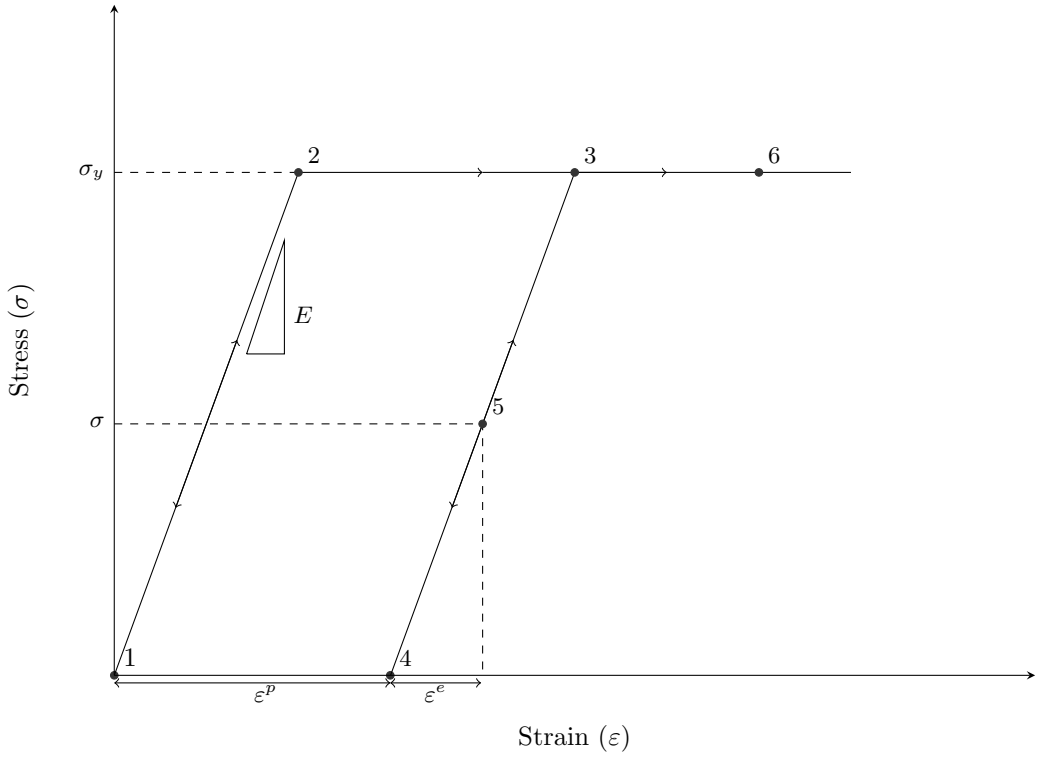

Figure 4.1: Stress-strain plot for perfect plasticity

materials such as soils with the Material Point Method (MPM), the concept of elasto-plasticity must be introduced. To do this the linear elastic relationship between stress and strain must be replaced with another constitutive relationship to allow that when a certain stress state is reached the material yields and deforms permanently introducing plastic strain. This results in a stress response in general which is path dependent and

irreversible. In Figure 4.1 if the applied strain causes the yield stress to be reached (for the case of perfect plasticity) the stress will remain the same for an increased level of strain and plastic strains will be introduced. This can be seen at the change from 1-2 to 2-3. If unloading begins (at point 3) line 3-4 will be followed, so the initial state will not be recovered. If reloading occurs it is possible to follow line 4-3 back up to the yield stress and then continue along from 3-6. To define when a material behaves elasto-plastically the concept of a yield surface will be introduced. A yield surface divides stress space into elastic, elasto-plastic and inadmissible regions. Because stress is a 9-component quantity with 6 independent components

$$[\sigma] = \begin{bmatrix} \sigma_{xx} & \sigma_{xy} & \sigma_{zx} \\ \sigma_{xy} & \sigma_{yy} & \sigma_{yz} \\ \sigma_{zx} & \sigma_{yz} & \sigma_{zz} \end{bmatrix}, \tag{4.2}$$

isotropic plasticity models are best represented in principal stress space. Principal stresses are the components of stress after a rotation of the stress space such that the shear components are equal to zero. This can be seen in Figure 4.2 where, after the rotation, only the principal stresses are present not the previously existing shear stresses. The principal stresses can be calculated as the eigenvalues of the Cauchy stress matrix. The use of these principal components allow any stress state to be visualised in 3D space. In

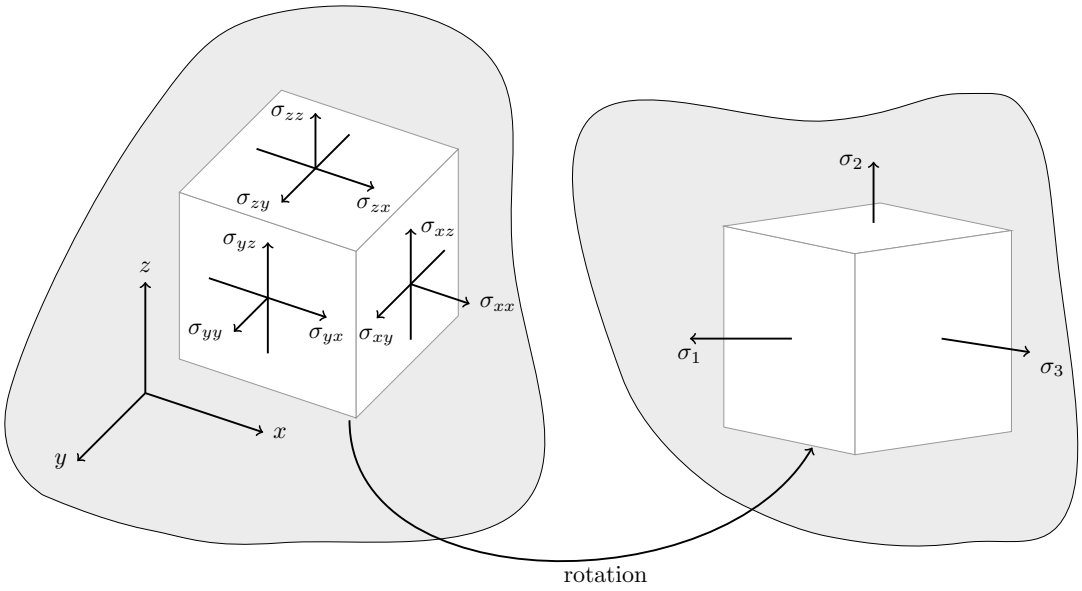

Figure 4.2: Rotation of stress space to give principal stresses

order to specify a material's stress state it is useful to make use of stress invariants, which are invariant to rigid body translations and rotations. Beginning with the Cauchy stress $[\sigma]$ we can define its trace as the first invariant

$$I_1 = tr([\sigma]). \tag{4.3}$$

From this, a deviatoric stress matrix $[s]$ can be calculated as

$$[s] = [\sigma] - I_1[1]/3, \tag{4.4}$$

where [1] is the three by three identity matrix. The second deviatoric stress invariant J_2 can then be introduced as

$$J_2 = \frac{1}{2}tr([s][s]). \tag{4.5}$$

The third deviatoric stress invariant J_3 is given as

$$J_3 = \frac{1}{2}tr([s][s][s]). \tag{4.6}$$

Using these stress invariants, a set of cylindrical coordinates (known as the Haigh Westergaard coordinates) can be given in principal stress space. These are the hydrostatic stress

$$\zeta = \frac{I_1}{\sqrt{3}}, \tag{4.7}$$

the deviatoric stress

$$\rho = \sqrt{2J_2}, \tag{4.8}$$

and the Lode angle

$$\theta = \frac{1}{3}\arcsin\left(\frac{-3\sqrt{3}}{2}\frac{J_3}{J_2^{3/2}}\right). \tag{4.9}$$

4.1.1 Yield surface

In principal stress space it is possible to define a yield surface based on these Haigh Westergaard coordinates. The yield surface can be described by a yield function (f) so that we have

- an allowable elastic region inside the yield surface where $f < 0$;
- an inadmissible region outside of the yield surface where $f > 0$; and
- an elasto-plastic boundary on the yield surface where $f = 0$.

This chapter will focus on von Mises perfect plasticity however the framework given is suitable for any isotropic plasticity model. The von Mises yield surface can be defined as

$$f = \rho^2 - \rho_y^2 = 0, \tag{4.10}$$

where ρ_y is the deviatoric yield stress of the material. The von Mises yield surface and the different regions are shown in Figure 4.3. It can be seen that due to being only dependent on ρ, this is represented by an open ended cylinder around the hydrostatic axis. On this yield surface is where plastic straining occurs and inside the cylinder is the region where the material behaves elastically. Due to having no hydrostatic component the von Mises yield surface is more physically suited to the modelling of metals than geomaterials which may ultimately be of interest. Despite this it offers a simple way to demonstrate the elasto-plastic capabilities of the iGIMP method.

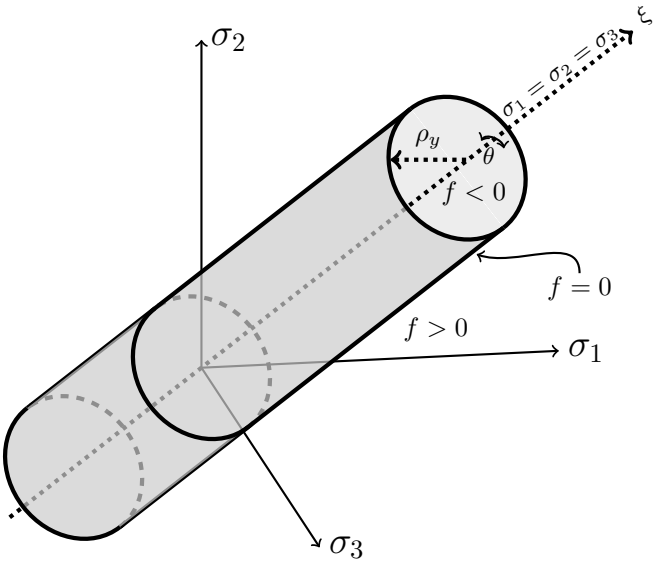

Figure 4.3: von Mises yield surface in principal stress space

4.1.2 Classical perfect plasticity

In this section the four key components of elasto-plasticity under small strains will be introduced. Firstly, when considering elasto-plastic behaviour, it is assumed that a rate relationship between exists elastic strain $\{\varepsilon^e\}$ and Cauchy stress

$$\{\dot{\sigma}\} = [D^e]\{\dot{\varepsilon^e}\}, \tag{4.11}$$

where $\{\dot{\sigma}\}$ is the stress rate, $\{\dot{\varepsilon^e}\}$, the strain rate and $[D^e]$ is the linear elastic stiffness matrix as used previously in 4.1. Throughout this work the superscripts $\cdot^{\mathrm{e}}$ and $\cdot^{\mathrm{p}}$ denote elastic and plastic terms, respectively. Secondly, it is assumed that the total strain, $\{\varepsilon\}$, can be additively split into this elastic strain, $\{\varepsilon^{\mathrm{e}}\}$, and a plastic strain, $\{\varepsilon^{\mathrm{p}}\}$,

$$\{\varepsilon\} = \{\varepsilon^{\mathrm{e}}\} + \{\varepsilon^{\mathrm{p}}\}. \tag{4.12}$$

This can be seen in Figure 4.1 where the strain at point 5 is split into elastic and plastic components adding up to the total strain. The plastic strain can be calculated by using an associated plastic flow rule of the form

$$\{\dot{\varepsilon^p}\} = \dot{\gamma}\left\{\frac{\partial f}{\partial \sigma}\right\}, \tag{4.13}$$

where $\{\dot{\varepsilon^{\mathrm{p}}}\}$ is the rate of change of plastic strain, $\dot{\gamma}$ is the plastic multiplier (or consistency parameter) which controls the magnitude of plastic strains and $\left\{\frac{\partial f}{\partial \sigma}\right\}$ is the derivative of the yield function with respect to stress. The use of an associated rule means that the plastic strains occur normal to the yield surface. These equations are subject to the the Kuhn-Tucker-Karush consistency conditions: The plastic multiplier must always be non-negative,

$$\dot{\gamma} \geq 0, \tag{4.14}$$

the yield function must have a value less than or equal to zero,

$$f(\{\sigma\}) \leq 0, \tag{4.15}$$

that is the stress must lie inside the yield surface (elastic behaviour) or in the yield surface (plastic behaviour), and plastic strains can only occur when the yield function is equal to zero

$$\dot{\gamma} f(\{\sigma\}) = 0. \tag{4.16}$$

4.1.3 Elasto-plastic predictor-correction algorithm

Plastic straining must occur on the yield surface. From the rate equation above (4.11), it is necessary to arrive at an incremental relationship describing what the updated stress state will be given an initial stress state σ_n and a strain increment. This is achieved through an elastic predictor-plastic corrector procedure, this can be seen visually in Figure 4.4. The first step to calculate a trial stress $\{\sigma_{tr}\}$ by assuming that the entire strain increment is elastic

$$\{\sigma_{tr}\} = [D^e]\{\{\varepsilon_n^e\} + \{\Delta\varepsilon_{n+1}\}\}, \tag{4.17}$$

where the elastic trial strain can be defined as

$$\{\varepsilon_{tr}^e\} = \{\{\varepsilon_n^e\} + \{\Delta\varepsilon_{n+1}\}\}. \tag{4.18}$$

It is then checked whether or not this trial stress is on, inside or outside the yield surface.

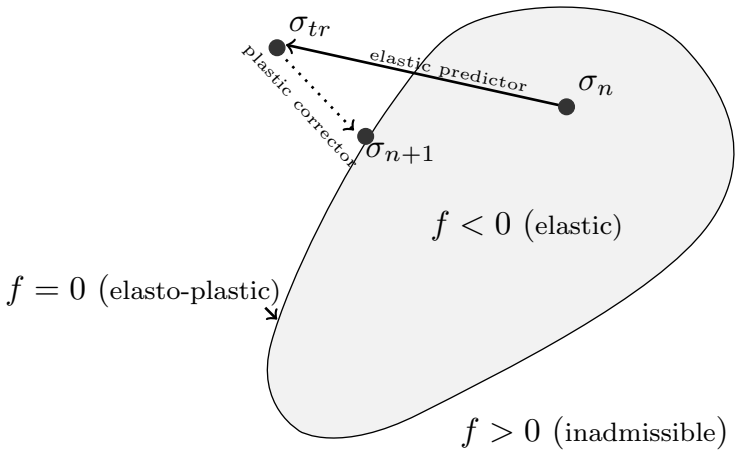

Figure 4.4: Elastic predictor-Plastic correcter stress updating

If the trial stress is on or inside the the yield surface ($f \leq 0$) then the trial stress is the correct updated stress and no further changes are necessary. However if the trial stress is outside the yield surface in the inadmissible region then it is necessary to integrate the rate

equation to return the stress to the yield surface. There are a number of ways in which this integration can be performed and in general (apart from a few simple models where exact integration can be used) these can be split into explicit and implicit integration methods. Explicit methods of stress integration, such as forward Euler, are generally less complicated than implicit methods, however they possess disadvantages in terms of accuracy and convergence. Specifically, explicit methods do not enforce the yield condition at the end of each step and if they do not use a consistent tangent this will mean that the global stiffness does not give asymptotically quadratic convergence for the global Newton Raphson (NR) algorithm. To avoid these issues, an implicit backward Euler method will be used and will be outlined below for perfect plasticity. A plastic corrector step is then used to correct the stress back onto the yield surface as shown in Figure 4.4.

$$\{\sigma_{n+1}\} = [D^e]\{\{\varepsilon^e_n\} + \{\Delta\varepsilon_{n+1}\} - \{\Delta\varepsilon^p\}\}. \tag{4.19}$$

where updated elastic strain (ε^e_{n+1}) is given as

$$\{\varepsilon^e_{n+1}\} = \{\{\varepsilon^e_n\} + \{\Delta\varepsilon_{n+1}\} - \{\Delta\varepsilon^p\}\}. \tag{4.20}$$

Making use of the associated plastic flow rule (4.13), and the consistency conditions it becomes necessary to solve the following system of algebraic equations to calculate the unknown updated elastic strain and the increment in the plastic multiplier

$$\{\varepsilon^e_{n+1}\} = \{\varepsilon^e_{tr}\} - \Delta\gamma \left\{\frac{\partial f}{\partial \sigma}\right\} \tag{4.21}$$

$$f(\sigma_{n+1}) = 0 \tag{4.22}$$

subject to

$$\dot{\gamma} > 0. \tag{4.23}$$

These return mapping equations can be solved using a NR method as shown in existing works including [42, 53] with unknowns

$$\{x\} = \{\{\varepsilon^e\}\Delta\gamma\}^T \tag{4.24}$$

and residuals

$$\{b\} = \begin{Bmatrix} \{\varepsilon^e\} - \{\varepsilon^e_{tr}\} + \Delta\gamma \left\{\frac{\partial f}{\partial \sigma}\right\} \\ f \end{Bmatrix} = \begin{Bmatrix} \{b_1\} \\ b_2 \end{Bmatrix} \tag{4.25}$$

The derivatives of the residuals with respect to the unknowns form the matrix [A]

$$[A] = \begin{bmatrix} \left[\frac{\partial b_1}{\partial \varepsilon^e}\right] & \left\{\frac{\partial b_1}{\partial \Delta\gamma}\right\} \\ \left\{\frac{\partial b_2}{\partial \varepsilon^e}\right\}^T & \frac{\partial b_2}{\partial \Delta\gamma} \end{bmatrix} = \begin{bmatrix} [1] + \Delta\gamma \left[\frac{\partial^2 f}{\partial \sigma^2}\right][D^e] & \left\{\frac{\partial f}{\partial \sigma}\right\} \\ \left\{\frac{\partial f}{\partial \sigma}\right\}^T [D^e] & 0 \end{bmatrix} \tag{4.26}$$

where all derivatives are calculated with respect to the updated values of the unknowns. Beginning from a starting value of $\{\varepsilon^e\} = \{\varepsilon^e_{tr}\}$ and $\Delta\gamma = 0$ the increment of the unknowns is calculated by

$$\{\delta x\} = -[A]^{-1}\{b\} \tag{4.27}$$

which is then used to update $\{x\}$ and then calculating new values of $[A]$ and $\{b\}$ and iterating until $\{b\}$ is reduced to within a given tolerance. The steps for the von Mises yield surface as used in the examples in this chapter can be seen in Algorithm 4.2.

4.1.4 Consistent linearisation

Now that an algorithm has been established to calculate an updated stress from a given trial strain it is essential to have a global tangent which is consistent with this algorithm ($[D^{alg}]$). This ensures that the relationship between stress and trial strain is consistent with the stress integration in the constitutive model. In order for the global NR procedure to converge quadratically it is necessary to derivative of the current stress with respect to the trial strain so that for an increment in elastic trial strain so that the updated stress can be found as

$$\{d\sigma\} = [D^{alg}]\{d\varepsilon^e_{tr}\}, \tag{4.28}$$

where

$$[D^{alg}] = \left[\frac{\{d\sigma\}}{\{d\varepsilon^e_{tr}\}}\right]. \tag{4.29}$$

This derivative is obtained by linearising the residuals (4.25) with respect to the elastic trial strain $\{\varepsilon^e_{tr}\}$. This first requires the derivatives of $\{b_1\}$

$$\frac{\{d\varepsilon^e\}}{\{d\varepsilon^e_{tr}\}} = \frac{\{d\varepsilon^e\}}{\{d\sigma\}}\frac{\{d\sigma\}}{\{d\varepsilon^e_{tr}\}} = [C^e]\frac{\{d\sigma\}}{\{d\varepsilon^e_{tr}\}}, \tag{4.30}$$

where the chain rule has been used and $[C^e] = [D^e]^{-1}$ is the elastic compliance matrix so that $\{d\sigma\}[C^e] = \{\varepsilon^e\}$, hence

$$-\frac{\{d\varepsilon^e_{tr}\}}{\{d\varepsilon^e_{tr}\}} = -1, \quad \text{and} \tag{4.31}$$

$$\frac{\left\{d\Delta\gamma\left\{\frac{\partial f}{\partial\sigma}\right\}\right\}}{\{d\varepsilon^e_{tr}\}} = \Delta\gamma\frac{\left\{d\left\{\frac{\partial f}{\partial\sigma}\right\}\right\}}{\{d\varepsilon^e_{tr}\}} + \left\{\frac{\partial f}{\partial\sigma}\right\}\frac{\{d\Delta\gamma\}}{\{d\varepsilon^e_{tr}\}}$$
$$= \Delta\gamma\frac{\left\{d\left\{\frac{\partial f}{\partial\sigma}\right\}\right\}}{\{d\sigma\}}\frac{\{d\sigma\}}{\{d\varepsilon^e_{tr}\}} + \left\{\frac{\partial f}{\partial\sigma}\right\}\frac{\{d\Delta\gamma\}}{\{d\varepsilon^e_{tr}\}}. \tag{4.32}$$

Along with the derivative of $\{b_2\}$

$$\frac{df}{\{d\varepsilon^e_{tr}\}} = \frac{df}{\{d\sigma\}}\frac{\{d\sigma\}}{\{d\varepsilon^e_{tr}\}}. \tag{4.33}$$

Using these derivatives and rearranging, the following equations can be obtained

$$[C^e]\{d\sigma\} + \Delta\gamma\left\{\frac{\partial^2 f}{\partial\sigma^2}\right\}\{d\sigma\} + \left\{\frac{\partial f}{\partial\sigma}\right\}\{d\Delta\gamma\} = \{d\varepsilon^e_{tr}\} \tag{4.34}$$

and

$$\left\{\frac{\partial f}{\partial\sigma}\right\}^T\{d\sigma\} = 0 \tag{4.35}$$

by combining these equations and separating the change in stress and the change in increment in plastic multiplier we can obtain

$$\begin{bmatrix} [C^e] + \Delta\gamma\left\{\frac{\partial^2 f}{\partial\sigma^2}\right\} & \left\{\frac{\partial f}{\partial\sigma}\right\} \\ \left\{\frac{\partial f}{\partial\sigma}\right\}^T & 0 \end{bmatrix}\begin{Bmatrix} \{d\sigma\} \\ \{d\Delta\gamma\} \end{Bmatrix} = \begin{Bmatrix} \{d\varepsilon^e_{tr}\} \\ 0 \end{Bmatrix}. \tag{4.36}$$

where the matrix on the lefthand side is $[A^{alg}]^{-1}$. Both sides of (4.36) can be multiplied by $[A^{alg}]$ in order to calculate the consistent tangent.

$$\begin{Bmatrix} \{d\sigma\} \\ \{d\Delta\gamma\} \end{Bmatrix} = \begin{bmatrix} [D^{alg}] & \{A^{alg}_{12}\} \\ \{A^{alg}_{21}\}^T & A^{alg}_{22} \end{bmatrix}\begin{Bmatrix} \{d\varepsilon^e_{tr}\} \\ 0 \end{Bmatrix}. \tag{4.37}$$

$[D^{alg}]$ is the top left submatrix of $[A^{alg}]$. The derivatives needed for this calculation are required to be in the final converged state, however these already exist due to the implicit

stress integration procedure needing the derivatives at every iteration.

4.2 Large deformation iGIMP with elasto-plasticity

In Chapter 3 an updated Lagrangian finite deformation formulation was introduced where a relationship between the logarithmic strain and Kirchhoff stress at each material point was used. For large deformation elasto-plasticity this relationship will be modified so that the Kirchhoff stresses $\{\tau\}$ are now related to the elastic part of the logarithmic strains $\{\varepsilon^{\mathrm{e}}\}$

$$\{\tau\} = [D^{\mathrm{e}}]\{\varepsilon^{\mathrm{e}}\}. \tag{4.38}$$

The Cauchy stress can be still be obtained from the Kirchhoff stress using

$$\{\sigma\} = J^{-1}\{\tau\}. \tag{4.39}$$

It is now assumed that the deformation gradient can be multiplicatively split into elastic and plastic components [97, 98]

$$[F] = [F^{\mathrm{e}}][F^{\mathrm{p}}], \tag{4.40}$$

Using this, the elastic left Cauchy-Green strain can be calculated from the elastic part of the deformation gradient as

$$[b^{\mathrm{e}}] = [F^{\mathrm{e}}][F^{\mathrm{e}}]^T. \tag{4.41}$$

The logarithmic strain can then be calculated from the elastic-left Cauchy green strain as

$$\{\varepsilon^{\mathrm{e}}\} = \frac{1}{2}\ln([b^{\mathrm{e}}]). \tag{4.42}$$

Each of the parts of the deformation gradient can be further split as with the full deformation gradient into rotational and stretch components

$$[F^{\mathrm{e}}] = [R^{\mathrm{e}}][U^{\mathrm{e}}] = [V^{\mathrm{e}}][R^{\mathrm{e}}] \quad \text{and} \quad [F^{\mathrm{p}}] = [R^{\mathrm{p}}][U^{\mathrm{p}} = [V^{\mathrm{p}}][R^{\mathrm{p}}] \tag{4.43}$$

An intermediate ('stress free') state will be introduced where only the plastic part of the deformation gradient is applied. This can be seen in Figure 4.5. In order to describe the elasto-plastic behaviour, the plastic velocity gradient $[L^p]$, which describes the rate of

plastic deformation in this intermediate state, will be introduced as

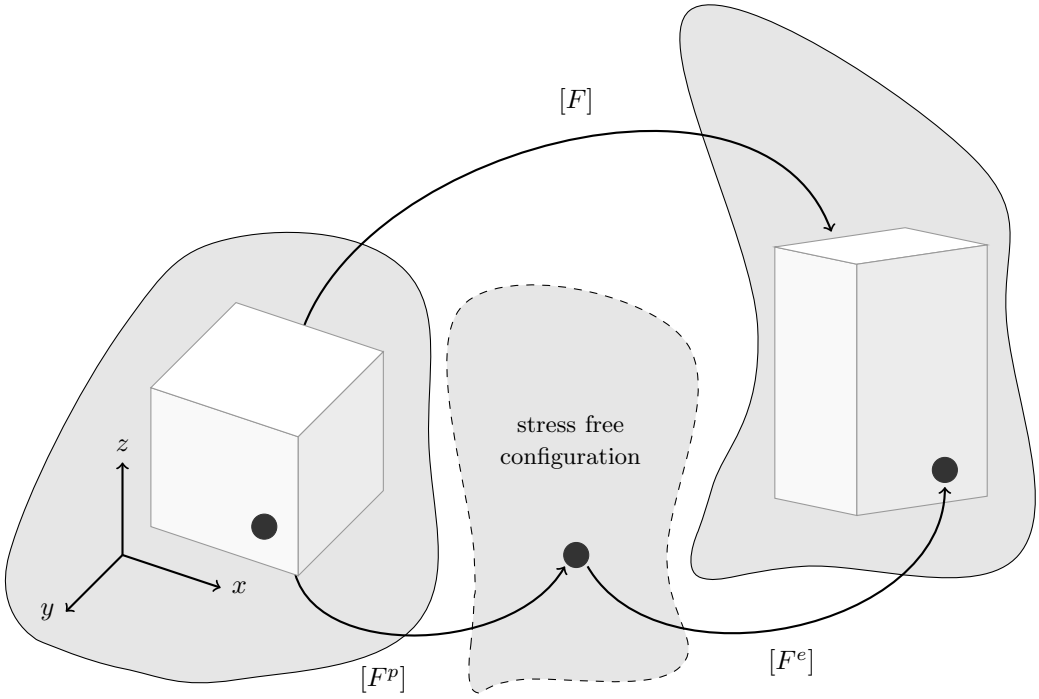

Figure 4.5: stress free configuration

$$[L^p] = [\dot{F}^p][F^p]^{-1}, \tag{4.44}$$

where $[\dot{F}^p]$ is the rate of change of the plastic deformation gradient. This can be mapped into the current configuration by $[R^e]$,

$$[\tilde{L}^p] = [R^e][L^p][R^e]^T \tag{4.45}$$

so that $[\tilde{L}^p]$ is now the rate of change of plastic deformation in the current configuration. At this point we use the assumption of plastic isotropy which means there will be zero plastic spin, that is $[\tilde{L}^p]$ will be symmetric, and from this we are able to introduce a finite strain associated plastic flow rule to describe this rate of change of plastic deformation

$$[\tilde{L}^p] = \dot{\gamma} \left\{ \frac{\partial f}{\partial \tau} \right\}. \tag{4.46}$$

This can be mapped back into the stress free configuration to give

$$[\dot{F}^p][F^p]^{-1} = [R^e]^T \dot{\gamma} \left\{ \frac{\partial f}{\partial \tau} \right\} [R^e]. \tag{4.47}$$

In order to approximate the plastic flow equation an implicit exponential map integrator concept is used, where an equation of the form $\dot{Y}(t) = A(t)Y(t)$ with initial conditions $Y(t_0) = Y_0$ can be approximated as $Y_{n+1} = \exp[\Delta t A_{n+1}]Y_n$, more details can be found in [53] amongst others. Making use of this and the fact that for orthogonal tensors $\exp([Q][\cdot][Q]^T) = [Q]\exp[\cdot][Q]^T$ can give the current plastic deformation gradient $[F^p_{n+1}]$ as

$$[F^p_{n+1}] = [R^e_{n+1}]^T \exp\left[\Delta\gamma \left. \frac{\partial f}{\partial \tau} \right|_{n+1} \right] [R^e_{n+1}][F^p_n]. \tag{4.48}$$

Combining the multiplicative decompositions (4.40) and (3.24) and rearranging making use of the fact that $[R]^T = [R]^{-1}$, the elastic deformation gradient can be written as

$$[F^e_{n+1}] = [\Delta F][F^e_n][R^e_{n+1}]^T \exp\left[-\Delta\gamma \left. \frac{\partial f}{\partial \tau} \right|_{n+1} \right] [R^e_{n+1}]. \tag{4.49}$$

This return mapping equation in terms of elastic deformation gradient which needs to be solved if $\Delta\gamma > 0$ can be significantly simplified by rearranging it in terms of logarithmic strains. The first step to this is to multiply both sides by $[R^e_{n+1}]^T$ to obtain

$$[V^e_n + 1] = [F^e_t][R^e_{n+1}]^T \exp\left[-\Delta\gamma \left. \frac{\partial f}{\partial \tau} \right|_{n+1} \right]. \tag{4.50}$$

Multiplication by the transpose of each side gives

$$[V^e_{n+1}] \exp\left[2\Delta\gamma \left. \frac{\partial f}{\partial \tau} \right|_{n+1} \right] [V^e_{n+1}] = ([V^{etr}_{n+1}])^2, \tag{4.51}$$

after which rearranging and taking square roots gives

$$[V^e_{n+1}] = [V^e_{tr}] \exp\left[-\Delta\gamma \left. \frac{\partial f}{\partial \tau} \right|_{n+1} \right], \tag{4.52}$$

and taking logarithms of both sides gives

$$\{\varepsilon^e_{n+1}\} = \{\varepsilon^e_{tr}\} - \Delta\gamma \left\{ \frac{\partial f}{\partial \tau} \right\} \tag{4.53}$$

which is the same format as (4.22) and the derivative of the deformation gradient is taken in the current state. This means that the conventional small strain constitutive model and the NR method used to solve the return mapping equations in Section 4.1 can be used within a finite deformation framework, but with logarithmic strains and Kirchhoff stresses. A major advantage of this choice of finite deformation framework is that the algorithm here does not change provided that the stress and strain measures are combined with the exponential map of the plastic flow equation. Because of the similarities between the iGIMP structure and that of FEM it is possible to use existing constitutive models without modification.

In order to include the elasto-plastic constitutive model in the iGIMP method given in Chapter 3, some minor modifications are required. Namely, the constitutive model will now take a trial elastic strain and material properties as inputs. The updated stress, updated elastic strain and $[D^{\text{alg}}]$ consistent with the stress integration used in the constitutive model, will be returned for use in the rest of the method.

To compute the trial elastic left Cauchy-Green strain ($[b^{\text{e}}_{tr}]$) (where the subscript tr denotes trial) needed as the initial estimate for the constitutive model for the current iteration, we need to calculate the elastic left Cauchy-Green strain tensor ($[b^{\text{e}}_n)]$ from the previously converged loadstep

$$[b^{\text{e}}_n] = \exp\big(2\{\varepsilon^{\text{e}}_n\}\big) \tag{4.54}$$

where the subscript n denotes the previously converged state (at the end of the previous loadstep). The trial elastic left Cauchy-Green strain can then be calculated (by assuming that the whole step will be elastic) from

$$[b^{\text{e}}_{tr}] = [\Delta F][b^{\text{e}}_n][\Delta F]^T, \tag{4.55}$$

where $[\Delta F]$ is the increment in the deformation gradient for the current loadstep (see Chapter 3). The trial elastic strain needed to compute the Kirchhoff stress using the

constitutive model can then be obtained using

$$\{\varepsilon^{\mathrm{e}}_{tr}\} = \frac{1}{2}\ln([b^{\mathrm{e}}_{tr}]). \tag{4.56}$$

At this point the method outlined in Chapter 3 can be followed to solve the system. It should be noted that as long as the algorithmic tangent consistent with the stress integration algorithm is used, asymptoticly quadratic convergence will still be achieved [157]. The iGIMP algorithm including the outlined elasto-plastic model is given in Algorithm 4.1. This replaces the material point loop Algorithm 3.2 introduced in Chapter 3. It is emphasised that it is possible to replace the material model with other models such as those presented in [25] to allow both elastic and plastic anisotropy, however this is not within the scope of this thesis.

Algorithm 4.1 Implicit GIMP algorithm with elasto-plastic material model.

i	1	2	$...n_{mp}$	FOR EACH Material Point		
$[\Delta F]$				deformation gradient increment	$[\Delta F_{n+1}] = [1] + \left[\frac{\partial \Delta u_{n+1}}{\partial \tilde{X}}\right]$	(3.25)
$[F]$				updated deformation gradient	$[F_{n+1}] = [\Delta F_{n+1}][F_n]$	(3.24)
$[b]$				trial elastic left Cauchy Green strain	$[b^e_t] = [\Delta F_{n+1}][b^e_n][\Delta F_{n+1}]^T$	(4.55)
$[\varepsilon^e_t]$				logarithmic elastic trial strain	$[\varepsilon^e_t] = \frac{1}{2}\log([b^e_t])$	(4.42)
$[\tau], [\varepsilon^e]$				Kirchhoff stress and elastic logarithmic strain	use small strain constitutive model (Algorithm 4.2)	
$[\sigma]$				Cauchy stress	$[\sigma] = J^{-1}[\tau]$	(4.39)
$[b^{\mathrm{e}}]$				left elastic cauchy green strain	$[b^{\mathrm{e}}_{n+1}] = \exp\big(2[\varepsilon^{\mathrm{e}}_{n+1}]\big)$	(4.54)
$[D^{cst}]$				spatial tangent	$[D^{cst}] = \frac{1}{2J}[D^{\mathrm{alg}}][L^D][B^D] - [S^D],$	(3.20)
nels	1	2	$...n_{els}$	FOR EACH overlapping element		
$[G]$				strain displacement matrix	$[G] = \left[\frac{\partial S^a_{vp1}}{\partial \tilde{X}}\right][\Delta F]^{-1} \ldots$	(3.29)
$\{f^{int}_p\}$				particle internal force	$\{f^{int}_p\} = [G]^T\{\sigma\}V_p$	(3.23)
$[K_p]$				particle stiffness	$[K_p] = [G]^T[D^{cst}][G]V_p$	(3.10)

Material model

Algorithm 4.2 Small strain constitutive model.

Inputs				$\{\varepsilon^e_{tr}\}$,E,v,ρ_y	
$[D^e], [C^e]$				Calculate $[D^e]$ and its inverse $[C^e]$ from E and v	2.3
$\{\sigma_{tr}\}$				calculate trial stress $\{\sigma_{tr}\} = [D^e]\{\varepsilon^e_{tr}\}$	(4.17)
f				evaluate yield function based on trial stress $f = \sqrt{3J_2}$	(4.15)
				IF $f \leq 0$	
$\{\sigma\}$				update stress $\{\sigma\} = \{\sigma_{tr}\}$	
$\{\varepsilon^e\}$				update elastic strain $\{\varepsilon^e\} = \{\varepsilon^e_{tr}\}$	
$[D^{alg}]$				update algorithmic consistent tangent $[D^{alg}] = [D^e]$	
				ELSE ($f > 0$)	
$\left\{\frac{\partial f}{\partial \sigma}\right\}, \left\{\frac{\partial^2 f}{\partial \sigma^2}\right\}$				Calculate derivatives of the yield function	
$NRit$	1	2	...	WHILE $\lvert\{\mathrm{b}\}\rvert < tol$	
$[A]$				calculate Hessian matrix $[A] = \begin{bmatrix} \left[\frac{\partial b_1}{\partial \varepsilon^e}\right] & \left\{\frac{\partial b_1}{\partial \Delta\gamma}\right\} \\ \left\{\frac{\partial b_2}{\partial \varepsilon^e}\right\}^T & \frac{\partial b_2}{\partial \Delta\gamma} \end{bmatrix}$	(4.26)
$\{dx\}$				calculate increment $\{dx\} = [A]^{-1}\{b\}$	(4.27)
$\{\varepsilon^e\}, d\gamma$				update elastic strain and increment in plastic multiplier $\{x_{k+1}\} = \{x_k\} + \{dx\}$	
$\{b\}$				update residuals $\varepsilon^e - \varepsilon^e_{tr} + \gamma \left\{\frac{\partial f}{\partial \sigma}\right\}, \sqrt{3J_2}$	4.25
$[D^{alg}]$				calculate $[D^{alg}]$ consistent with the updated stress state, see Section 4.1.1 $[D^{alg}] = \left[\frac{\{d\sigma\}}{\{d\varepsilon^e_{tr}\}}\right]$	(4.29)
Outputs				$\{\varepsilon^e\}$,$[D^{alg}]$,$\{\sigma\}$	

4.3 Numerical examples

In this section examples will be presented to demonstrate the iGIMP method combined with the elasto-plastic material behaviour introduced in Section 4.2.

4.3.1 Column under selfweight

A column with the same geometry as in Chapters 2 and 3, height 50 units under self weight with a body force of 40000 units and a Young's modulus of $E = 10^6$, is now investigated but this time using the von Mises constitutive model outlined in Section 4.1.1

with a deviatoric yield stress of $\rho_y = 3 \times 10^4$. The material will yield when $\tau_{zz} = \rho_y$ which should occur at a position of $Z = l_0 - \frac{\rho_y}{\rho_o b_0}$ which can be obtained by rearranging the elastic analytical solution and solving for the yield stress. The elasto-plastic behaviour will introduce stresses in the out of plane directions τ_{xx} and τ_{yy}, below this position. It should be noted that the displacements and total strains (elastic and plastic strains do develop but the combined resulting strain is zero) in these directions are still enforced as zero as a consequence of modelling in one dimension. These stresses will be equal due to the boundary conditions that are applied so here on, τ_{yy} will be not be discussed as it is equal to τ_{xx}. It is possible to write the deviatoric stress in this situation as

$$\rho = |\tau_{xx} - \tau_{zz}|. \tag{4.57}$$

The vertical stress τ_{zz} should still follow the analytical solution given in Chapter 3, however in the section near the base of the column where the yield stress is reached, stresses will appear in the out of plane direction. This is shown in Figure 4.6 where it can be seen that in the elasto-plastic region (grey shaded region on the figure) there are stresses in both the vertical and horizontal directions. The analytical solution for these out of plane stresses can be arrived at using knowledge of the deformation, and from this a relationship can be found between elastic parts of the deformation gradient (see A.10 for further details)

$$F^e_{xx} = F^e_{zz} e^{\frac{\rho_y}{E}}. \tag{4.58}$$

In the vertical direction, it can also be observed that a relationship between plastic and elastic components of the deformation gradient exists as

$$F^p_{zz} = {F^e_{zz}}^2 e^{\frac{2\rho_y}{E}}. \tag{4.59}$$

The Cauchy stress can then be given in the vertical direction as

$$\sigma_{zz} = \frac{1}{{F^e_{zz}}^3 e^{(\frac{2\rho_y}{E})}} E \ln(F^e_{zz}). \tag{4.60}$$

where F^e_{zz} can be obtained from knowledge of σ_{zz} from the elastic solution. This result allows F^e_{zz} to be calculated using a Newton process which yields F_{zz} using (4.59). F^e_{xx} can

also be calculated using (4.58) which allows the calculation of

$$\sigma_{xx} = \frac{1}{F_{zz}} E \ln(F^e_{xx}). \tag{4.61}$$

The derivation for this can be found in [30] but has been included as Appendix A to assist the reader.

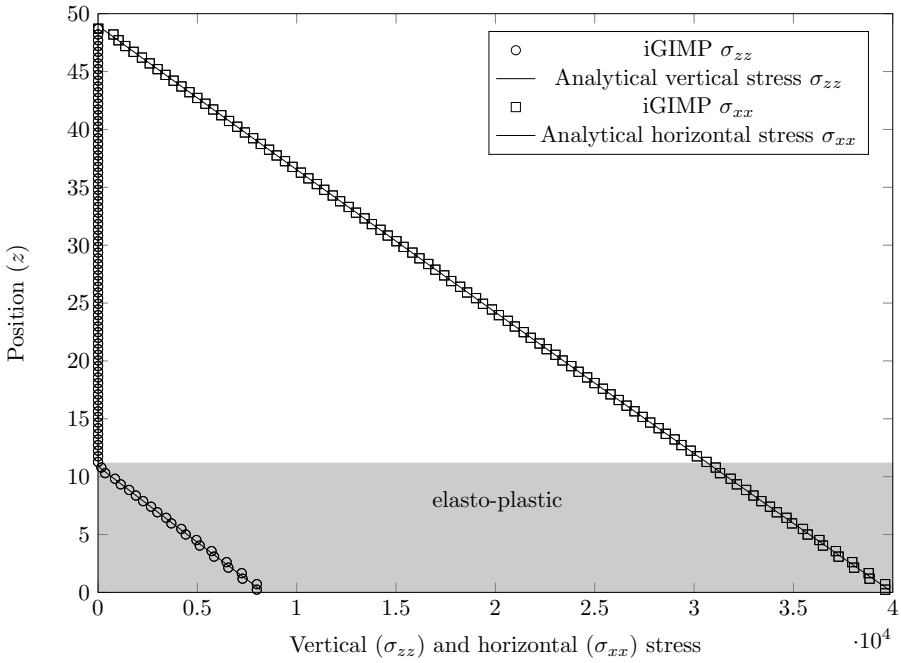

Figure 4.6: Plot of vertical and horizontal stress against analytical solution 1D column with elasto-plastic behaviour.

The problem was repeated with an increased body force of 400000. The stresses here, shown in Figure 4.7, also show close agreement with the analytical solution. The convergence for these simulations with increased numbers of background grid elements is shown in Figure 4.8, where the same behaviour can be observed as in the elastic case. It was not possible to plot the convergence for quadratic finite elements for this problem as locking was experienced when using a 3 x 3 quadrature scheme and machine precision was reached with reduced integration with a single step.

4.3.2 Collapse of strip footing

The second example consists of a footing, of width 1 m, displaced downwards into a soil assumed to be an infinite medium. Only half of the cross section is modelled due to symmetry using a 5 m x 5 m square of soil and a 0.5 m footing as can be seen in

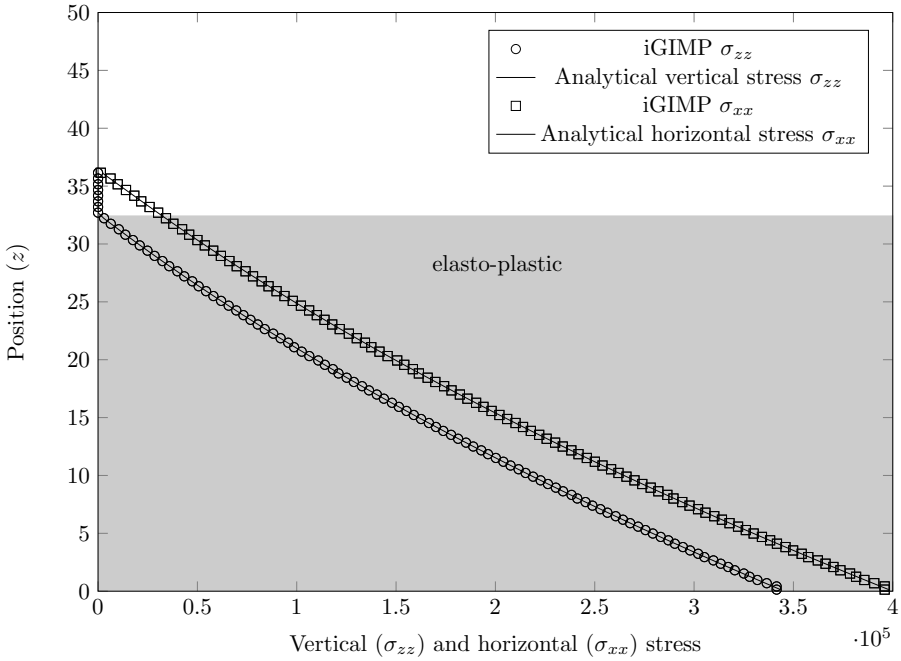

Figure 4.7: Plot of vertical and horizontal stress against analytical solution 1D column with elasto-plastic behaviour undergoing larger deformation.

Figure 4.9. The shading shows the level of plastic strain. The von Mises perfectly plastic model introduced in Section with a Young's modulus of $E = 1 \times 10^7$kPa, Poisson's ratio of $\nu = 0.48$ and a yield stress of $\sigma_y = 848.7$kPa. It is possible to model this in 2D due to the plain strain assumptions, assuming that the footing is long, which is the same problem (and parameters) as shown in De Souza Neto [53]. The total displacement applied is $u = 0.002$m over 20 loadsteps. Figure 4.10 shows the normalised pressure plotted against the normalised settlement for the footing. It can be seen here that the iGIMP results agree well with those achieved using linear FEM using the same background mesh. According to [53] the normalised limit pressure ($P/(\frac{\sigma_y}{\sqrt{3}})$ should equal 5.14 however this value is not achieved using the iGIMP method. It is possible to achieve more accurate results by refining the background grid, however a key reason for this is the occurrence of volumetric locking in problems such as this. In the FEM by using quadratic elements with reduced integration this problem can be avoided, but this cannot be done using the iGIMP formulation used here. A solution to this problem would be to implement an $\bar{F}$ approach as done in [43]. In this paper the first author extended the iGIMP method developed in this thesis to overcome locking in the MPM. However, as the novel contributions for this paper were not work of the author of this thesis, this work will not be included here.

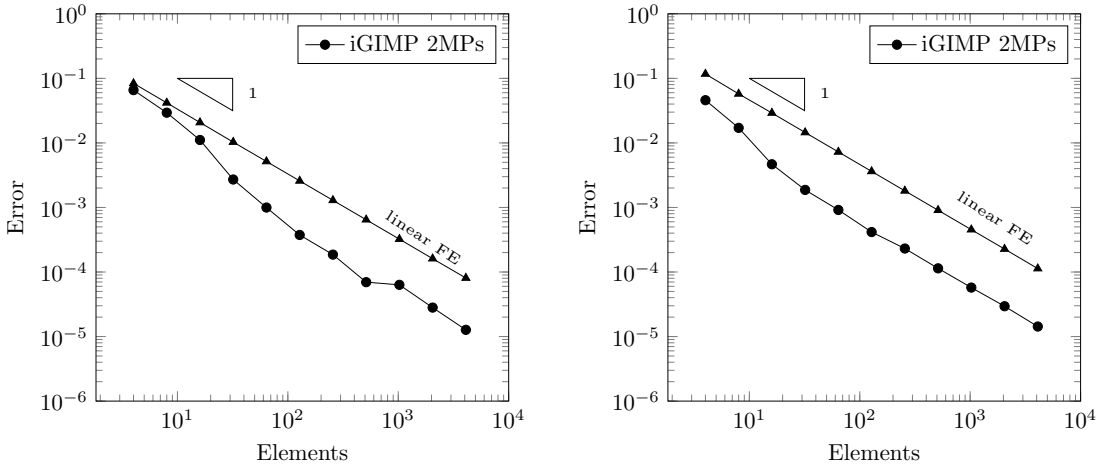

(a) $w = 40,000$ (b) $w = 400,000$

Figure 4.8: Convergence study for 1D column under self weight with elasto-plastic behaviour.

4.4 Observations

In this chapter the basic theory of elasto-plasticity has been introduced to enable the introduction of different constitutive models into the iGIMP method in the same way as in the FEM. The concept of a yield surface was explained and the four key components of small strain elasto-plasticity were introduced. The stress integration return mapping procedure and the importance of a consistent tangent were also explained. This was then combined into the large deformation iGIMP algorithm presented in Chapter 3 resulting in a large deformation implicit GIMP method with elasto-plasticity which was first published in the literature by the author in [30]. The method was then demonstrated with a numerical example using a von Mises yield surface, showing agreement with an analytical solution and convergence with increasing degrees of freedom. A further example showed good agreement with linear FEM but showed that the GIMP method suffers from volumetric locking. The approach developed over the previous two chapters has been shown to work successfully by agreeing well with analytical solutions for large deformation and elasto-plasticity problems however as shown in [186] the MPM becomes mesh dependent for problems involving localisations. The next chapter will investigate a gradient plasticity as one possible approach to overcome this.

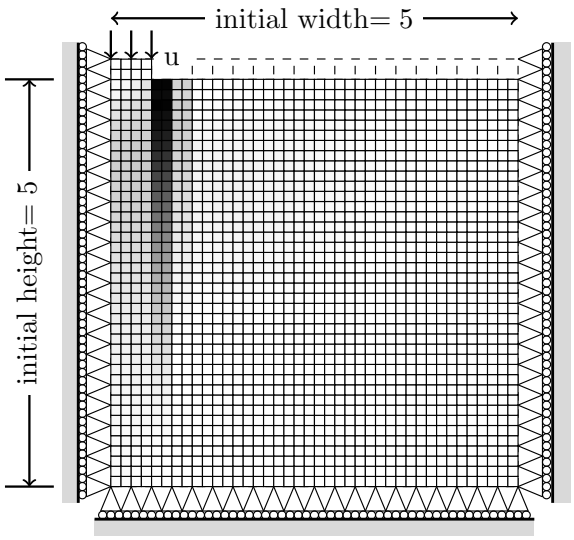

Figure 4.9: Plastic strain around displaced footing

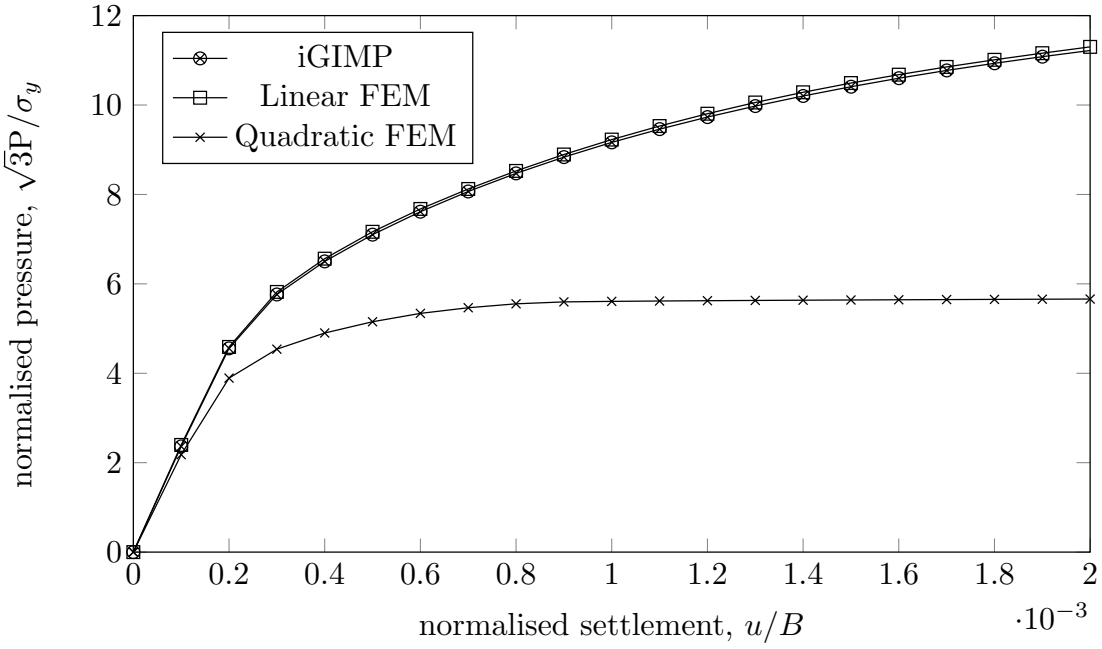

Figure 4.10: Normalised settlement against normalised pressure for displaced footing

Chapter 5

Gradient elasto-plasticity

In the previous chapters the Generalised Interpolation Material Point (GIMP) method has been implemented for large deformations and elasto-plasticity. However, such conventional continuum analysis techniques constructed in terms of stress and strain are unable to resolve structural instabilities such as necking or shear banding. This is due to the fact that they do not contain any measure of the length of the microstructure of the material analysed such as molecule size of the grain structure. Because of this, the result is that as the background grid is refined in the conventional Material Point Method (MPM) the width of the shear band is continually reduced based on the mesh discretisation [23]. Addressing this problem is not a new area of interest, with much research in the area using a variety of different approaches including non-local methods [61, 141], couple stress theory [178, 179], and gradient theories [51, 66]. The purpose of this chapter is not to give a comprehensive review of techniques for dealing with these types of localisations — some methods are compared in [50] — but to demonstrate how existing theory can be combined with the MPM and GIMP methods.

Some existing work on non-local methods used with the MPM has been done, for example [23] and [73] which have both been used to tackle problems such as slope stability. This method works by material points influencing neighbouring material points. This chapter presents, for the first time, a gradient elasto-plastic theory based MPM. The framework used was previously presented in [29].

In this chapter, an introduction to gradient theories will be given in Section 5.1 before outlining the theory of the gradient approach used in Section 5.2. Section 5.3 describes

in detail the Hermitian shape functions which are required for the gradient plasticity approach adopted before aspects of the implementation are discussed in Section 5.4. Finally, Section 5.5 will show numerical examples to verify the approach.

5.1 Gradient theories

Gradient elasticity theories are an extension of classical elasticity equations to account for microstructure of a material by considering higher order derivatives — usually higher order derivatives of displacement or strain. The phrase 'gradient' comes from these higher order terms being proportional to the Laplacian of lower order terms. Theories relating to enriching elasticity equations by capturing effects of microstructure using higher order gradients can be seen as far back as the 19th [26] and early 20th [47] centuries. More interest in the area developed in the 1960s when studies [128, 129, 178, 179] began to extend previous approaches into elaborate full gradient theories, a landmark paper being Mindlin [127]. In modern times there has been another shift of interest towards simplified theories [2, 60]. This simplification allows for easier implementation with the popular Finite Element Method (FEM), an example of this being the Ru-Aifantis theorem [150]. This allowed the initial method [127] which was very complex with almost 2000 coefficients to be reduced to a simple two step process with a single length scale parameter. An overview of gradient elasticity can be found in [8].

5.1.1 Gradient plasticity

For the types of problem we are interested in modelling, such as shear bands, a gradient elasto-plasticity approach is more appropriate. It is possible to extend gradient elasticity to plasticity as in [148] however, within gradient plasticity there are multiple approaches to take. One approach to gradient elasto-plasticity takes the same idea of incorporating higher order derivatives, this time into a elasto-plasticity framework rather than an elastic one and taking derivatives of the plastic multiplier. Fleck and Hutchinson propose another variety of gradient plasticity in [66–68]. However it is the formulation of De Borst *et al.* [51] which will be adopted in this work. This approach includes a single length scale which is incorporated into the yield function and will be explained in the section below. The gradients here are only associated with the plastic part of the model meaning that the elastic response is not altered. A disadvantage of this is that it is necessary to identify the

elastic-plastic boundary which is not trivial in general examples.

5.2 Elasto-plastic gradient approach used with iGIMP

The approach described below follows that of De Borst and Mühlhaus [51]. Usually in computational plasticity it is necessary to integrate (4.11) to provide an incremental relationship between stress and strain (see Chapter 4 for further details), however here the plastic multipliers ($\dot{\gamma}$) is treated as an independent unknown solved for at nodes in addition to the nodal displacements. This results in the yield condition only being satisfied, in a weak sense, at the end of a loadstep, not in every iteration as in the method used in the previous chapter. With this formulation, where the plastic consistency parameter is solved alongside displacements, it is necessary to make the yield strength dependent not only on the plastic strain, but also its Laplacian. The starting point for this formulation is

$$[L]^T\{\dot{\sigma}\} + \{f_b\} = \{0\}, \tag{5.1}$$

where $\{\sigma\}$ is the Cauchy stress and can be calculated using the elastic strain and $[L]$ is the differential operator as explained in (2.5). Integrating over the volume and multiplying by a test function $\{\partial u\}$ gives

$$\int_v \{\partial u\}[L]^T\{\dot{\sigma}\} + \{\partial u\}^T\{f_b\}dv = 0, \tag{5.2}$$

which using Gauss-Green theorem can be expressed as

$$\int_v \{\partial\varepsilon\}^T\{\dot{\sigma}\}dv - \int_s \{\partial u\}^T\{\dot{t}\}ds - \int_v \{\partial u\}^T\{f_b\}dv = 0, \tag{5.3}$$

where $\dot{t}$ is the rate of change of the tractions and $\partial\varepsilon$ is obtained as the derivative of the test function. Making use of the plastic flow rule and additive decomposition previously introduced in (4.12) and (4.13) the stress can be written as

$$\{\dot{\sigma}\} = [D^e]\left\{\{\dot{\varepsilon}\} - \dot{\gamma}\left\{\frac{\partial f}{\partial\sigma}\right\}\right\}, \tag{5.4}$$

where $[D^e]$ is the elastic material stiffness matrix, $\dot{\gamma}$ is the rate of change of the plastic multiplier and $\left\{\frac{\partial f}{\partial\sigma}\right\}$ is the flow direction which is calculated as the derivative of the yield

function with respect to stress (assuming associated flow). Together the rate of change of the plastic multiplier and the flow direction give the rate of change of plastic strain $\dot{\varepsilon}^p$. Substituting this into (5.3) we arrive at

$$\int_v \{\partial\varepsilon\}^T [D^e] \left\{ \{\dot{\varepsilon}\} - \dot{\gamma} \left\{ \frac{\partial f}{\partial \sigma} \right\} \right\} dv - \int_s \{\partial u\}^T \{\dot{t}\} ds - \int_v \{\partial u\}^T \{f_b\} dv = 0. \tag{5.5}$$

In addition to this standard equation a global equation must be constructed to relating to the plastic multiplier. The starting point for this is the consistency condition introduced in Chapter 4, again repeated here to aid the reader

$$\dot{\gamma} f = 0. \tag{5.6}$$

It is known that if a material is behaving elasto-plasticly its stress state must lie on the yield surface and remain on the yield surface

$$f = 0 \quad \text{and} \quad \dot{f} = 0. \tag{5.7}$$

By writing expressing the yield function as not only dependent on stress but also the plastic multiplier and its Laplacian

$$f(\sigma, \gamma, \nabla^2\gamma) = 0, \tag{5.8}$$

it is possible to express $\dot{f}$ as

$$\dot{f} = \left\{ \frac{\partial f}{\partial \sigma} \right\} \dot{\sigma} + \frac{\partial f}{\partial \gamma} \dot{\gamma} + \frac{\partial f}{\partial \nabla^2 \gamma} \dot{\nabla^2 \gamma} = 0 \tag{5.9}$$

By defining a hardening parameter as

$$H = -\frac{\partial f}{\partial \gamma} \tag{5.10}$$

and a gradient parameter as

$$c = \frac{\partial f}{\partial \nabla^2 \gamma} \tag{5.11}$$

it is possible to write

$$\left\{\frac{\partial f}{\partial \sigma}\right\}\dot{\sigma} - H\gamma + c\nabla^2\gamma = 0. \tag{5.12}$$

By substituting (5.4) into (5.12) it is possible to obtain

$$\left\{\frac{\partial f}{\partial \sigma}\right\}^T [D^e]\left\{\{\varepsilon\} - \gamma\left\{\frac{\partial f}{\partial \sigma}\right\}\right\} - H\gamma + c\nabla^2\gamma = 0, \tag{5.13}$$

from which one can obtain the weak form

$$\int_v \partial\gamma\left[\left\{\frac{\partial f}{\partial \sigma}\right\}^T [D^e]\left\{\{\varepsilon\} - \gamma\left\{\frac{\partial f}{\partial \sigma}\right\}\right\} - H\gamma + c\nabla^2\gamma\right] dv = 0. \tag{5.14}$$

Displacements at the grid $\{u_g\}$ are mapped to displacements at the material points $\{u_p\}$ as before using the GIMP shape functions (S_{vp})

$$\{u_p\} = [S_{vp}]\{u_g\}. \tag{5.15}$$

By computing the strain displacement matrix $[B]$ from

$$[B] = [L]\{S_{vp}\}, \tag{5.16}$$

strains can be calculated by

$$\{\varepsilon\} = [B]\{u_g\}. \tag{5.17}$$

Due to (5.14) including the Laplacian of the plastic multiplier, γ must be mapped using C1 continuous shape functions [51]. As suggested in [51], Hermitian shape functions will be used to achieve this. A further explanation of Hermitian shape functions is given in Section 5.3.1. The resulting mappings are then

$$\gamma_p = \{h\}^T\{\Lambda_g\} \tag{5.18}$$

and

$$\nabla^2\gamma_p = \{p\}^T\{\Lambda_g\} \tag{5.19}$$

where p are the Laplacians of h and $\{\Lambda_g\}$ are the nodal values of the plastic multipliers and their derivatives. Introducing (5.18) into (5.5) gives

$$\{\partial u\}^T \int_v [B]^T [D^e] \left\{ [B]\{u_g\} - \left(\{h\}^T \{\Lambda_g\}\right) \left\{ \frac{\partial f}{\partial \sigma} \right\} \right\} dv - \{\partial u\}^T \int_s \{S_{vp}\}^T \{t\} ds \\ - \{\partial u\}^T \int_v \{S_{vp}\}^T \{f_b\} dv = 0 \quad (5.20)$$

and substituting (5.18) and (5.19) into (5.14) gives

$$\delta\Lambda_g \int_v \{h\}^T \left\{ \frac{\partial f}{\partial \sigma} \right\} [D] \left\{ [B]\{u_g\} - \{h\}^T \{\Lambda_g\} \left\{ \frac{\partial f}{\partial \sigma} \right\} \right\} - H\{h\} \left(\{h\}^T \{\Lambda_g\}\right) \\ + c\{h\} \left(\{p\}^T \{\Lambda_g\}\right) dv = -\delta\Lambda \int_v \{h\} f(\sigma_n) dv. \quad (5.21)$$

Eliminating $\partial\varepsilon$ and $\partial\gamma$, these become

$$\int_v [B]^T [D^e] \left\{ [B]\{u_g\} - \left(\{h\}^T \{\Lambda_g\}\right) \left\{ \frac{\partial f}{\partial \sigma} \right\} \right\} dv = \int_s \{S_{vp}\}^T \{t\} ds + \int_v \{S_{vp}\}^T \{f_b\} dv \quad (5.22)$$

and

$$\int_v \{h\} \frac{\partial f}{\partial \sigma}^T [D] \left\{ [B]\{u_g\} - \{h\}^T \{\Lambda_g\} \left\{ \frac{\partial f}{\partial \sigma} \right\} \right\} - \{h\} H \{h\}^T \{\Lambda_g\} \\ + c\{h\}\{p\}^T \{\Lambda_g\} dv + \int_v \{h\} f(\sigma_n) dv = 0. \quad (5.23)$$

Equations (5.22) and (5.23) can be combined into a coupled system written as

$$\begin{bmatrix} [K_{aa}] & [K_{a\lambda}] \\ [K_{a\lambda}]^T & [K_{\lambda\lambda}] \end{bmatrix} \begin{bmatrix} \{u_g\} \\ \{\Lambda_g\} \end{bmatrix} = \begin{Bmatrix} \int_s [S_{vp}]^T \{t\} ds + \int_v [S_{vp}]^T \{f_b\} dv \\ \int_v \{h\} f(\sigma_n) dv \end{Bmatrix}, \quad (5.24)$$

where

$$[K_{aa}] = \int_v [B]^T [D^e] [B] dv \quad (5.25)$$

$$[K_{a\lambda}] = -\int_v [B]^T [D^e] \{f_{,\sigma}\} \{h\}^T dv, \quad (5.26)$$

and

$$[K_{\lambda\lambda}] = \int_v \{h\} \{f_{,\sigma}\}^T [D^e] \{f_{,\sigma}\} \{h\}^T + \{h\} H \{h\}^T - c\{h\}\{p\}^T dv. \quad (5.27)$$

where $\{\frac{\partial f}{\partial \sigma}\}$ has been written as $\{f_{,\sigma}\}$ for conciseness in this case. The first term in (5.27) introduces the plastic behaviour, the second term relates to the hardening effects and the third term the gradient effects. By setting c and H to zero, (5.24) reduces to standard elasto-plasticity, however it should be noted that the yield function is only satisfied in an average sense.

5.3 Hermitian shape functions

In this section the Hermitian shape functions used in this approach to give C1 continuity will be introduced. Hermitian shape functions are constructed of two parts which are used with a nodal value and its spatial derivative, this is similar to beam elements. They will first be introduced in one dimension as the two dimensional shape functions can be calculated by multiplying 1D Hermitian functions.

5.3.1 1D Hermitian shape functions

Consider the element shown in Figure 5.1, with degrees of freedom plastic multiplier Λ and its derivative with respect to the x direction, $\Lambda_{,x}$ at nodes 1 and 2, at local coordinates -1 and 1. These can be written as:

$$\{\Lambda\} = \{\Lambda_1 \quad \Lambda_{,x1} \quad \Lambda_2 \quad \Lambda_{,x2}\}^T \tag{5.28}$$

It is possible to calculate the plastic multiplier at a point within the element γ using

$$\gamma = \{h\}^T \{\Lambda_g\} \tag{5.29}$$

where $\{h\}$ are Hermitian shape functions given by

$$\{h\} = \{h_1 \quad h_{,x1} \quad h_2 \quad h_{,x2}\}^T. \tag{5.30}$$

The Hermitian shape functions can first be calculated in a local coordinate system ($-1 < \xi < 1$ in 1D) as

$$\{\tilde{h}\} = \{\tilde{h}_1 \quad \tilde{h}_{,\xi 1} \quad \tilde{h}_2 \quad \tilde{h}_{,\xi 2}\}^T. \tag{5.31}$$

Figure 5.1: 1D element with degrees of freedom to be used with Hermitian shape functions.

where

$$\tilde{h}_1 = \frac{1}{4}(1-\xi)^2(2+\xi) \qquad \tilde{h}_2 = \frac{1}{4}(1+\xi)^2(2-\xi). \tag{5.32}$$

and

$$\tilde{h}_{,\xi 1} = \frac{1}{4}(\xi+1)(1-\xi)^2 \qquad \tilde{h}_{,\xi 2} = \frac{1}{4}(\xi-1)(1+\xi)^2. \tag{5.33}$$

These shape functions can be seen in Figure 5.3.1. Subfigure (a) shows the Hermitian shape functions (5.32) and (b) shows their derivatives (5.32) in the local coordinate system. $\{h\}$ in global coordinates can be recovered using

$$\{h\} = \left\{ \tilde{h}_1 \quad \tilde{h}_{,\xi 1}\frac{\partial x}{\partial \xi} \quad \tilde{h}_2 \quad \tilde{h}_{,\xi 2}\frac{\partial x}{\partial \xi} \right\}^T \tag{5.34}$$

It can be seen that the value of the Hermitian shape function in (a) is equal to the slope in

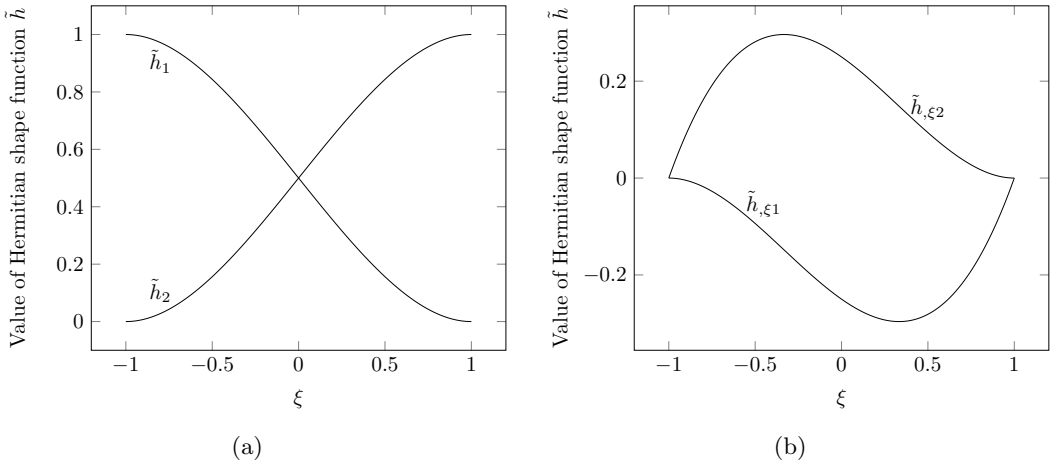

Figure 5.2: Hermitian shape functions in 1D showing (a) $\tilde{h}_i$ and (b) $\tilde{h}_{,\xi i}$.

(b). The Laplacian of the plastic multiplier $\nabla^2\gamma$ is needed for the gradient formulation. In 1D this is equivalent to the second derivative $\gamma_{,xx}$. In order to calculate this, the Laplacian of these shape functions are needed too. This is why it is necessary to have C1 continuous

shape functions. $\nabla^2\gamma$ can be calculated as

$$\nabla^2\gamma = \{p\}^T\{\Lambda\} \tag{5.35}$$

where

$$\{p\} = \{p_1 \quad p_{,x1} \quad p_2 \quad p_{,x2}\}^T = \frac{\partial^2}{\partial x^2}\{h\}. \tag{5.36}$$

As with the standard hermitian functions these can be calculated in a local coordinate system as

$$\{\tilde{p}\} = \{\tilde{p}_1 \quad \tilde{p}_{,\xi 1} \quad \tilde{p}_2 \quad \tilde{p}_{,\xi 2}\}^T = \frac{\partial^2}{\partial \xi^2}\{\tilde{h}\}, \tag{5.37}$$

where

$$\tilde{p}_1 = \frac{3}{2}\xi \qquad \tilde{p}_2 = -\frac{3}{2}\xi. \tag{5.38}$$

and

$$\tilde{p}_{,\xi 1} = -\frac{1}{2} + \frac{3}{2}\xi \qquad \tilde{p}_{,\xi 2} = \frac{1}{2} + \frac{3}{2}\xi. \tag{5.39}$$

These second derivatives can be seen in Figure 5.3. It is again possible to express $\{p\}$ in

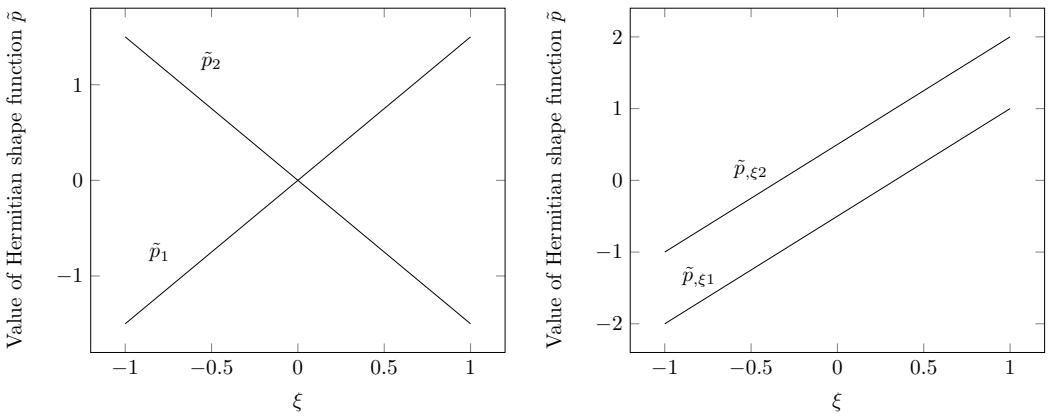

Figure 5.3: Hermitian shape function Laplacians in 1D showing (a) $\tilde{p}_i$ and (b) $\tilde{p}_{,\xi i}$..

the global coordinates this time through

$$\{p\} = \left(\frac{\partial \xi}{\partial x}\right)^2 \left\{\tilde{p} \quad \tilde{p}_{,\xi 1}\frac{\partial x}{\partial \xi} \quad \tilde{p}_2 \quad \tilde{p}_{,\xi 2}\frac{\partial x}{\partial \xi}\right\}. \tag{5.40}$$

5.3.2 2D Hermitian shape functions

In two dimensions using 4 noded quadrilateral elements we have degrees of freedom at each node of displacements u and v (which are mapped using the GIMP shape functions as introduced previously in Chapter 3), and plastic multiplier γ, its derivative with respect to x and y, γ, x and γ, y and the derivative with respect to both x and y, γ, xy. Written out for one element these are

$$\{\Lambda\} = \{\Lambda_1 \;\; \Lambda_{,x1} \;\; \Lambda_{,y1} \;\; \Lambda_{,xy1} \;\; \Lambda_2 \;\; \Lambda_{,x2} \;\; \Lambda_{,y2} \;\; \Lambda_{,xy2} \;\; \Lambda_3 \;\; \Lambda_{,x3} \;\; \Lambda_{,y3} \;\; \Lambda_{,xy3} \;\; \Lambda_4 \;\; \Lambda_{,x4} \;\; \Lambda_{,y4} \;\; \Lambda_{,xy4}\}^T \tag{5.41}$$

this will be shortened to

$$\{\Lambda\} = \{\Lambda_i \quad \Lambda_{,xi} \quad \Lambda_{,yi} \quad \Lambda_{,xyi}\}^T \tag{5.42}$$

where i represents each of the nodes. These can be seen in the element shown in Figure 5.4 using clockwise node numbering. As in the 1D case, the plastic multiplier at a given

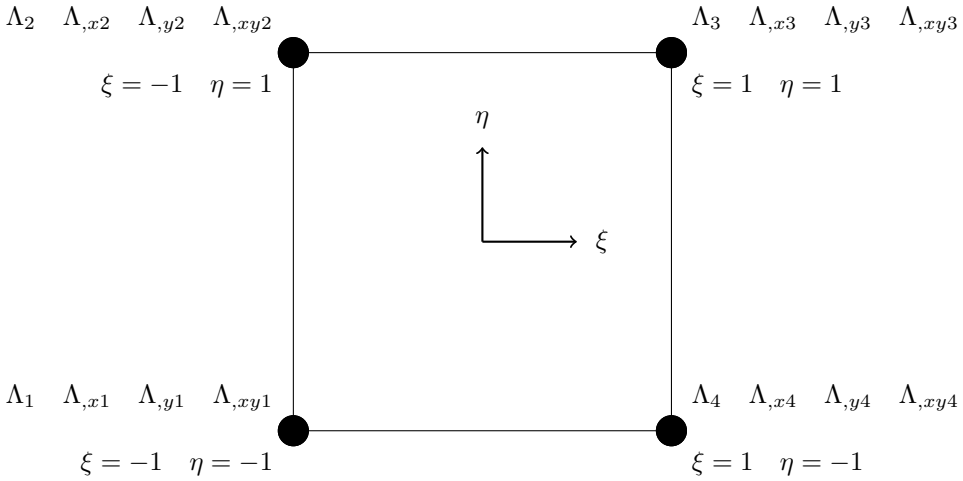

Figure 5.4: 2D element with degrees of freedom to be used with Hermitian shape functions.

point can be calculated as

$$\gamma = \{h\}^T\{\Lambda\} \tag{5.43}$$

where

$$\{h\} = \{h_i \;\; h_{,xi} \;\; h_{,yi} \;\; h_{,xyi}\}^T. \tag{5.44}$$

these can be calculated in the local coordinates ξ and η as

$$\{\tilde{h}\} = \{\tilde{h}_i \;\; \tilde{h}_{,\xi i} \;\; \tilde{h}_{,\eta i} \;\; \tilde{h}_{,\xi\eta i}\}^T. \tag{5.45}$$

where $\{\tilde{h}\}$ can be calculated by taking the product of 1D Hermitian shape functions (5.34)

$$\begin{aligned}
\tilde{h}_i &= \tilde{h}_{i(\xi)}\tilde{h}_{i(\eta)} \\
\tilde{h}_{,\xi i} &= \tilde{h}_{,\xi i(\xi)}\tilde{h}_{i(\eta)} \\
\tilde{h}_{,\eta i} &= \tilde{h}_{i(\xi)}\tilde{h}_{,\eta i(\eta)} \\
\tilde{h}_{,\xi\eta i} &= \tilde{h}_{,\xi i(\xi)}\tilde{h}_{,\eta i(\eta)}.
\end{aligned} \tag{5.46}$$

where the 1D functions can be calculated based on the local coordinates in each direction. This gives the following functions

$$\begin{aligned}
\tilde{h}_1 &= \frac{1}{16}(1-\xi)^2(2+\xi)(1-\eta)^2(2+\eta) \\
\tilde{h}_2 &= \frac{1}{16}(1-\xi)^2(2+\xi)(1+\eta)^2(2-\eta) \\
\tilde{h}_3 &= \frac{1}{16}(1+\xi)^2(2-\xi)(1+\eta)^2(2-\eta) \\
\tilde{h}_4 &= \frac{1}{16}(1+\xi)^2(2-\xi)(1-\eta)^2(2+\eta).
\end{aligned} \tag{5.47}$$

$$\begin{aligned}
\tilde{h}_{,\xi 1} &= \frac{1}{16}(\xi+1)(1-\xi)^2(1-\eta)(2+\eta)^2 \\
\tilde{h}_{,\xi 2} &= \frac{1}{16}(\xi+1)(1-\xi)^2(1+\eta)(2-\eta)^2 \\
\tilde{h}_{,\xi 3} &= \frac{1}{16}(\xi-1)(1+\xi)^2(1+\eta)(2-\eta)^2 \\
\tilde{h}_{,\xi 4} &= \frac{1}{16}(\xi-1)(1+\xi)^2(1-\eta)(2+\eta)^2
\end{aligned} \tag{5.48}$$

$$\begin{aligned}
\tilde{h}_{,\eta 1} &= \frac{1}{16}(1-\xi)(2+\xi)^2(\eta+1)(1-\eta)^2 \\
\tilde{h}_{,\eta 2} &= \frac{1}{16}(1-\xi)(2+\xi)^2(\eta-1)(1+\eta)^2 \\
\tilde{h}_{,\eta 3} &= \frac{1}{16}(1+\xi)(2-\xi)^2(\eta-1)(1+\eta)^2 \\
\tilde{h}_{,\eta 4} &= \frac{1}{16}(1+\xi)(2-\xi)^2(\eta+1)(1-\eta)^2.
\end{aligned} \tag{5.49}$$

$$\begin{aligned}
\tilde{h}_{,\xi\eta 1} &= \frac{1}{16}(\xi+1)(1-\xi)^2(\eta+1)(1-\eta)^2 \\
\tilde{h}_{,\xi\eta 2} &= \frac{1}{16}(\xi+1)(1-\xi)^2(\eta-1)(1+\eta)^2 \\
\tilde{h}_{,\xi\eta 3} &= \frac{1}{16}(\xi-1)(1+\xi)^2(\eta-1)(1+\eta)^2 \\
\tilde{h}_{,\xi\eta 4} &= \frac{1}{16}(\xi-1)(1+\xi)^2(\eta+1)(1-\eta)^2.
\end{aligned} \tag{5.50}$$

These can be mapped back to the global coordinates through

$$\{h\} = \left\{ \tilde{h}_i \quad \tilde{h}_{,\xi i}\frac{\partial x}{\partial \xi} \quad \tilde{h}_{,\eta i}\frac{\partial y}{\partial \eta} \quad \tilde{h}_{,\xi\eta i}\frac{\partial x}{\partial \xi}\frac{\partial y}{\partial \eta} \right\}^T. \tag{5.51}$$

One key point here is that the mapping of $\tilde{h}_{,\xi\eta i}$ is a special case, as in the iGIMP method it can be ensured that the background grid is always rectangular. This is a specific advantage when compared to the FEM where the elements cannot be guaranteed to be rectangular. This means that derivatives $\frac{\partial x}{\partial \eta}$ and $\frac{\partial y}{\partial \xi}$ that would otherwise contribute to a more complicated expression are equal to zero and can be omitted. These functions can be seen in Figure 5.3.2.

The property of being able to guarantee a regular rectangular mesh also simplifies the Laplacian of the shape functions which in 2D are

$$\nabla^2\gamma = \gamma_{,xx} + \gamma_{,yy} \tag{5.52}$$

and can be calculated from the nodal values as

$$\nabla^2\gamma = \{p\}^T\{\Lambda\} \tag{5.53}$$

where

$$\{p\} = \frac{\partial^2}{\partial x^2}\{h\} + \frac{\partial^2}{\partial y^2}\{h\}. \tag{5.54}$$

The second order derivatives can be calculated in local coordinates as

$$\{\tilde{p}\} = \underbrace{\frac{\partial^2}{\partial \xi^2}\{\tilde{h}\}}_{\{\tilde{p^1}\}} + \underbrace{\frac{\partial^2}{\partial \eta^2}\{\tilde{h}\}}_{\{\tilde{p^2}\}} \tag{5.55}$$

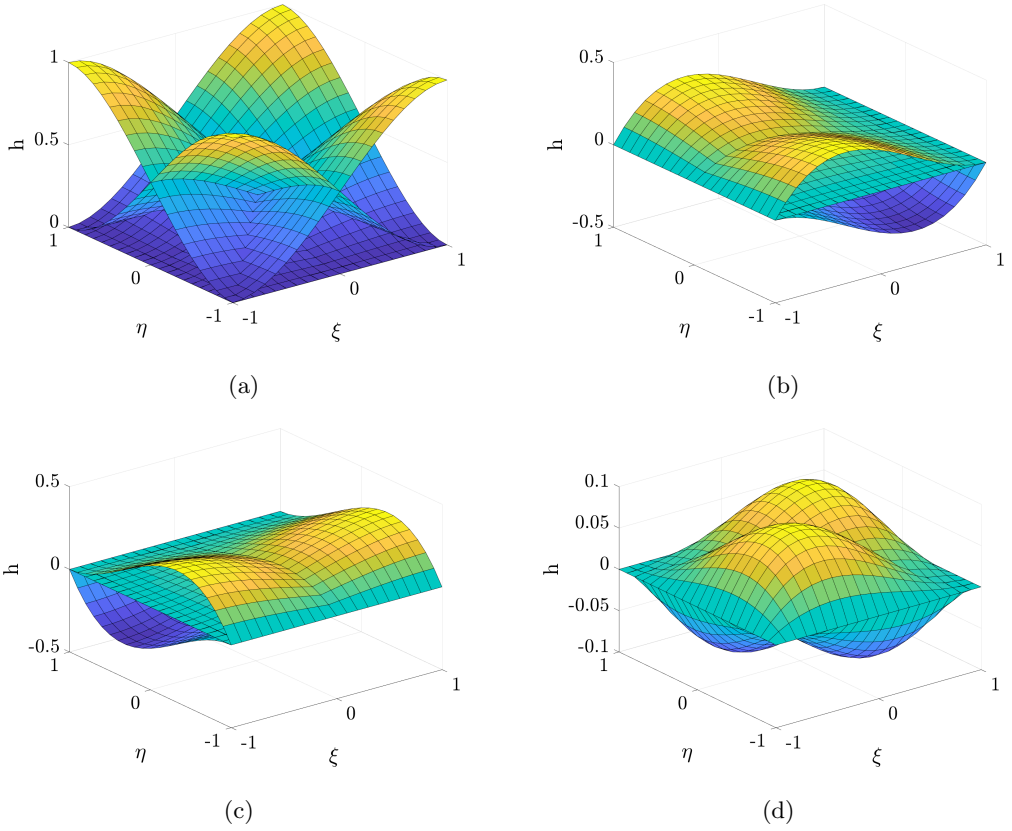

Figure 5.5: Hermitian shape functions in a 2D element. (a) showing $\tilde{h}$, (b) showing $\tilde{h}_{,\xi}$, (c) showing $\tilde{h}_{,\eta}$ and (d) showing $\tilde{h}_{,\xi\eta}$.

where $\{\tilde{p}\}$ can be calculated by taking the product of 1D Hermitian shape functions (5.37)

$$\begin{aligned}
\tilde{p}^1_i &= \tilde{p}_{i(\xi)}\tilde{h}_{i(\eta)} & \tilde{p}^2_i &= \tilde{h}_{i(\xi)}\tilde{p}_{i(\eta)} \\
\tilde{p}^1_{,\xi i} &= \tilde{p}_{,\xi i(\xi)}\tilde{h}_{i(\eta)} & \tilde{p}^2_{,\xi i} &= \tilde{h}_{,\xi i(\xi)}\tilde{p}_{i(\eta)} \\
\tilde{p}^1_{,\eta i} &= \tilde{p}_{i(\xi)}\tilde{h}_{,\eta i(\eta)} & \tilde{p}^2_{,\eta i} &= \tilde{h}_{i(\xi)}\tilde{p}_{,\eta i(\eta)} \\
\tilde{p}^1_{,\xi\eta i} &= \tilde{p}_{,\xi i(\xi)}\tilde{h}_{,\eta i(\eta)} & \tilde{p}^2_{,\xi\eta i} &= \tilde{p}_{,\eta i(\eta)}\tilde{h}_{,\xi i(\xi)}.
\end{aligned} \tag{5.56}$$

where the 1D functions can be calculated based on the local coordinates in each direction. This gives the following 2D functions and derivatives

$$\begin{aligned}
\tilde{p}^1_1 &= \frac{3}{8}\xi(1-\eta)^2(2+\eta) & \tilde{p}^2_1 &= \frac{3}{8}\eta(1-\xi)^2(2+\xi) \\
\tilde{p}^1_2 &= \frac{3}{8}\xi(1+\eta)^2(2-\eta) & \tilde{p}^2_2 &= \frac{3}{8}\eta(1+\xi)^2(2-\xi) \\
\tilde{p}^1_3 &= -\frac{3}{8}\xi(1+\eta)^2(2-\eta) & \tilde{p}^2_3 &= -\frac{3}{8}\eta(1+\xi)^2(2-\xi) \\
\tilde{p}^1_4 &= -\frac{3}{8}\xi(1-\eta)^2(2+\eta) & \tilde{p}^2_4 &= -\frac{3}{8}\eta(1-\xi)^2(2+\xi).
\end{aligned} \tag{5.57}$$

$$
\begin{aligned}
\tilde{p}^1_{,\xi 1} &= (\frac{3}{8}\xi - \frac{1}{8})(1-\eta)(2+\eta)^2 & \tilde{p}^2_{,\xi 1} &= \frac{3}{8}\eta(\xi+1)(1-\xi)^2 \\
\tilde{p}^1_{,\xi 2} &= (\frac{3}{8}\xi - \frac{1}{8})(1+\eta)(2-\eta)^2 & \tilde{p}^2_{,\xi 2} &= \frac{3}{8}\eta(\xi-1)(1+\xi)^2 \\
\tilde{p}^1_{,\xi 3} &= (\frac{3}{8}\xi + \frac{1}{8})(1+\eta)(2-\eta)^2 & \tilde{p}^2_{,\xi 3} &= -\frac{3}{8}\eta(\xi-1)(1+\xi)^2 \\
\tilde{p}^1_{,\xi 4} &= (\frac{3}{8}\xi + \frac{1}{8})(1-\eta)(2+\eta)^2 & \tilde{p}^2_{,\xi 4} &= -\frac{3}{8}\eta(\xi+1)(1-\xi)^2.
\end{aligned} \tag{5.58}
$$

$$
\begin{aligned}
\tilde{p}^1_{,\eta 1} &= \frac{3}{8}\xi(\eta+1)(1-\eta)^2 & \tilde{p}^2_{,\eta 1} &= (\frac{3}{8}\eta - \frac{1}{8})(1-\xi)(2+\xi)^2 \\
\tilde{p}^1_{,\eta 2} &= \frac{3}{8}\xi(\eta-1)(1+\eta)^2 & \tilde{p}^2_{,\eta 2} &= (\frac{3}{8}\eta - \frac{1}{8})(1+\xi)(2-\xi)^2 \\
\tilde{p}^1_{,\eta 3} &= -\frac{3}{8}\xi(\eta-1)(1+\eta)^2 & \tilde{p}^2_{,\eta 3} &= (\frac{3}{8}\eta + \frac{1}{8})(1+\xi)(2-\xi)^2 \\
\tilde{p}^1_{,\eta 4} &= -\frac{3}{8}\xi(\eta+1)(1-\eta)^2 & \tilde{p}^2_{,\eta 4} &= (\frac{3}{8}\eta + \frac{1}{8})(1-\xi)(2+\xi)^2.
\end{aligned} \tag{5.59}
$$

$$
\begin{aligned}
\tilde{p}^1_{,\xi\eta 1} &= (\frac{3}{8}\xi - \frac{1}{8})(\eta+1)(1-\eta)^2 & \tilde{p}^2_{,\xi\eta 1} &= (\frac{3}{8}\eta - \frac{1}{8})(\xi+1)(1-\xi)^2 \\
\tilde{p}^1_{,\xi\eta 2} &= (\frac{3}{8}\xi - \frac{1}{8})(\eta-1)(1+\eta)^2 & \tilde{p}^2_{,\xi\eta 2} &= (\frac{3}{8}\eta - \frac{1}{8})(\xi-1)(1+\xi)^2 \\
\tilde{p}^1_{,\xi\eta 3} &= (\frac{3}{8}\xi + \frac{1}{8})(\eta-1)(1+\eta)^2 & \tilde{p}^2_{,\xi\eta 3} &= (\frac{3}{8}\eta + \frac{1}{8})(\xi-1)(1+\xi)^2 \\
\tilde{p}^1_{,\xi\eta 4} &= (\frac{3}{8}\xi + \frac{1}{8})(\eta+1)(1-\eta)^2 & \tilde{p}^2_{,\xi\eta 4} &= (\frac{3}{8}\eta + \frac{1}{8})(\xi+1)(1-\xi)^2.
\end{aligned} \tag{5.60}
$$

The local functions can be seen below in Figure 5.3.2. These functions can be mapped back to the global coordinates and combined through

$$
\begin{aligned}
\{p\}^T = \left(\frac{\partial \xi}{\partial x}\right)^2 \left\{ \tilde{p}^1_i \quad \tilde{p}^1_{,\xi i}\frac{\partial x}{\partial \xi} \quad \tilde{p}^1_{,\eta i}\frac{\partial y}{\partial \eta} \quad \tilde{p}^1_{,\xi\eta i}\frac{\partial x}{\partial \xi}\frac{\partial y}{\partial \eta} \right\} \\
+ \left(\frac{\partial \eta}{\partial y}\right)^2 \left\{ \tilde{p}^2_i \quad \tilde{p}^2_{,\xi i}\frac{\partial x}{\partial \xi} \quad \tilde{p}^2_{,\eta i}\frac{\partial y}{\partial \eta} \quad \tilde{p}^2_{,\xi\eta i}\frac{\partial x}{\partial \xi}\frac{\partial y}{\partial \eta} \right\}.
\end{aligned} \tag{5.61}
$$

It will now be shown how these Hermitian functions are used in the implementation of the gradient approach with the GIMP method. More information on hermitian functions can be found in [59] and [9].

5.4 Implementation

To implement the approach with the GIMP method, incremental values for the stress and plastic multiplier must be used as the primary unknowns in the non-linear problem as the background grid is reset after each step. The stresses can be calculated from the elastic strain which can be calculated from the previous elastic strain, plus the increment

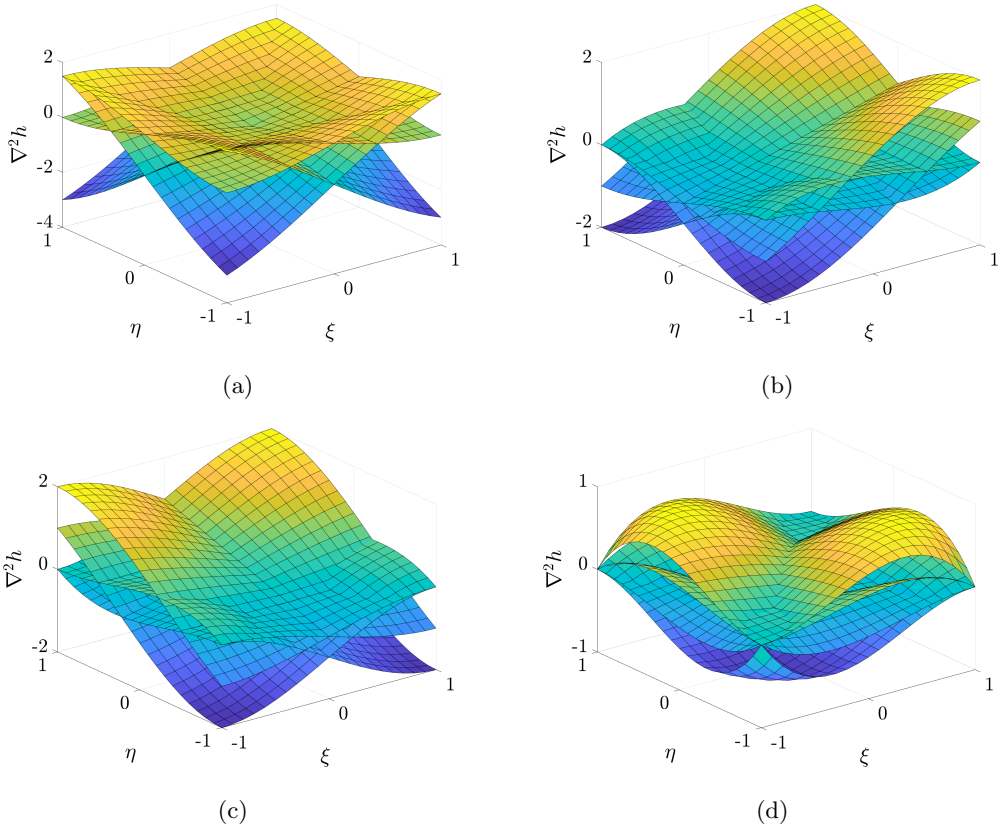

Figure 5.6: Hermitian shape function Laplacianss in a 2D element. (a) showing $\nabla^2\tilde{h}$, (b) showing $\nabla^2\tilde{h}_{,\xi}$, (c) showing $\nabla^2\tilde{h}_{,\eta}$ and (d) showing $\nabla^2\tilde{h}_{,\xi\eta}$..

associated with the current loadstep, minus any increment in plastic straining, that is

$$\{\varepsilon^e_{n+1}\} = \{\varepsilon^e_n\} + \{\Delta\varepsilon\} - \Delta\gamma\{f_{,\sigma}\}, \tag{5.62}$$

where n refers to the value at the end of the previous load step. The current Cauchy stress can be obtained from

$$\{\sigma_{n+1}\} = \{\sigma_n\} + \{\Delta\sigma\} \tag{5.63}$$

where

$$\{\Delta\sigma\} = [D^e]\{\{\Delta\varepsilon\} - \Delta\gamma\{f_{,\sigma}\}\}. \tag{5.64}$$

The plastic multiplier in a similar manner becomes

$$\gamma_{n+1} = \gamma_n + \Delta\gamma. \tag{5.65}$$

Using these increments, an incremental form of the weak statement of equilibrium can be expressed as

$$\int_v \{\partial\varepsilon\}^T [D^e] \left\{ \{\Delta\varepsilon\} - \Delta\gamma \left\{ \frac{\partial f}{\partial \sigma} \right\}^T \right\} dv + \int_v \partial\{\varepsilon\}^T \{\sigma_n\} dv \\ - \int_s \{\partial u\}^T \{t\} ds - \int_v \{\partial u\}^T \{f_b\} dv = \{0\}. \quad (5.66)$$

Taking a Taylor series expansion of the volume averaged version of (5.6) and ignoring higher order terms it is possible to arrive at

$$\int_v \partial\gamma \left\{ \frac{\partial f}{\partial \sigma} \right\}^T \{\Delta\sigma\} dv = -\int_v \partial\gamma f(\sigma_n) dv. \quad (5.67)$$

introducing the incremental relationship (5.64) into this results in

$$\int_v \delta\gamma \{f_{,\sigma}\}^T [D^e] (\{\Delta\varepsilon\} - \Delta\gamma \{f_{,\sigma}\}) dv = -\int_v \delta\gamma f(\sigma_n) dv. \quad (5.68)$$

Using the substitutions (5.17) and (5.18) as above and eliminating $\delta\gamma$ from (5.68) and substituting $\{\delta\varepsilon\} = [B]\delta u$ and eliminating $\{\delta u\}$ from (5.66) gives the following equations (with the size of each component below, asssuming no material point domains overlapping multiple elements)

$$\int_v \underbrace{[B]^T}_{8\times3} \underbrace{[D^e]}_{3\times3} \underbrace{[B]}_{3\times8} dv \underbrace{\{\Delta u_g\}}_{8\times1} - \int_v \underbrace{[B]^T}_{8\times3} \underbrace{[D^e]}_{3\times\mathbf{6}} \underbrace{\{f_{,\sigma}\}}_{\mathbf{6}\times1} \underbrace{\{h\}^T}_{1\times16} dv \underbrace{\{\Delta\Lambda\}}_{16\times1} \\ = \int_s \underbrace{[S_{vp}]^T}_{8\times2} \underbrace{\{t\}}_{2\times1} ds + \int_v \underbrace{[S_{vp}]^T}_{8\times2} \underbrace{\{f_b\}}_{2\times1} dv - \int_v \underbrace{[B]^T}_{8\times3} \underbrace{\{\sigma_n\}}_{3\times1} dv \quad (5.69)$$

and

$$-\int_v \underbrace{\{h\}}_{16\times1} \underbrace{\{f_{,\sigma}\}^T}_{1\times\mathbf{6}} \underbrace{[D^e]}_{\mathbf{6}\times3} \underbrace{[B]}_{3\times8} dv \underbrace{\{\Delta u_g\}}_{8\times1} + \int_v \underbrace{\{h\}}_{16\times1} \underbrace{\{f_{,\sigma}\}^T}_{1\times\mathbf{6}} \underbrace{[D^e]}_{\mathbf{6}\times\mathbf{6}} \underbrace{\{f_{,\sigma}\}}_{\mathbf{6}\times1} \underbrace{\{h\}^T}_{1\times16} dv \underbrace{\{\Delta\Lambda\}}_{16\times1} \\ = \int_v \underbrace{\{h\}}_{16\times1} \underbrace{f(\sigma_n)}_{1\times1} dv, \quad (5.70)$$

where the right hand side of 5.74 is the residual in terms of the plastic multiplier. These equations can be re-written as a coupled system

$$\begin{bmatrix} [K_{aa}] & [K_{a\lambda}] \\ [K_{a\lambda}]^T & [K_{\lambda\lambda}] \end{bmatrix} \begin{Bmatrix} \{\Delta d\} \\ \{\Delta\Lambda\} \end{Bmatrix} = \begin{Bmatrix} \int_s [S_{vp}]^T \{t\} ds + \int_v [S_{vp}]^T \{f_b\} dv \\ \int_v \{h\} f(\sigma_n) dv \end{Bmatrix}, \tag{5.71}$$

where $[K]$ is as in (5.25) to (5.27) but now acting on incremental values of displacement and plastic multipler. The consistent tangent must also be updated, according to [52] this is given by

$$[D^{alg}] = \left[[D^e]^{-1} + d\gamma \left[\frac{\partial^2 f}{\partial \sigma^2} \right] \right]^{-1} \tag{5.72}$$

An outline of the algorithm for gradient plasticity with the iGIMP method can be found in Algorithms 5.1 and 5.2. A key consideration, which may not be immediately clear and is different from using a standard return mapping algorithm, is that the flow direction $\{f_{,\sigma}\}$ must be calculated and stored in full even when not simulating 3D problems. This is because of the way the yield function is coupled in with the global equations so it is not possible to ignore terms in direction not of interest. This can be highlighted by considering the sizes of each of the components of (5.73) and (5.74) in the 2D case shown above with how it reduces in the 1D equivalent

$$\begin{aligned} \int_v \underbrace{[B]^T}_{2\times1} \underbrace{[D^e]}_{1\times1} \underbrace{[B]}_{1\times2} dv \underbrace{\{\Delta u_g\}}_{2\times1} - \int_v \underbrace{[B]^T}_{2\times1} \underbrace{[D^e]}_{1\times\mathbf{6}} \underbrace{\{f_{,\sigma}\}}_{\mathbf{6}\times1} \underbrace{\{h\}^T}_{1\times4} dv \underbrace{\{\Delta\Lambda\}}_{4\times1} \\ = \int_s \underbrace{[S_{vp}]^T}_{2\times1} \underbrace{\{t\}}_{1\times1} ds + \int_v \underbrace{[S_{vp}]^T}_{2\times1} \underbrace{\{f_b\}}_{1\times1} dv - \int_v \underbrace{[B]^T}_{2\times1} \underbrace{\{\sigma_n\}}_{1\times1} dv \end{aligned} \tag{5.73}$$

and

$$\begin{aligned} - \int_v \underbrace{\{h\}}_{4\times1} \underbrace{\{f_{,\sigma}\}^T}_{1\times\mathbf{6}} \underbrace{[D^e]}_{\mathbf{6}\times1} \underbrace{[B]}_{1\times2} dv \underbrace{\{\Delta u_g\}}_{2\times1} + \int_v \underbrace{\{h\}}_{4\times1} \underbrace{\{f_{,\sigma}\}^T}_{1\times\mathbf{6}} \underbrace{[D^e]}_{\mathbf{6}\times\mathbf{6}} \underbrace{\{f_{,\sigma}\}}_{\mathbf{6}\times1} \underbrace{\{h\}^T}_{1\times4} dv \underbrace{\{\Delta\Lambda\}}_{4\times1} \\ = \int_v \underbrace{\{h\}}_{4\times1} \underbrace{f(\sigma_n)}_{1\times1} dv, \end{aligned} \tag{5.74}$$

The terms in bold are highlighted to emphasise that they do not change between 1D and 2D.

Algorithm 5.1 Gradient plasticity iGIMP algorithm

$lstp$	1	2	...lstps	FOR EACH Loadstep		
				Calculate which elements each particle overlaps, and therefore free degrees of freedom		
$\{f^{ext}_{n+1}\}$				increment and map the external forces	$\{f^{ext}_g\} = \{f^{ext}_p\}[S_{vp}]$	(2.19)*
$NRit$	1	2	...	WHILE $\|f^R\| < tol$		
$\{\Delta u_g\}$				solve for displacements, now including lam	$\{\delta u_{k+1}\} = [K]^{-1}\{f^R_k\}$, $\{\Delta u_{k+1}\} = \{\Delta u_k\} + \{\delta u_{k+1}\}$	(3.17)
$\{\Delta u_p\}$				particle displacement	$\{\Delta u_p\} = [S_{vp}]\{\Delta u_g\}$	(2.25)*
i	1	2	$...n_{mp}$	FOR EACH Material point		
$nels$	1	2	$...n_{els}$	FOR EACH overlapping element		
$[B]$				strain displacement matrix	$[B] = \left[\frac{\partial S^a_{vp1}}{\partial \tilde{X}}\right] \dots$	(3.29)
i	1	2	$...n_{mp}$	FOR EACH Material point		
				Algorithm 5.2		
$\{f^\lambda\}$				calculate plastic multiplier residual term	$\{f^\lambda\} = \{h\}f$	
$\{f^{int}_p\}$				particle internal force	$\{f^{int}_p\} = [B]^T\{\sigma\}V_p$	(3.23)
$[K_{aa}]$				particle stiffness linking displacement DoF	$[B]^T[D^e][B]V_p$	(5.25)
$[K_{a\lambda}]$				particle stiffness coupling terms	$-[B]^T[D^e]\{f_{,\sigma}\}\{h\}^T V_p$	(5.26)
$[K_{\lambda\lambda}]$				particle stiffness linking plastic multiplier terms	$\{h\}\{f_{,\sigma}\}^T[D^e]\{f_{,\sigma}\}\{h\}^T + \{h\}H\{h\}^T - c\{h\}\{p\}^T V_p$	(5.27)
$\{f^R\}$				out of balance force	$\{f^R\} = \{f^{int}; f^\lambda\} - \{f^{ext}\}$	
$\{x^{n+1}_p\}$				update particle positions	$\{x^{n+1}_p\} = \{x^n_p\} + \{u_p\}$	(2.26)

Algorithm 5.2 Gradient material point loop and constitutive model

$\{h\}$				calculate hermitian shape functions	$\left\{\tilde{h}_1 \quad \tilde{h}_{,\xi 1}\frac{\partial x}{\partial \xi} \quad \tilde{h}_2 \quad \tilde{h}_{,\xi 2}\frac{\partial x}{\partial \xi}\right\}^T$	(5.30)
$\{p\}$				calculate laplacian hermitian shape functions	$\left(\frac{\partial \xi}{\partial x}\right)^2\left\{\tilde{p} \quad \tilde{p}_{,\xi 1}\frac{\partial x}{\partial \xi} \quad \tilde{p}_2 \quad \tilde{p}_{,\xi 2}\frac{\partial x}{\partial \xi}\right\}$	(5.40)
$d\gamma$				calculate increment in plastic multiplier	$d\gamma = \{h\}^T\{\Lambda_g\}$	(5.18)
$d\nabla^2\gamma$				calculate increment in laplacian of plastic multiplier	$d\nabla^2\gamma = \{p\}^T\{\Lambda_g\}$	(5.19)
$\{\varepsilon^e_{tr}\}$				calculate trial elastic strain increment	$\{\varepsilon^e_{tr}\} = \{\varepsilon^e\} + [B]\{\Delta u_g\}.$	(5.17)
$[D^e], [C^e]$				Calculate $[D^e]$ and its inverse $[C^e]$ from E and v		(2.3)
$\{\sigma_{tr}\}$				calculate trial stress	$\{\sigma_{tr}\} = [D^e]\{\varepsilon^e_{tr}\}$	(4.17)
f				evaluate yield function based on trial stress	$f(\sigma, H\gamma, C\nabla^2\gamma)$	(5.8)
				IF $f \leq 0$		
$\{\sigma\}$				update stress	$\{\sigma\} = \{\sigma_{tr}\}$	
$\{\varepsilon^e\}$				update elastic strain	$\{\varepsilon^e\} = \{\varepsilon^e_{tr}\}$	
$[D^{alg}]$				update algorithmic consistent tangent	$[D^{alg}] = [D^e]$	
H				zero hardening parameter	$H = 0$	
				ELSE ($f > 0$)		
$\left\{\frac{\partial f}{\partial \sigma}\right\}, \left\{\frac{\partial^2 f}{\partial \sigma^2}\right\}$				Calculate derivatives of the yield function		
$\{\sigma_{n+1}\}$				update stress	$\{\sigma_n\} + [D^e]\{\{\Delta\varepsilon\} - \Delta\gamma\{f_{,\sigma}\}\}$	(5.64)
f				evaluate yield function based on updated stress	$f(\sigma, H\gamma, C\nabla^2\gamma)$	(5.8)
$\left\{\frac{\partial f}{\partial \sigma}\right\}, \left\{\frac{\partial^2 f}{\partial \sigma^2}\right\}$				Calculate updated derivatives of the yield function		
$[D^{alg}]$				calculate $[D^{alg}]$ consistent with the updated stress state	$[D^{alg}] = [[C^e] + d\gamma[\left\{\frac{\partial^2 f}{\partial \sigma^2}\right\}]]^{-1}$	(5.72)
H				set hardening parameter	$H = -0.1E$	

5.4.1 Additional boundary conditions

Due to the additional degrees of freedom required to use the Hermitian shape functions it is necessary to introduce additional boundary conditions relating to the plastic multiplier degrees of freedom. These are

$$\delta\gamma = 0 \quad \text{or} \quad (\nabla d\gamma)^T n_\gamma = 0 \tag{5.75}$$

where n_λ is the outward normal to the boundary of the plastic region. It is not always clear exactly where this plastic boundary is, however, in [59] it is stated that this can be achieved by setting the derivative of the plastic multiplier to zero in the direction normal to the model boundary. In 1D this corresponds to

$$\gamma_{,n} = 0, \tag{5.76}$$

and in 2D

$$\gamma_{,n} = 0 \quad \text{and} \quad \gamma_{,nm} = 0, \tag{5.77}$$

where n and m are normal and tangential directions to the model boundary. This may appear to be a minor point but has the potential to cause difficulties if these boundaries become not aligned with the background grid or move during a simulation.

5.5 Numerical examples

In this section the iGIMP method with gradient plasticity will be demonstrated on numerical examples in 1D and 2D.

5.5.1 Extension of a weakened bar

In the first example a 1D bar with a weakened section in the middle subjected to displacement at each end (as shown in Figure 5.7). The bar has a Young's modulus of

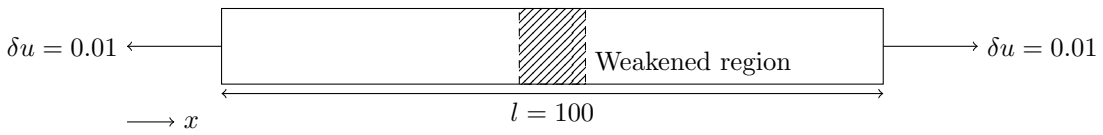

Figure 5.7: Bar with weakened central section subject to end displacements.

$E = 20000$, a yield strength of $\rho_y = 2$ (reduced by 10% in the weakened region) and has a softening(hardening) parameter of $H = -0.1E$. The bar has an initial length of 100, a weakened region of 10, and is displaced by 0.01 which leads to elasto-plastic behaviour in the weakened section. The problem was modelled over 20 loadsteps using 160 elements, each with two material points. Using a von Mises yield surface, the gradient yield function (5.8) becomes

$$f = \rho_y + H\gamma - c\Delta\gamma \tag{5.78}$$

where c is related to a length scale measurement ℓ through $c = -\ell^2 H$. Figure 5.8 shows the axial stress (taken at the end of the bar) plotted against the extension of the bar and shown along with the analytical solution for c=50000, equivalent to $\ell = 5$. The analytical gradient of the stress against extension graph during softening is derived to be $\frac{E}{L(\pi-1)}$ in [51]. It can be seen that the iGIMP method gives a value of -92.3281 which is within 1% of the analytical gradient.

In Figure 5.9, the plastic strain is plotted against position through the bar using the same parameters. It can be seen that the addition of the gradient terms has smoothed the plastic strain rather than having a sudden jump as would be the case for conventional plasticity. It can also be seen that as the number of background grid elements is increased, a peak value of plastic strain is converged towards. The width of the plastic strain zone can also be calculated analytically [51] as $2\pi\sqrt{\frac{-c}{H}}$. This is also plotted on Figure 5.9 and is shown to match closely with the values from the gradient GIMP method.

Figure 5.10 highlights a disadvantage of the gradient plasticity method chosen, showing that in the plastic region, stress oscillations occur. It can be seen that although the axial stress was as expected towards the ends of the bar, the stress towards the middle varies from each material point to the next rather than being fixed at the yield stress. It is possible that this is related to the basis functions used [52], and although it does not appear to affect the results of the plastic strain for this problem, it could have implications in more complicated analyses as will be explored in Chapter 6.

Figure 5.11 demonstrates the dependence of this axial stress on the length scale. The same problem was modelled using values of c of 12500, 50000 and 200000, it can be seen that the elastic behaviour is identical in each simulation however once the material yields and softening begins the behaviour is different for each length scale. Figure 5.12 shows

the distribution of plastic strain, and how it develops through the simulation, for each of these cases (a) c=12500, (b) c=50000 and (c) c=200000. It can be observed that with a larger length scale the zone of plastic strain is larger. Each of these cases is also compared against the analytical width, calculated in the same way as above, and is shown to agree well.

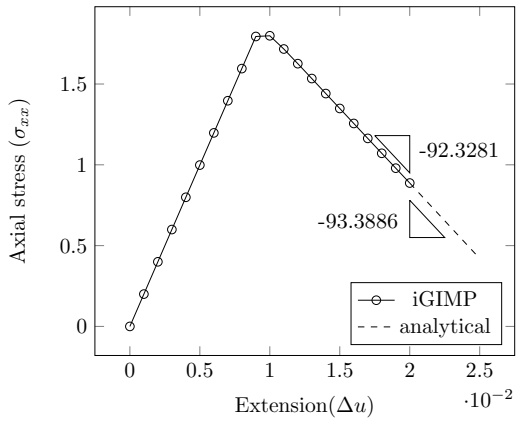

Figure 5.8: Plot of extension against axial stress comparing against analytical solution

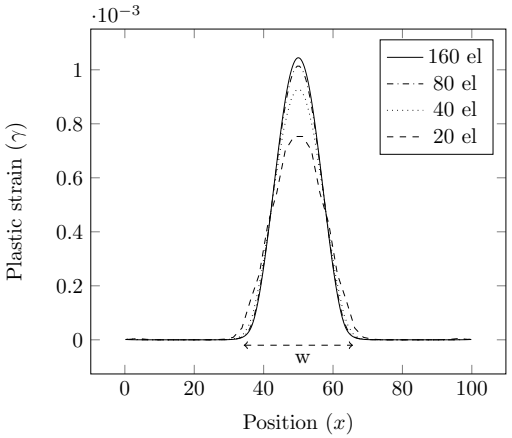

Figure 5.9: Position against plastic strain for different numbers of background grid elements

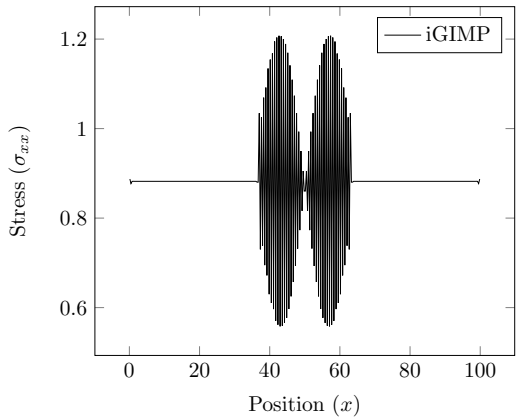

Figure 5.10: Stress through bar showing unphysical oscillations

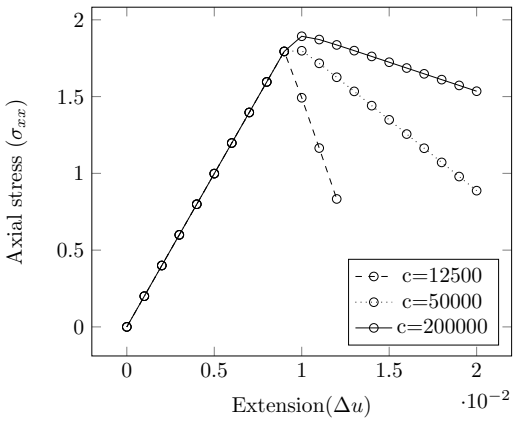

Figure 5.11: Extension against axial stress for varying values of c

5.5.2 Shear band in a 2D domain

The second example involves a 2D domain stretched by the right hand edge as analysed in [95]. The domain was fixed in the horizontal direction along the lefthand side, and restrained in the vertical direction at a single point at the centre of the lefthand side. A displacement of 0.002mm was prescribed to the righthand edge as shown in Figure

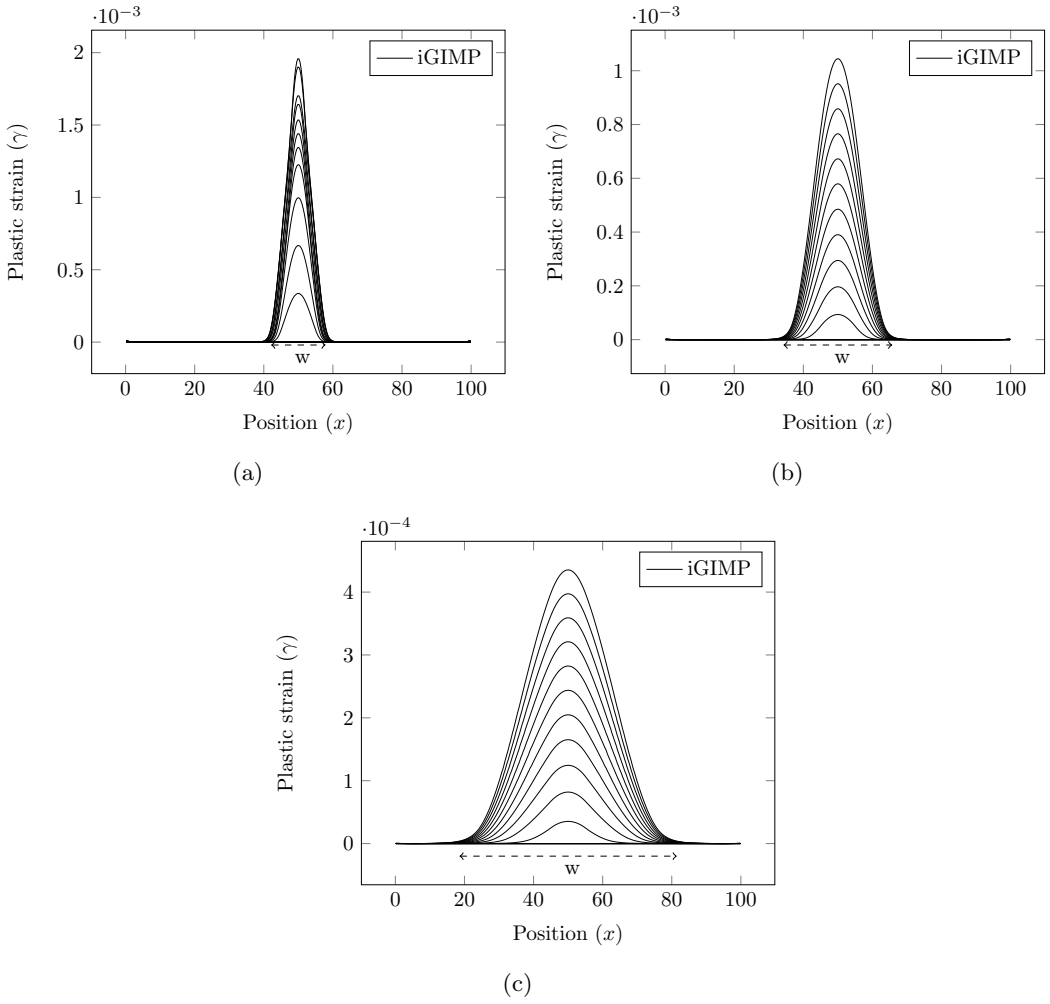

Figure 5.12: Plastic strain in an extended bar with varied length scale.

5.13. The Young's Modulus and Poisson's ratio were assigned as $E = 20000\text{N/mm}^2$ and $\nu = 0.25$. A small 1mm by 1mm section is weakened in the bottom left hand corner in order to initiate a shear band. The size of the domain was 10m by 10m and was modelled using 2 x 2 material points per element on a background grid one element larger than this on each side (although in reality displacements were so small any influence of these elements was negligible). Because of the small magnitude of the displacement it was possible to apply the boundary conditions (including the additional restraints of γ_x, γ_y and γ_{xy} needed because of the gradient formulation) directly to the background grid nodes.

It can be seen in Figure 5.15 that as the mesh is refined the width of the shear band becomes thinner, and this is dependent on the mesh. By introducing a length scale it can be seen in Figure 5.15 that the width of the shear band is now dependent on the

length scale rather than the size of the background grid elements. Figure 5.14 shows a force against displacement plot for the problem varying the number of elements with a length scale of zero and 400, it can be seen that without the length scale the response is dependent on the background grid element size. However, when using a length scale responses for all discretisations agree.

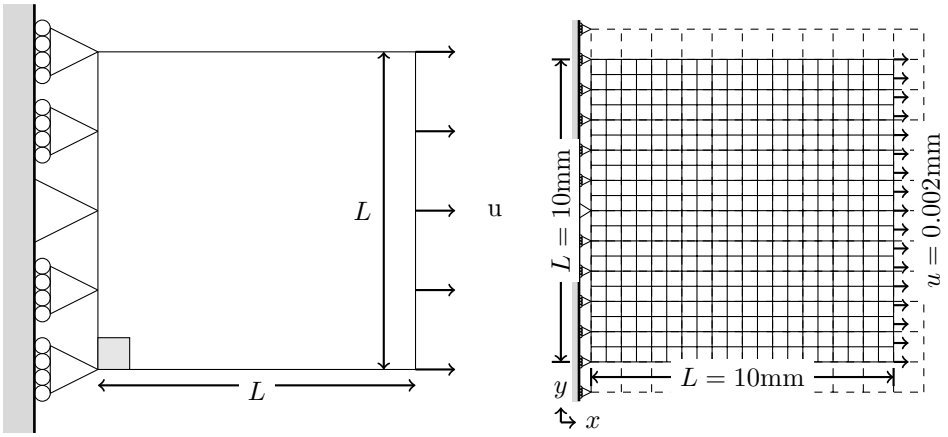

Figure 5.13: 2D square with weakened corner size 1mm x 1mm.

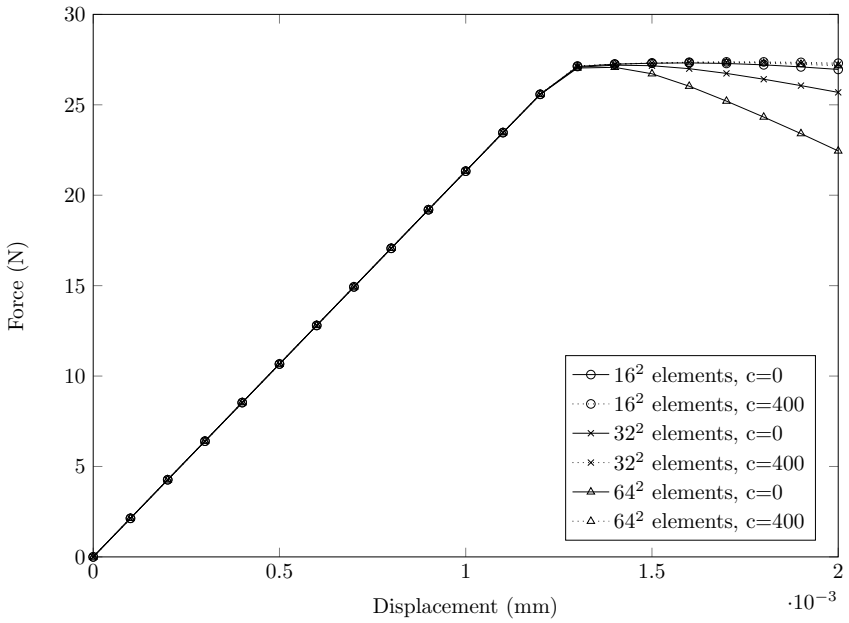

Figure 5.14: Force against displacement for square with shear band.

5.6 Observations

In this chapter an extension of the iGIMP method to gradient plasticity has been proposed. The plastic multiplier is now solved for as an additional degree of freedom at grid nodes along with its derivative and is mapped using Hermitian shape functions. The Laplacian of the plastic multiplier is introduced into the yield function along with a length scale which is shown in numerical examples to control the width of a region of plastic strain in 1D and a shear band in 2D. It should be noted that the formulation presented in this chapter is only suitable for small strains; although a large strain method would be desirable it is not included in this thesis. In the next chapter further examples will contrast the abilities of the different methods developed in the thesis.

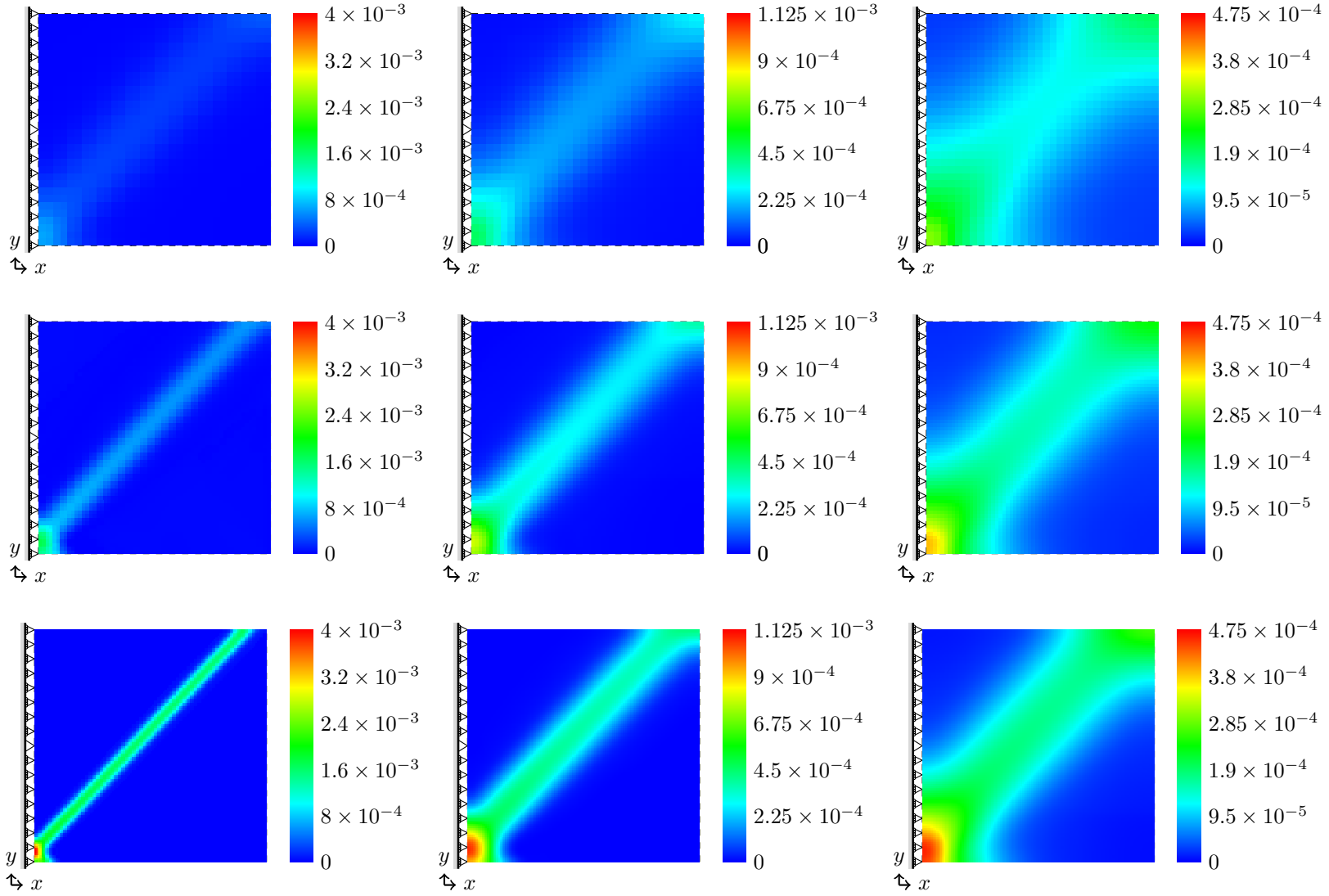

Figure 5.15: Shear bands in 2D square with length scales 0,100 and 400 (left to right) and 16^2,32^2 and 64^2 elements (top to bottom). Magnitude of plastic strain shown by colours with equal scales for each length scale.

Chapter 6

Numerical Examples

As shown in the previous chapter, for basic problems the combination of the gradient plasticity and iGIMP method can give results in agreement with analytical solutions and with the FEM for problems involving singularities and shear banding. This chapter will show examples to both further demonstrate the implicit GIMP method introduced in Chapters 3 and 4 and to highlight difficulties in utilising the gradient plasticity method introduced in Chapter 5. The focus will be on two different geometries modelled in 2D, the first being a square of material, and the second a steep slope with material properties and boundary conditions adjusted to introduce a singularity and to allow large deformations.

6.1 2D square

The first geometry to be considered has a height of 8 units and width of 8 units, for the following simulations the initial shape will be the same, however the material properties and boundary conditions will be specified in each example.

6.1.1 Elastic compaction under self weight

The large deformation capabilities of the implicit Generalised Interpolation Material Point (iGIMP) method will be demonstrated by showing the behaviour of the material deforming due to self-weight with increasing gravity. In this example, the domain is modelled using 8 x 8 elements, each populated by 4 x 4 material points, with the grid being sized 10 x 10 elements to allow for movement of material during the simulation. The material properties assigned are a Young's modulus of $E = 1 \times 10^5$ and Poisson's ratio of $\nu = 0.3$. Roller boundary conditions are applied on the lefthand edge which could represent symmetry

when modelling a block of width 16 units, and movement is restrained in a vertical direction along the bottom edge. A total weight of $w = 4 \times 10^5$ was applied to the block over 20 loadsteps. Figure 6.1 shows the initial and final position of the material, the shading corresponds to the vertical stress at each material point at the end of the simulation.

Figure 6.2 shows convergence within loadstep 16 for this problem. The near asymptotically quadratic convergence rate of the Newton-Raphson process indicates correct implementation of the method. Table 6.1 shows the values of the norm residual force ($\{f^R\}$) at the end of each Newton Raphson iteration for loadsteps 16-20.

Although no analytical solution to this problem exists it is still possible to verify the calculation by comparing it to an updated Lagrangian finite element analysis of the same problem. The maximum horizontal displacement at the bottom right hand corner of the material was calculated. For the FE analysis 1,000,000 linear finite elements were used and integrated with 2 x 2 gauss quadrature. By refining the background grid it can be seen that the displacements converge towards this reference solution. Values plotted in Figure 6.3 are normalised by this solution, it can be seen that for all cases the iGIMP results are in between those of linear and quadratic finite elements for the same mesh size. When calculating the displacement using the iGIMP method, the value used was the displacement of the bottom right material point plus half of any extension to its influence domain. The problem was simulated using varying numbers of material points per element and it can be seen that with an element size of 1 or smaller all discretisation came within 1% of the converged solution. This suggests that the number of elements in the background grid has more impact on the results than the number of material points per element.

6.1.2 Elasto-plastic compaction under self-weight

In this example, the same problem was modelled using 8 by 8 background grid elements, although this time each element was filled with 4x4 material points. A Young's modulus of $E = 1 \times 10^5$, Poisson's ratio of $\nu = 0.3$ and a total self weight applied of $w = 4 \times 10^5$

Table 6.1: Newton Raphson residuals showing near asymptotic quadratic convergence.

Step	16	17	18	19	20
Iteration 1	1.357×10^{-3}	1.246×10^{-3}	1.147×10^{-3}	1.094×10^{-3}	9.897×10^{-4}
Iteration 2	4.805×10^{-7}	4.202×10^{-7}	3.658×10^{-7}	3.478×10^{-7}	2.872×10^{-7}
Iteration 3	6.903×10^{-14}	5.399×10^{-14}	4.283×10^{-14}	1.839×10^{-12}	2.809×10^{-14}

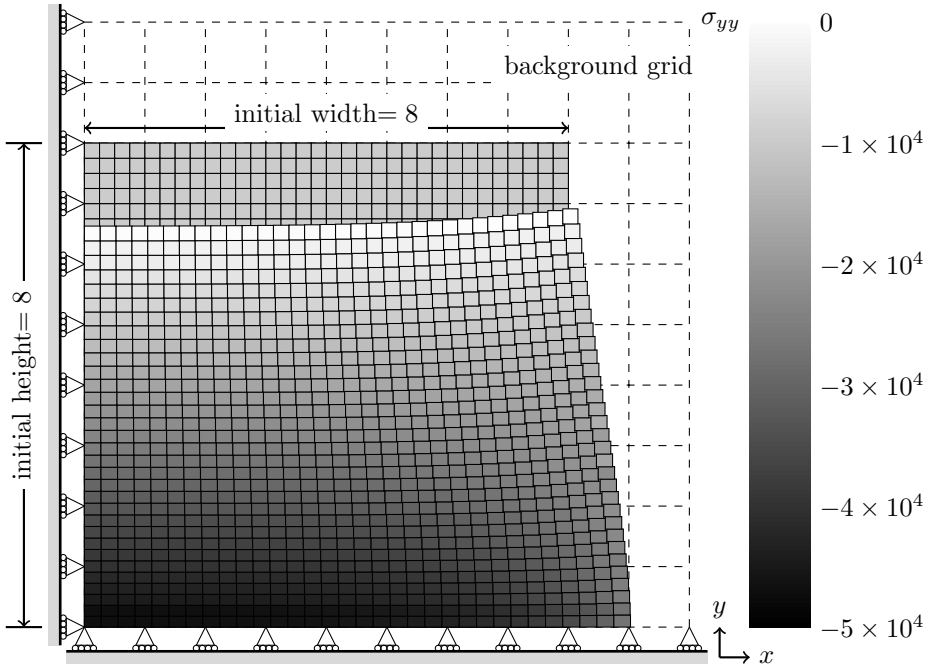

Figure 6.1: Compaction under self weight problem showing initial (grey) and final (shaded) material point positions and influence domains with vertical stress shown.

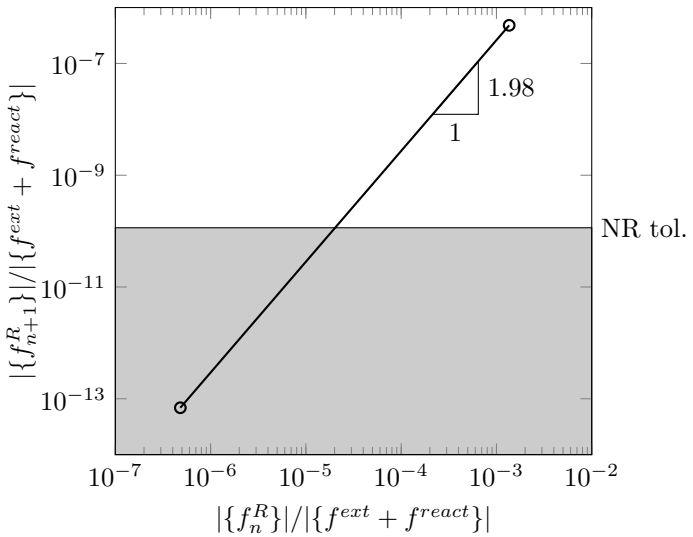

Figure 6.2: Norm residual force at the end of each iteration in loadstep 16, showing near asymptotic quadratic convergence.

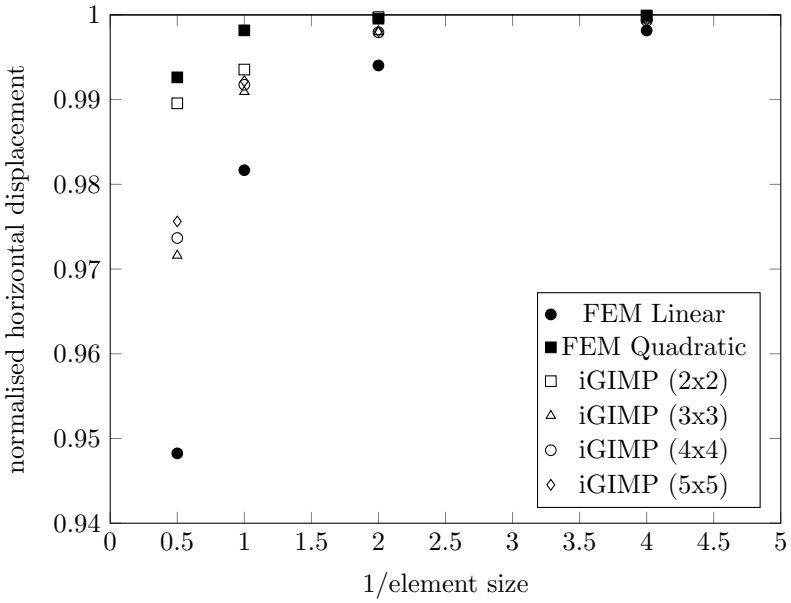

Figure 6.3: Physical convergence of displacement with changing mesh density for compaction of material under self weight.

were used as before. However this time a von Mises constitutive model with a deviatoric yield stress of $\rho_y = 1.2 \times 10^4$ was used. The yield function is defined as in (4.10). The initial and deformed shape of the domain can be seen in Figure 6.4, where it can be seen that significantly larger displacements have occurred than previously, where the material did not yield. The convergence is given in Table 6.2 for the final 5 steps of the simulation. It can be seen that, now the material behaviour is elasto-plastic, more iterations are needed for the NR algorithm to find the correct path, however, near asymptotic quadratic convergence is reached before running into machine precision at lower errors.

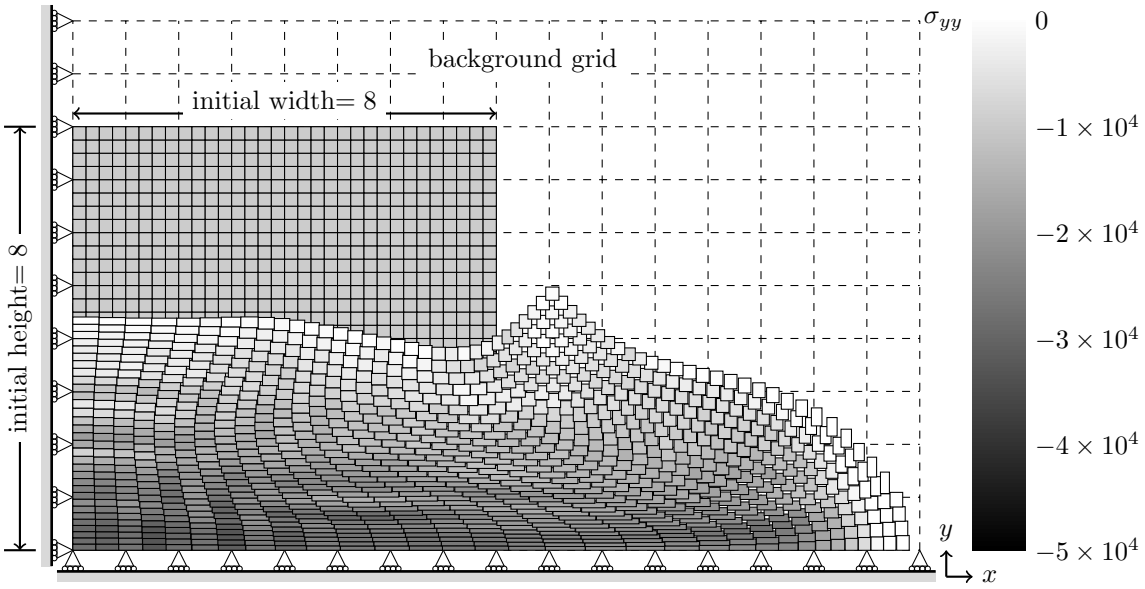

Figure 6.4: Compaction under self weight with a yield stress introducing elasto-plastic deformation.

6.1.3 Gradient elasto-plasticity analysis of rigid footing

In the previous two examples it can be seen that the iGIMP method performs well for problems involving compaction under self weight. In this example the material properties are altered to those in [142], that is a Young's Modulus of $E = 2.5 \times 10^8$, Poisson's ratio of $\nu = 0.25$ and a deviatoric yield stress of $\rho_y = 4 \times 10^3$. As the gradient method introduced in Chapter 5 will be used a softening modulus of $H = -16 \times 10^6$ and a length scale of $\ell = 0.4$ (equivalent to $c = 2.56 \times 10^6$) was also used. Boundary condition were applied to restrain displacements on the lefthand side and at the bottom as can be seen in Figure 6.5(a). A footing was simulated at the top right hand corner of the material which initiates

Table 6.2: Newton Raphson residuals for loadsteps of modelling compaction with elasto-plastic behaviour.

Step	16	17	18	19	20
Iteration 1	2.987×10^{-2}	2.787×10^{-2}	2.600×10^{-2}	2.467×10^{-2}	2.372×10^{-2}
Iteration 2	4.631×10^{-2}	4.703×10^{-2}	3.072×10^{-2}	2.504×10^{-2}	2.013×10^{-2}
Iteration 3	9.236×10^{-3}	2.483×10^{-3}	8.893×10^{-4}	6.861×10^{-4}	3.863×10^{-4}
Iteration 4	2.379×10^{-4}	1.530×10^{-5}	3.494×10^{-6}	1.633×10^{-6}	1.237×10^{-6}
Iteration 5	8.852×10^{-6}	1.562×10^{-10}	4.098×10^{-11}	2.642×10^{-12}	3.505×10^{-12}
Iteration 6	2.028×10^{-10}	8.386×10^{-16}			
Iteration 7	7.290×10^{-16}				

a shear band. The displacement of the footing was $u = 0.004$ and is applied directly to the background grid due to the small displacement. The simulation used 8 x 8 background grid elements, with 2 x 2 material points in each. In addition to the boundary conditions restraining the displacements, on the left and right hand edges of the material it was enforced that $\Lambda_{,x} = 0$ and $\Lambda_{,xy} = 0$ and on the top and bottom edges of the material it was enforced that $\Lambda_{,y} = 0$ and $\Lambda_{,xy} = 0$.

It can be seen that for these parameters the Newton Raphson loop converges with the expected rate of convergence as shown in Table 6.3. The value of the gradient parameter is altered to have values of $c = 1.28 \times 10^6$ and $c = 5.12 \times 10^6$ and the results of the simulation using these values are shown in Figure 6.5, where the distribution of plastic strain can be seen. Although with this density of background mesh and alteration in the gradient parameter the width of the shear band does not change dramatically it can be seen by using the same scales for each case that the plastic strains are more concentrated for the higher values of c. The difference can also be seen in Figure 6.6 where the force displacement response, calculated as the total force over the footing and the displacement of the footing, is dependent on the length scale parameter.

When increasing the number of background grid elements and using the gradient plasticity method, one would expect the response to be independent of the background mesh however, as can be seen in Figure 6.8, this was found not to be the case. This is the first indication of problems when using the method as proposed in Chapter 5. It can be seen in Figure 6.7 that by increasing the number of elements the width of the shear band appears to remain the same, however, convergence deteriorates, indicating that the global Newton Raphson loop was not able to converge to the required tolerance.

This could be attributed to the stress oscillations that have been observed previously

Table 6.3: Newton Raphson residuals for loadsteps of modelling gradient elasto-plastic behaviour of displacement of a footing on a square domain.

Step	16	17	18	19	20
Iteration 1	5.140×10^{-3}	5.076×10^{-3}	5.150×10^{-3}	5.317×10^{-3}	6.282×10^{-3}
Iteration 2	5.438×10^{-4}	4.793×10^{-4}	2.405×10^{-4}	7.591×10^{-4}	3.104×10^{-3}
Iteration 3	3.418×10^{-7}	1.656×10^{-7}	8.789×10^{-8}	5.826×10^{-7}	1.142×10^{-5}
Iteration 4	1.470×10^{-13}	2.878×10^{-14}	9.488×10^{-15}	5.183×10^{-13}	1.943×10^{-10}
Iteration 5					4.893×10^{-16}

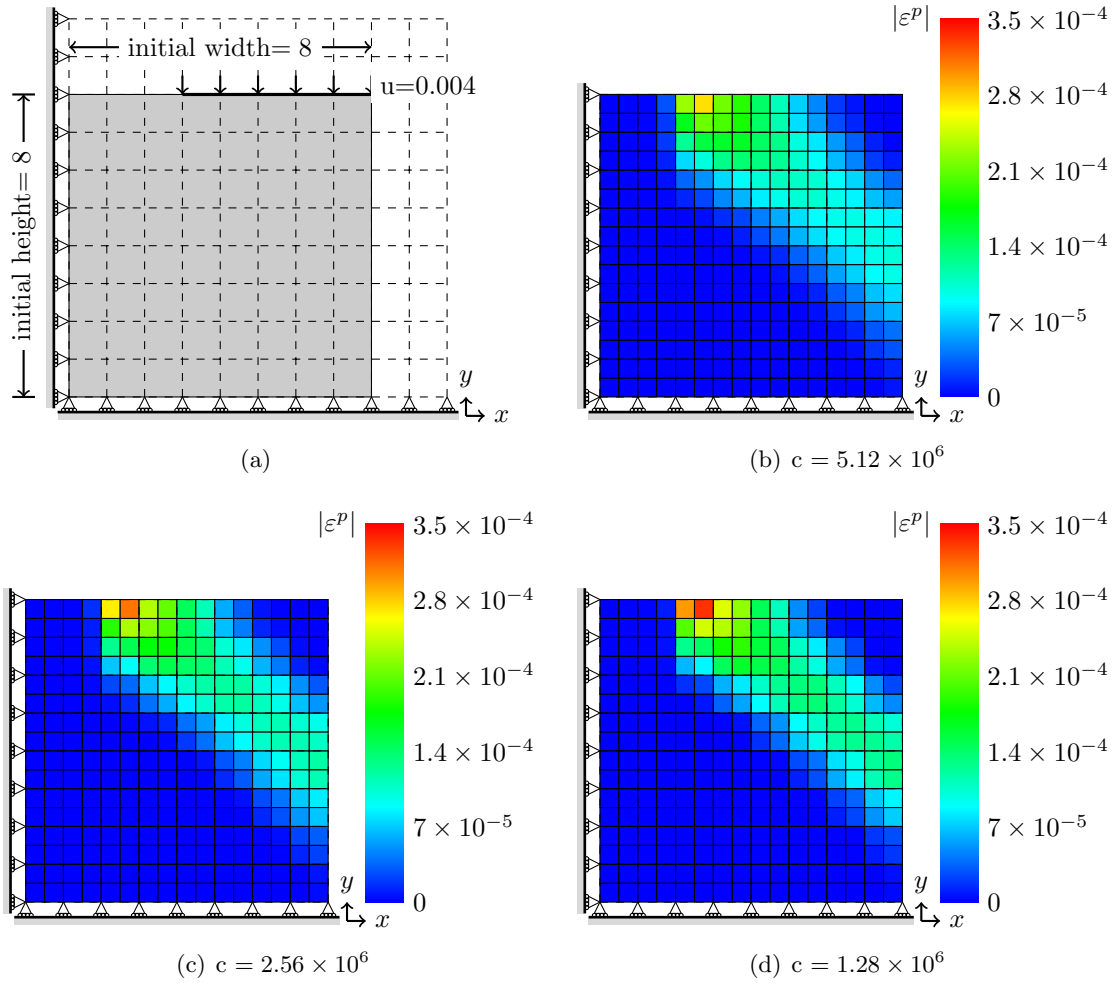

Figure 6.5: Geometry and plastic strain distribution for footing on square of material for different values of c.

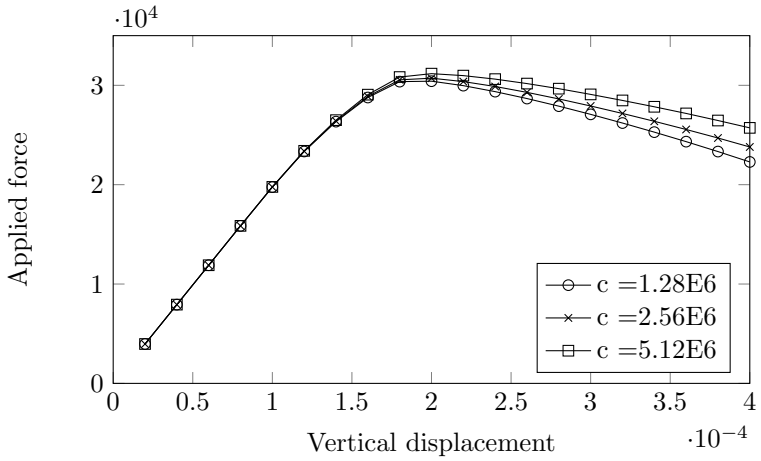

Figure 6.6: Force against displacement for different values of gradient parameter c.

in Chapter 5, similar behaviour was found in [143] working with the element-free Galerkin method. These spurious stresses will mean that that the material will enter the plastic regime erroneously. Although in the initial work [51] background elements with linear shape functions were used, in [52], a number of other elements were presented for use in gradient plasticity with the Finite Element Method (FEM). It was shown by De Borst and Pamin that the stress oscillations occur in both the 1D and 2D elements where the displacements are mapped using linear shape functions and the plastic multipliers with hermitian values and thus in further work quadratic interpolation of the displacements was used to avoid this. Because, in the MPM and iGIMP method used here, a linear background grid is utilised, the issue is still going to occur. It is not desirable to use quadratic FEM shape functions with the MPM or GIMP method in general as problems are introduced due to the negative values of the shape functions in certain positions [5]. Recently published work [95] includes the use of B splines instead of both the hermitian functions and linear/quadratic shape functions which could act as a possible solution, especially as similar approaches have been investigated to combat the grid crossing error in the standard MPM [132, 176], this is a major overhaul of the method and is beyond the scope of this thesis but could be an interesting topic of future research.

6.2 2D steep slope

The second problem that will be the looked at in this chapter will be a slope made by extending the previous geometry to include a steep slope. The geometry has been taken to be the same as [142], of height 10, top width 10 and a slope with gradient 7/20 as shown in Figure 6.9. To begin with the problem of a footing causing a shear band will be revisited, which is shown to encounter further problems with the gradient method combined with MPM. The large deformation elasto-plastic iGIMP method will then be examined, to demonstrate that the highlighted problems are a feature of the choice of gradient approach and not the MPM as a whole.

6.2.1 Slope with footing at top with gradient elasto-plasticity

In this example the material properties are the same as those in [142] and those used in the previous example of a shear band under a footing. These are a Young's Modulus of $E = 2.5 \times 10^8$, Poisson's ratio of $\nu = 0.25$, a deviatoric yield stress of $\rho_y = 4 \times 10^3$,

a softening modulus of $H = -16 \times 10^6$ and a length scale of $\ell = 0.4$ (equivalent to $c = 2.56 \times 10^6$).

Problems encountered

One of the advantages of the Material Point Method (MPM), or indeed mesh-free methods in general, is the ability to model geometry without having to match a mesh to the geometry. In this instance, a regular background mesh could be populated with material points to fill the geometry as required. The result of this is that a number of background grid elements become partially filled by material points. As shown in previous examples in Chapter 4, this is not a problem for the iGIMP method in general. However, upon running a problem with partially filled elements with the gradient method, it frequently causes the system of equations to become singular and prevents the analysis from completing.

This could be caused by integration errors, which in the standard MPM is often combatted by increasing the numbers of material points. However, increasing the number of material points used in the gradient elasto-plastic iGIMP method again causes the convergence to deteriorate. This can be shown to be the case even for the case of a single element, and is linked to the hermitian functions requiring optimal integration points to achieve required accuracy [52].

This is not the only problem that is encountered when attempting to model a slope using the proposed method. The fact that the slope face is no longer aligned with the background grid causes an additional problem due to the fact that it is necessary to impose $\Lambda_{,n}$ where n is the direction normal to the boundary and $\Lambda_{,xy}$ equal to zero at all of the problem boundaries. As discussed previously, the problem of applying boundary conditions in the MPM when they do not align with the grid has been addressed recently in [46] and [19] as this is also an issue in many other applications of the MPM.

Running an example

It is possible to make a crude approximation of the example which avoids the problem of partially filled elements and the sensitivity to quadrature by staggering the filled elements as seen in Figure 6.10. Certainly, adjusting the background grid to align with this boundary could be a possibility with a MPM however this is restricting the MPM and adjusting back towards FEM. The boundary conditions here are approximated by setting both $\Lambda_{,x}$

and $\Lambda_{,y}$ to zero at all the nodes along the zig-zag shaped boundary.

Despite the result showing the expected shape of shear band forming, which is only possible due to the addition of gradient terms (a conventional Finite element analysis results in a second band beginning at the other end of the footing). Degradation in convergence can be observed as was the case for the non-sloping example in Section 6.1.3, this can be seen in Figure 6.11.

6.2.2 Slope under self-weight

In this final example the material properties of the compaction under self weight of the square were used, Young's modulus of $E = 1 \times 10^5$, Poisson's ratio of $\nu = 0.3$, total self weight applied of $w = 6 \times 10^5$ over 20 loads steps and a deviatoric yield stress of $\rho_y = 1.2 \times 10^4$. Here the boundary conditions only restrict displacement perpendicular to the boundary at the left hand side and the bottom a shown in Figure 6.12. By reverting to the conventional large deformation plasticity iGIMP method introduced in Chapter 4 there is no requirement for additional boundary conditions on the free surfaces of the slope. The problem is modelled by filling the area occupied by the material with material points, in this case 6 x 6 material points are used for full elements and the same density for partially filled elements. Figure 6.12 shows the deformed shape of the slope after increasing the self weight to a point where the material has yielded. The colour represents the magnitude of plastic straining at each material point. It can be seen that as the slope deforms, the plastic zone spreads through the domain. Figure 6.13 shows the same simulation but using 2 x 2 (Subfigures (a) & (b)) and 4 x 4 (Subfigures (c) & (d)) material points. It can be seen that using 4 x 4 material points the results appear identical to those using 6 x 6. The simulation using 2 x 2 material points did not complete, Subfigure (b) shows the simulation after 18 load steps. It can be seen that in the top left of the domain, and in the bottom centre of the domain where the strain is highest that material points become stretched over the size of an element which causes stability issues in the code.

6.3 Observations

It has been shown in this chapter, both examples showing the capabilities of the iGIMP method to handle large deformation elasto-plasticity problems, as well as examples highlighting issues when combining it with with the Gradient plasticity method introduced

in Chapter 5. Despite showing initial promise as a candidate method for implementing a length scale dependent gradient plasticity method with the MPM, further investigation shows that for more general problems there are a number of obstacles which prevent this from being the case. The main problems that arose (and ideas of possible solutions) were:

- The use of linear background elements results in the gradient terms giving stress oscillations which in turn lead to poor convergence for the gradient method. The work using B splines in [95] with the FEM could be a possible avenue for overcoming this problem.

- Problems regarding position and number of material points when used with the hermitian functions. Again, replacing the Hermitian functions would eliminate this problem. Alternatively inspiration could be taken from other work in the MPM for example [69] where Gauss quadrature is used as an intermediate step to reduce errors resulting from sampling at material point positions.

- Imposition of boundary conditions which do not align with the background grid. Because the boundary conditions are required on the entire of the boundary of the material domain, in addition to not aligning with the grid, the boundary conditions will also need to evolve with the deformation. One approach that could make this possible has recently been developed in [19].

It is an interesting point that two of the major factors which caused the Gradient iGIMP proposed here not to be successful are also the causes of two of the main challenges in the MPM community as a whole, imposition of boundary conditions and continuity between background grid elements, clearly these are important areas of research if the method is to be successful in the future. In addition to this, it would be desirable in the future to have a gradient method which is compatible with the a large deformation framework. Without being able to handle large deformations correctly in a consistent framework such as outlined in Chapters 3 and 4 the MPM offers no additional benefit to the FEM but with higher computational expense. Despite these somewhat undesirable conclusions from the combination of a selected gradient plasticity method with the MPM, the benefits of the MPM can be seen clearly in the large deformation plasticity examples shown without the gradient influence.

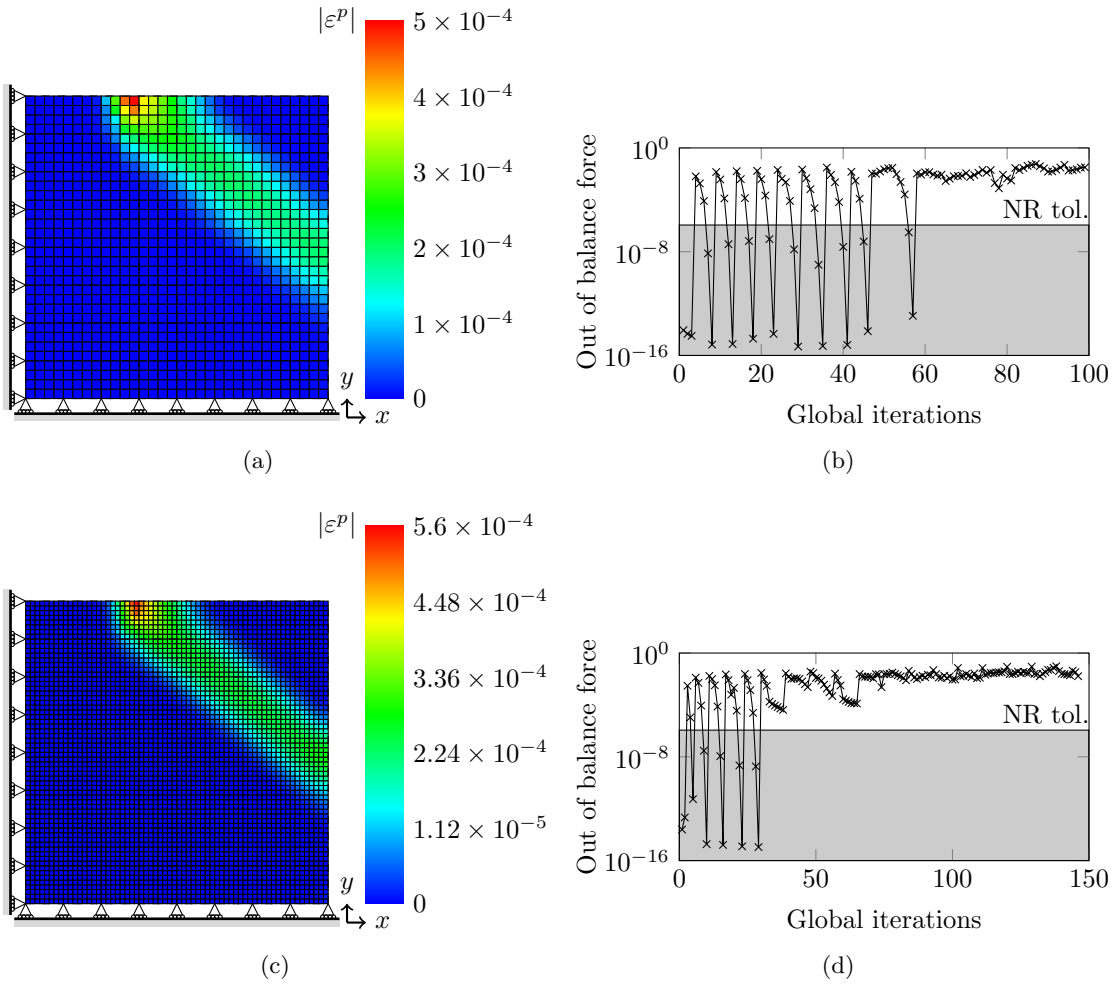

Figure 6.7: Plastic strain distribution and convergence plots for varied mesh density.

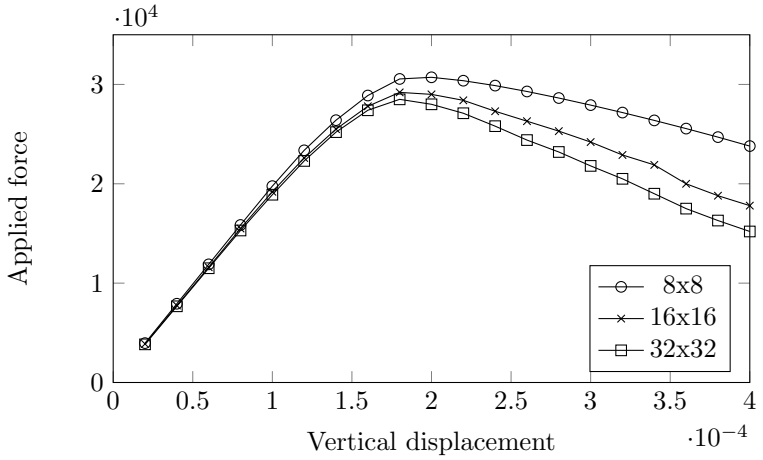

Figure 6.8: Force against displacement for varied mesh density.

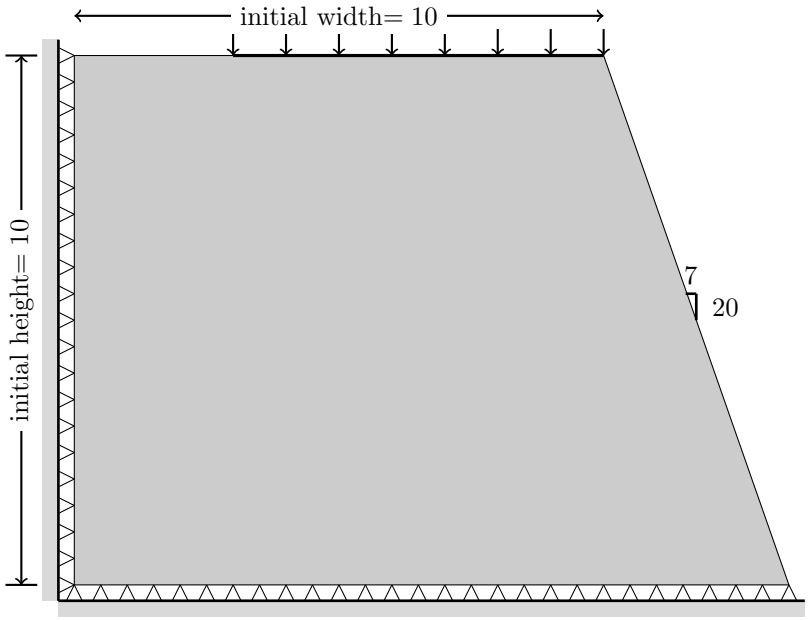

Figure 6.9: Geometry and boundary conditions of slope.

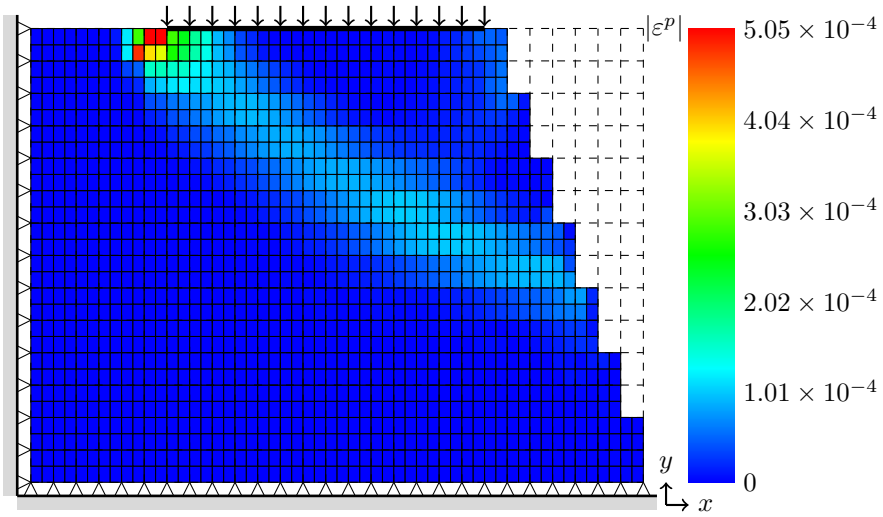

Figure 6.10: Material point model of slope showing magnitude of plastic strains.

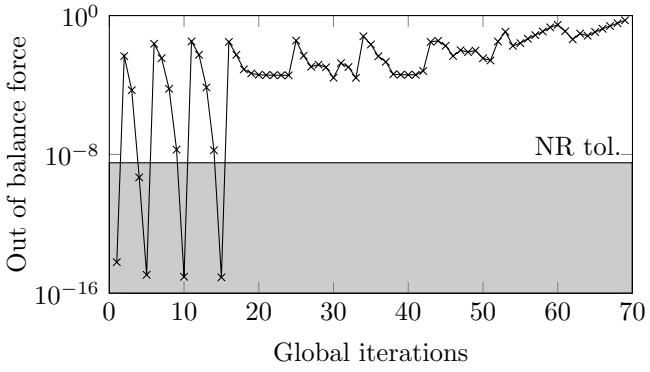

Figure 6.11: Convergence plot for analysis of slope.

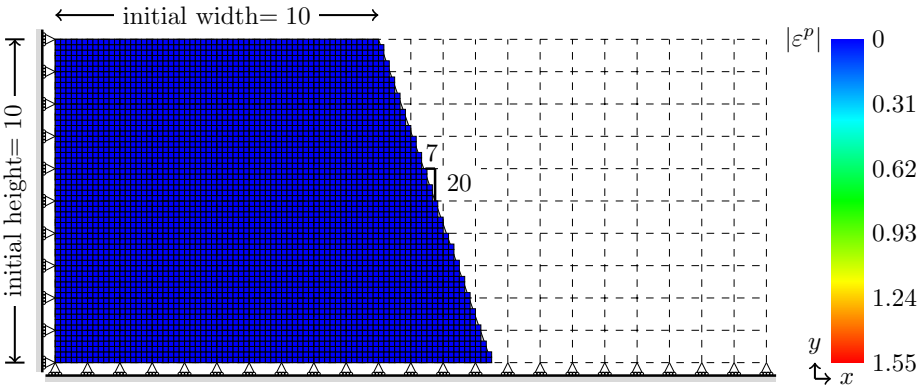

(a) Start of simulation, 6 x 6 material points

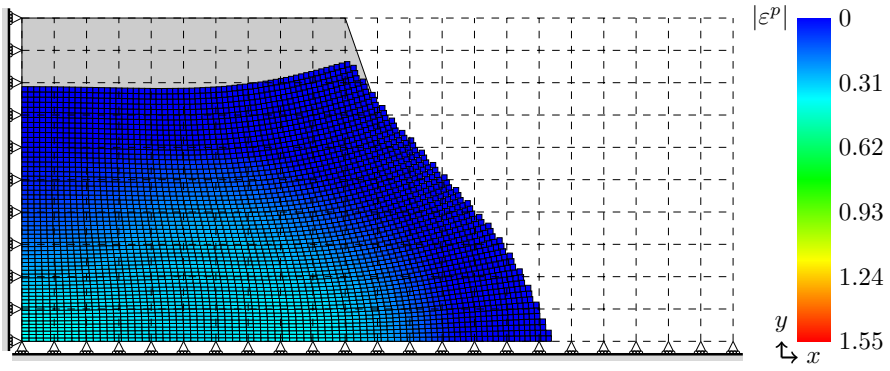

(b) Load step 13/20, 6 x 6 material points

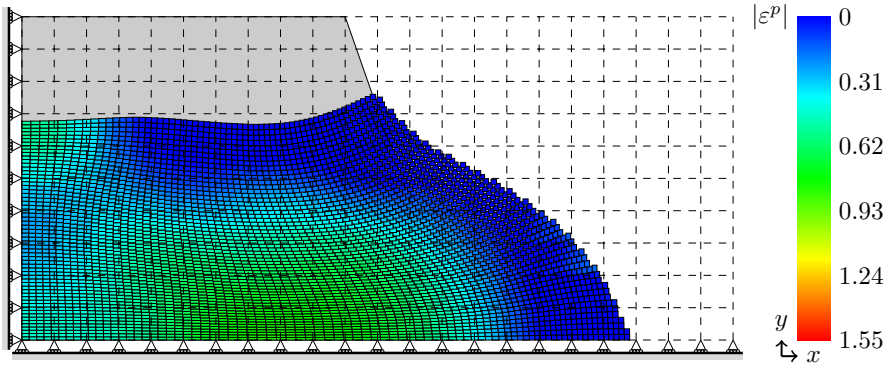

(c) Load step 16/20, 6 x 6 material points

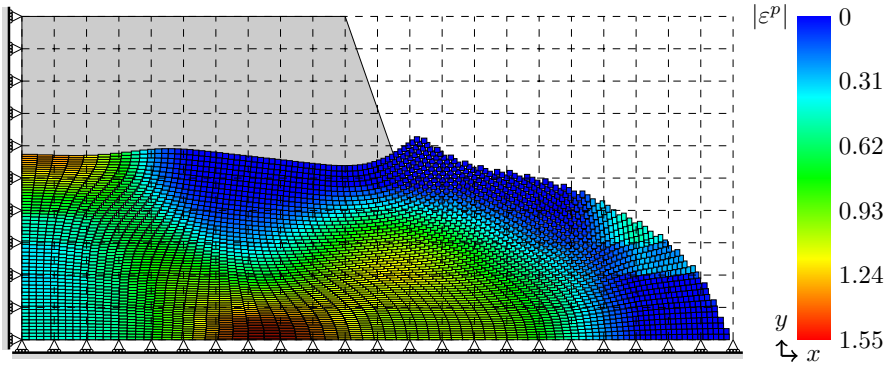

(d) End of simulation, 6 x 6 material points

Figure 6.12: Displaced geometry and material points showing magnitude of plastic strain using 6 x 6 material points per element.

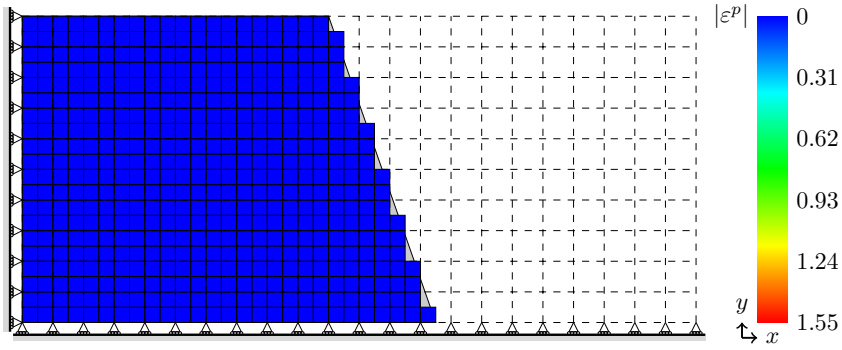

(a) Start of simulation, 2 x 2 material points

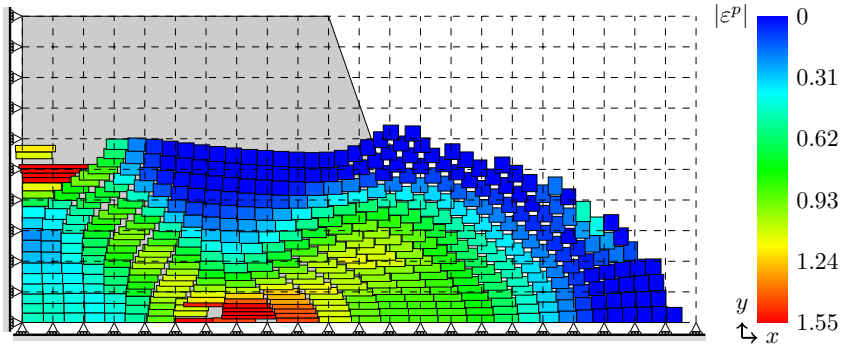

(b) Load step 18/20, 2 x 2 material points

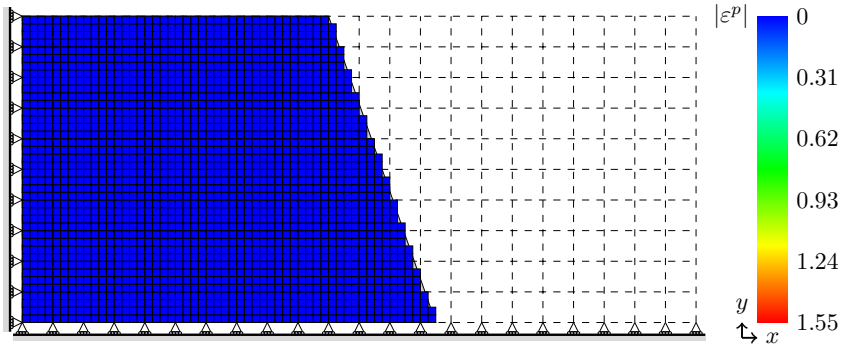

(c) Start of simulation, 4 x 4 material points

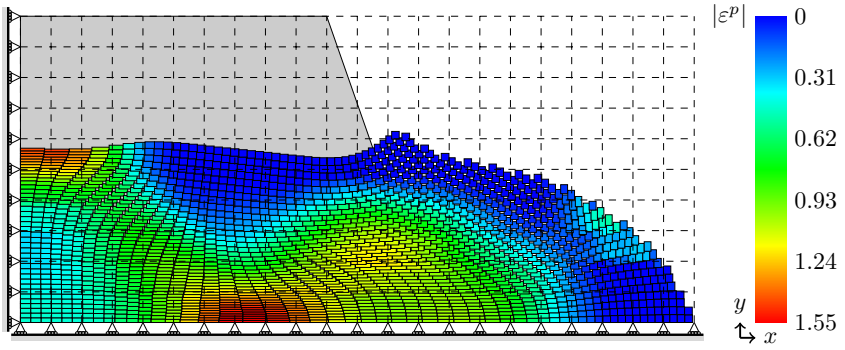

(d) End of simulation, 4 x 4 material points

Figure 6.13: Displaced geometry and material points showing magnitude of plastic strain using 2 x 2 and 4 x 4 material points per element.

Chapter 7

Conclusions

7.1 Summary

This thesis set out to develop the Material Point Method (MPM) as a method with potential for use in geotechnical problems. To model these problems, typically the ability to have a method able to handle both large deformations and material non-linearity is needed. A large proportion of previous research was found to be focused on an explicit implementation, particularly those developments using the Generalised Interpolation Material Point (GIMP) method for alleviating the grid crossing error present in the original MPM. Despite this, there are a number of advantages that can be gained by using an implicit approach including allowance of larger load steps, and improvement of error control. With these advantages in mind, an implicit GIMP method was implemented for the first time for large deformation elasto-plasticity. This method was then combined with a Gradient Plasticity approach with the aim of introducing a length scale parameter into the formulation to overcome mesh dependency in shear band problems.

Chapter 2 introduced the background of the MPM giving an overview of the method, a summary of the published literature discussing many of its current applications as well as highlighting current known issues such as the grid crossing instability which occurs when material points cross between background elements. The MPM was implemented for linear elasticity by modification of an existing Finite Element Method (FEM) code. Comparisons are frequently made in the literature between the FEM and MPM, however one must be cautious when doing this as the differences due to not updating the mesh have

ramifications when comparing to an analytical solution due to the fact that the moving of material points introduces an element of geometric non-linearity which is not accounted for. In the FEM, a small strain assumption means that calculations take place without the mesh being updated as it is assumed that deformations are small enough that this will not influence the results. In the MPM performing the same problem (over a number of load steps) would result in the material points moving to new positions with the deformation, however small, of the material and this will alter new values calculated based upon this. In the literature errors are frequently attributed to grid crossing and quadrature errors which may not always be the case.

Key novelties were introduced in Chapters 3 where the MPM was extended to the GIMP method in order to reduce the non-physical stress oscillations associated with grid crossing. The method was implemented with a geometrically nonlinear framework using logarithmic strains and Kirchhoff stresses. Again, this requires careful consideration, if basing an MPM implementation on the FEM, as the reference frame must be consistent with the method being used. In particular updating the deformation gradient and the calculation of the strain displacement matrix must be calculated differently to in the FEM as the concept of a previously converged or updated configuration only exists at the material points and not at the grid nodes where the equations are solved. The use of a standard Total Lagrangian or Updated Lagrangian formulation requires an initial or updated state at the grid nodes as the derivatives are based on this, therefore they must be mapped from the configuration at the start of the current step which is available in the MPM. A further novelty is the updating of the GIMP domains using the stretch tensor rather than the full deformation gradient. Although debate continues as to whether the GIMP method is the best approach to combat grid crossing, with this implementation it was possible to show correct convergence the method, something which has frequently been omitted in the literature. This is important in any method to be sure of it's accuracy and reliability before tackling problems without known solutions. Although the MPM, which has now existed for over 20 years, has gathered traction recently, the initial work developing the method seems to have given way to impressive looking simulations without much documented consideration of convergence or agreement with analytical solutions, instead favouring qualitative comparison to experimental results. Chapter 4 extended

the method to include elasto-plasticity, this is essential for geotechnical type problems and although only the von Mises yield surface was used for simplicity, the framework implemented allows a straightforward replacement with other constitutive models without modifying the rest of the code. Again this was compared to analytical solutions and convergence due to the use of a consistent tangent was shown.

It has been suggested many times that the MPM's similarities to the FEM should allow technologies which exist within the finite element community to be transferred easily to the MPM however there are some caveats which must be accounted for. Chapter 5 demonstrated this by introducing a gradient plasticity method to the MPM for the first time. The approach introduced a second differential equation to solve for the plastic multiplier which was mapped using hermitian shape functions to allow for C1 continuity and introducing a length scale parameter to remove mesh dependency for problems such as those involving shear banding. It was shown successfully to agree with FEM and analytical solutions for test cases.

Despite the combination of Gradient plasticity and the implicit Generalised Interpolation Material Point (iGIMP) method showing initial promise, further examples in Chapter 6 brought to light issues which show that changes from the FEM to MPM are not always trivial. Problems which in the FEM are solved by increasing the order of the background elements or changing the quadrature are not as easy to solve in MPM. The use of linear background elements introducing stress oscillations which in turn lead to poor convergence towards equilibrium for the gradient method, in FEM quadratic elements can be used but this is not as simple in MPM. Problems exist regarding position and number of material points when used with the hermitian functions, it is not possible to use reduced integration in the MPM as could be done in the FEM. The problem of imposition of boundary conditions which do not align with the background grid also caused issues. This is specifically a problem in the gradient plasticity method investigated as it is necessary to have boundary conditions on all edges of the problem domain for the derivatives of the plastic multiplier.

7.2 Future work

Based on the work undertaken during this thesis, there are a number of areas which present themselves as clear opportunities for future research and development:

- In all the examples in this thesis[1], and a large proportion of those in the published literature, problems have been chosen where prescribed boundary conditions are aligned with the background grid. The reason for this is that there is no established method for applying boundary conditions when the geometry does not align with the background grid. A situation which, to fully take advantage of the MPM as a mesh-free method is likely to arise and thus must be addressed. Although there has been some recent research on the topic such as suggestions of B-splines [19], implicit boundaries [45] and a moving mesh method [163] there is still work to be done to develop a method that can be relied on for all types of boundaries of arbitrary and possibly changing shape.

- In this thesis, all examples of elasto-plasticity have been restricted to use of the von Mises yield function. This was for simplicity as opposed to incompatibility, for geotechnical problems this is not a very good approximation to soil behaviour. An extension to the large deformation elasto-plastic iGIMP code to allow more complex behaviour would allow more realistic problems to be modelled. Another useful extension would be to include a water phase as has been done for example in [10] as many geotechnical problems which would benefit from use of the MPM also require a soil model which accounts for moisture.

- Although ultimately only partially successful, the conclusions relating to the presented gradient formulation in combination with the MPM will be of use to any future research in the area. As previously suggested in Chapter 7, the combination of recent contributions to the MPM [132] and to Gradient plasticity [95] both utilising B-splines could be combined to potentially alleviate some of the problems encountered. Research could also focus on a gradient method that is compatible with a large deformation framework as is ultimately required to be of use with the MPM in order to offer an advantage over the FEM. To do this it will also be necessary to deal with the boundary conditions in a more general manner as mentioned earlier.

[1] With the exception of the problem presented in Section 6.2.1 where it specifically highlights problems relating to boundary conditions not aligned with the mesh.

7.3 Final thoughts

It is hoped that the ideas presented in this thesis will be of use in some capacity to the progress of the MPM and GIMP method. Particular attention has been made to demonstrate convergence of the algorithms used in this implementation and comparisons to analytical solutions where possible which in some cases appear to have been omitted in the literature. In the future, work showing that the method behaves correctly and can be trusted is essential should the MPM become a useful tool for modelling real geotechnical problems.

Appendix A

Analytical solution to column under self weight with elasto-plasticity

The response of a column to the application of a body force due to increasing gravity is modelled. The column has an initial length (L_0) and is restrained at the bottom with $u(z = 0) = 0$. Displacement is only permitted in a vertical direction. A Young's modulus of E and a density of ρ_0 in compatible units are assigned to give a total force, once gravity (g) is applied, of w. This time a deviatoric yield stress of ρ_y is introduced. The von-Mises yield surface is defined as

$$f = \rho - \rho_y = 0 \tag{A.1}$$

as outlined in section 4.3. The material will yield when $\tau_{zz} = \rho_y$ which should occur at a position of $Z = l_0 - \frac{\rho_y}{\rho_o b_0}$ which can be obtained from rearranging the solution for the Cauchy stress in the vertical direction for the elastic case which can be determined from the initial vertical position within the column, Z, through

$$\sigma_{zz} = \rho_0 b(l_0 - Z), \tag{A.2}$$

where ρ_0 is the initial density of the material and b is the body force. Below this point, the material will experience elasto-plastic behaviour and despite zero deformation being

enforced in the out of plane directions, stresses τ_{xx} and τ_{yy} will be introduced. Because the boundary conditions are the same these two stresses will be equal, because of this from here on only variables in the x direction will be discussed. Using this it is possible to write the deviatoric stress as $\rho = |\tau_{xx} - \tau_{zz}|$. The Cauchy and Kirchhoff stresses (τ) are linked through $\sigma = \frac{\tau}{J}$ where $J = \det(F)$ which in this case is equal to F_{zz}. Due to the boundary conditions it is known that

$$[F] = \begin{bmatrix} 1 & 0 & 0 \\ 0 & 1 & 0 \\ 0 & 0 & F_{zz} \end{bmatrix}. \tag{A.3}$$

When there are only normal components, the logarithmic strain is defined as

$$\varepsilon^{(0)} = \frac{1}{2}\ln(F^2) = \ln(F) \tag{A.4}$$

The deformation gradient can be split into elastic and plastic components using multiplicative decomposition $F = F^e F^p$. Using this and A.3 we can get

$$F^e_{xx} F^p_{xx} = 1 \quad \text{and} \quad F^e_{zz} F^p_{zz} = J. \tag{A.5}$$

Using the fact that $\ln(F^e F^p) = \ln(F^e) + \ln(F^p)$ allows the strain to be split into elastic and plastic components

$$\varepsilon^{(0)} = \varepsilon^e + \varepsilon^p = \ln(F^e) + \ln(F^p) \tag{A.6}$$

and with $v = 0$ we can assume that the Kirchhoff stress is linked to the elastic logarithmic strain through

$$\tau = E\varepsilon^e. \tag{A.7}$$

When elasto-plastic behaviour has started, using the above relationships we can write

$$E\varepsilon^e_{xx} - E\varepsilon^e_{zz} = \rho_y = E\ln(F^e_{xx}) - E\ln(F^e_{zz}) \tag{A.8}$$

Rearranging this gives

$$\frac{\rho_y}{E} = \ln(F^e_{xx}) - \ln(F^e_{zz}) = \ln\left(\frac{F^e_{xx}}{F^e_{zz}}\right) \tag{A.9}$$

so it can be seen that

$$F^e_{xx} = F^e_{zz} e^{\frac{\rho_y}{E}}. \tag{A.10}$$

The derivative of the yield function with respect to the Kirchhoff stress ($\frac{df}{d\tau}$) can be shown through use of the chain rule to be

$$f_{,\tau} = f_{,\rho}\rho_{,J_2}\{J_{2,S}\}^T[S_{,\tau}] = \frac{3}{2\rho}\{S\} = \frac{3}{2\rho}\frac{1}{3}\begin{Bmatrix} \tau_{xx} - \tau_{zz} \\ \tau_{xx} - \tau_{zz} \\ 2\tau_{zz} - 2\tau_{xx} \end{Bmatrix} \tag{A.11}$$

Using $\rho = |\tau_{xx} - \tau_{zz}|$ and $\varepsilon^p = \dot{\gamma}\{f_{,\tau}\}$ we can arrive at the relationship

$$\frac{\varepsilon^p_{xx}}{\varepsilon^p_{zz}} = -\frac{1}{2} \quad \text{or} \quad \frac{\ln(F^p_{xx})}{\ln(F^p_{zz})} = -\frac{1}{2} \tag{A.12}$$

Rearranging this gives

$$\ln(F^p_{xx}\sqrt{F^p_{zz}}) = 0 \tag{A.13}$$

Leading to the relationship

$$F^p_{xx}\sqrt{F^p_{zz}} = 1 \tag{A.14}$$

Combining A.14 and A.5 it can be seen that

$$\sqrt{F^p_{zz}} = F^e_{xx}. \tag{A.15}$$

Substitution of this into A.10 and squaring both sides gives

$$F^p_{zz} = {F^e_{zz}}^2 e^{(\frac{2\rho}{E})} \tag{A.16}$$

Using this, we can express $F_{zz} = {F^e_{zz}}^3 e^{(\frac{2\rho}{E})}$ and, using the solution for Cauchy stress above, say that

$$\sigma_{zz} = \frac{1}{{F^e_{zz}}^3 e^{(\frac{2\rho}{E})}} E \ln(F^e_{zz}). \tag{A.17}$$

The elastic part of the deformation gradient can then be found using a Newton process to solve for F^e_{zz} in (A.17). Using the above relationships it is possible to calculate the remaining parts of the deformation gradient and find the out of plane stresses as

$$\sigma_{xx} = \frac{1}{F_{zz}} E \ln(F^e_{xx}). \tag{A.18}$$

References

[1] K. Abe, K. Soga, and S. Bandara, "Material point method for coupled hydromechanical problems," *Journal of Geotechnical and Geoenvironmental Engineering*, vol. 140, no. 3, p. 04013033, 2013.

[2] E. C. Aifantis, "On the microstructural origin of certain inelastic models," *Journal of Engineering Materials and technology*, vol. 106, no. 4, pp. 326–330, 1984.

[3] E. Alonso and A. Yerro, "Trends in large-deformation analysis of landslide mass movements with particular emphasis on the material point method," *Géotechnique*, vol. 66, no. 3, pp. 248–273, 2016.

[4] R. Ambati, X. Pan, H. Yuan, and X. Zhang, "Application of material point methods for cutting process simulations," *Computational Materials Science*, vol. 57, pp. 102–110, 2012.

[5] S. Andersen and L. Andersen, "Analysis of spatial interpolation in the material-point method," *Computers & Structures*, vol. 88, pp. 506 – 518, 2010.

[6] S. Andersen and L. Andersen, "Material-point-method analysis of collapsing slopes," in *Proceedings of the 1 st International Symposium on Computational Geomechanics (COMGEO I)*, 2009, pp. 817–828.

[7] S. Andersen and L. Andersen, "Modelling of landslides with the material-point method," *Computational Geosciences*, vol. 14, no. 1, pp. 137–147, 2010.

[8] H. Askes and E. C. Aifantis, "Gradient elasticity in statics and dynamics: an overview of formulations, length scale identification procedures, finite element implementations and new results," *International Journal of Solids and Structures*, vol. 48, no. 13, pp. 1962–1990, 2011.

[9] C. E. Augarde, "Generation of shape functions for straight beam elements," *Computers & Structures*, vol. 68, no. 6, pp. 555 – 560, 1998.

[10] S. Bandara, A. Ferrari, and L. Laloui, "Modelling landslides in unsaturated slopes subjected to rainfall infiltration using material point method," *International Journal for Numerical and Analytical Methods in Geomechanics*, vol. 40, no. 9, pp. 1358–1380, 2016, nag.2499.

[11] S. Bandara and K. Soga, "Coupling of soil deformation and pore fluid flow using material point method," *Computers and Geotechnics*, vol. 63, no. 1, pp. 199–214, 2015.

[12] S. G. Bardenhagen, J. A. Nairn, and H. Lu, "Simulation of dynamic fracture with the material point method using a mixed J-integral and cohesive law approach," *International Journal of Fracture*, vol. 170, no. 1, pp. 49–66, 2011.

[13] S. Bardenhagen, "Energy conservation error in the material point method for solid mechanics," *Journal of Computational Physics*, vol. 180, no. 1, pp. 383 – 403, 2002.

[14] S. Bardenhagen, J. Brackbill, and D. Sulsky, "The material-point method for granular materials," *Computer Methods in Applied Mechanics and Engineering*, vol. 187, no. 3, pp. 529–541, 2000.

[15] S. Bardenhagen and E. Kober, "The generalized interpolation material point method," *Computer Modeling in Engineering and Sciences*, vol. 5, no. 6, pp. 477–496, 2004.

[16] L. Beuth, Z. Wieckowski, and P. Vermeer, "Solution of quasi-static large-strain problems by the material point method," *International Journal for Numerical and Analytical Methods in Geomechanics*, vol. 35, no. 13, pp. 1451–1465, 2011.

[17] L. Beuth, T. Benz, P. A. Vermeer, and Z. Wieckowski, "Large deformation analysis using a quasi-static material point method," *Journal of Theoretical and Applied Mechanics*, vol. 38, no. 1-2, pp. 45–60, 2008.

[18] T. Bhandari, F. Hamad, C. Moormann, K. Sharma, and B. Westrich, "Numerical modelling of seismic slope failure using mpm," *Computers and Geotechnics*, vol. 75, pp. 126–134, 2016.

[19] Y. Bing, "B-spline based boundary method for the material point method," Master's thesis, Durham University, 2017.

[20] J. U. Brackbill, D. B. Kothe, and H. M. Ruppel, "FLIP: A low-dissipation, particle-in-cell method for fluid flow," *Computer Physics Communications*, vol. 48, no. 1, pp. 25–38, 1988.

[21] J. Brackbill and H. Ruppel, "FLIP: A method for adaptively zoned, particle-in-cell calculations of fluid flows in two dimensions," *Journal of Computational Physics*, vol. 65, no. 2, pp. 314 – 343, 1986.

[22] M. Bürg, L. J. Lim, and R. Brinkgreve, "Application of a second-order implicit material point method," *Procedia Engineering*, vol. 175, pp. 279 – 286, 2017, proceedings of the 1st International Conference on the Material Point Method (MPM 2017).

[23] J. Burghardt, R. Brannon, and J. Guilkey, "A nonlocal plasticity formulation for the material point method," *Computer Methods in Applied Mechanics and Engineering*, vol. 225, pp. 55 – 64, 2012.

[24] O. Buzzi, D. Pedroso, and A. Giacomini, "Caveats on the implementation of the generalized material point method," *Computer Modeling in Engineering and Sciences*, vol. 1, no. 1, pp. 1–21, 2008.

[25] M. Á. Caminero, F. J. Montáns, and K.-J. Bathe, "Modeling large strain anisotropic elasto-plasticity with logarithmic strain and stress measures," *Computers & Structures*, vol. 89, no. 11, pp. 826–843, 2011.

[26] A. Cauchy, "Memoire sur les vibrations d'un double systeme de molecules et de l'ether continu dans un corps cristallise," *Oeuvres completes*, vol. Tome II, 1st Serie, no. 1, pp. 338–350,, 1850.

[27] F. Ceccato, L. Beuth, and P. Simonini, "Analysis of piezocone penetration under different drainage conditions with the two-phase material point method," *Journal of Geotechnical and Geoenvironmental Engineering*, vol. 142, no. 12, p. 04016066, 2016.

[28] F. Ceccato, L. Beuth, P. A. Vermeer, and P. Simonini, "Two-phase material point method applied to the study of cone penetration," *Computers and Geotechnics*, vol. 80, pp. 440–452, 2016.

[29] T. J. Charlton, W. M. Coombs, and C. E. Augarde, "Gradient elasto-plasticity with the generalised interpolation material point method," *Procedia Engineering*, vol. 175, pp. 110 – 115, 2017, proceedings of the 1st International Conference on the Material Point Method (MPM 2017).

[30] T. Charlton, W. Coombs, and C. Augarde, "iGIMP: An implicit generalised interpolation material point method for large deformations," *Computers & Structures*, vol. 190, pp. 108 – 125, 2017.

[31] H. Chen, I. Hagiwara, and A. Tieu, "A seamless coupling between molecular dynamics and material point method," *Japan journal of industrial and applied mathematics*, vol. 28, no. 1, pp. 55–67, 2011.

[32] Z. Chen, W. Hu, L. Shen, X. Xin, and R. Brannon, "An evaluation of the MPM for simulating dynamic failure with damage diffusion," *Engineering Fracture Mechanics*, vol. 69, no. 17, pp. 1873–1890, 2002.

[33] Z. Chen and R. Brannon, "An evaluation of the material point method," Sandia National Laboratories, Tech. Rep., 2002.

[34] Z. Chen, S. Jiang, Y. Gan, H. Liu, and T. D. Sewell, "A particle-based multiscale simulation procedure within the material point method framework," *Computational Particle Mechanics*, vol. 1, no. 2, pp. 147–158, 2014.

[35] Z.-P. Chen, X. Zhang, X.-M. Qiu, and Y. Liu, "A frictional contact algorithm for implicit material point method," *Computer Methods in Applied Mechanics and Engineering*, vol. 321, pp. 124–144, 2017.

[36] Z. Chen, X. Qiu, X. Zhang, and Y. Lian, "Improved coupling of finite element method with material point method based on a particle-to-surface contact algorithm," *Computer Methods in Applied Mechanics and Engineering*, vol. 293, pp. 1–19, 2015.

[37] W.-F. Chiang, M. DeLisi, T. Hummel, T. Prete, K. Tew, M. Hall, P. Wallstedt, and J. Guilkey, "GPU acceleration of the generalized interpolation material point method," in *Symposium on Application Accelerators in High Performance Computing, SAAHPC*, 2009.

[38] C. Coetzee, "Discrete and continuum modelling of soil cutting," *Computational Particle Mechanics*, vol. 1, no. 4, pp. 409–423, 2014.

[39] C. Coetzee, A. Basson, and P. Vermeer, "Discrete and continuum modelling of excavator bucket filling," *Journal of Terramechanics*, vol. 44, no. 2, pp. 177 – 186, 2007.

[40] C. Coetzee, P. Vermeer, and A. Basson, "The modelling of anchors using the material point method," *International Journal for Numerical and Analytical Methods in Geomechanics*, vol. 29, no. 9, pp. 879–895, 2005.

[41] A. Colom, "Solving hydro-mechanical problems with the material point method," in *Geotechnical Engineering: New Horizons*, 2011, pp. 318–323.

[42] W. Coombs, "Finite deformation of particulate geomaterials: frictional and anisotropic critical state elasto-plasticity," Ph.D. dissertation, Durham University, 2011.

[43] W. M. Coombs, T. J. Charlton, M. Cortis, and C. E. Augarde, "Overcoming volumetric locking in material point methods," *Computer Methods in Applied Mechanics and Engineering*, vol. 333, pp. 1 – 21, 2018.

[44] W. Coombs, R. Crouch, and C. Augarde, "70-line 3D finite deformation elastoplastic finite-element code," in *Numerical Methods in Geotechnical Engineering (NUMGE 2010)*. CRC Press, Jun. 2010, pp. 151–156.

[45] M. Cortis, W. Coombs, C. Augarde, M. Brown, A. Brennan, and S. Robinson, "Imposition of essential boundary conditions in the material point method," *International Journal for Numerical Methods in Engineering*, vol. 113, pp. 130–152, 2017.

[46] M. Cortis, W. M. Coombs, C. E. Augarde, S. Robinson, M. Brown, and A. Brennan, "Modelling seabed ploughing using the material point method," *Procedia Engineering*, vol. 175, pp. 1 – 7, 2017, proceedings of the 1st International Conference on the Material Point Method (MPM 2017).

[47] E. Cosserat and F. Cosserat, "Théorie des corps déformables," *Paris*, 1909.

[48] S. Cummins and J. Brackbill, "An implicit particle-in-cell method for granular materials," *Journal of Computational Physics*, vol. 180, no. 2, pp. 506 – 548, 2002.

[49] N. P. Daphalapurkar, H. Lu, D. Coker, and R. Komanduri, "Simulation of dynamic crack growth using the generalized interpolation material point (GIMP) method," *International Journal of Fracture*, vol. 143, no. 1, pp. 79–102, 2007.

[50] R. de Borst, L. Sluys, H.-B. Mühlhaus, and J. Pamin, "Fundamental issues in finite element analyses of localization of deformation," *Engineering computations*, vol. 10, no. 2, pp. 99–121, 1993.

[51] R. de Borst and H.-B. Mühlhaus, "Gradient-dependent plasticity: Formulation and algorithmic aspects," *International Journal for Numerical Methods in Engineering*, vol. 35, no. 3, pp. 521–539, 1992.

[52] R. de Borst and J. Pamin, "Some novel developments in finite element procedures for gradient-dependent plasticity," *International Journal for Numerical Methods in Engineering*, vol. 39, no. 14, pp. 2477–2505, 1996.

[53] E. A. de Souza Neto, D. Perić, and D. R. J. Owen, *Computational Methods For Plasticity: Theory and Applications*. John Wiley & Sons, Ltd, 2008.

[54] E. de Souza Neto, D. Perić, and D. Owen, "A computational model for ductile damage at finite strains." in *Computational Plasticity: Fundamentals and Applications Proceedings of the Third International Conference held in Barcelona*, D. Owen, E. Oate, and E. Hinton, Eds. Swansea: Pineridge Press., 1992, pp. 1425–1441.

[55] E. de Souza Neto, D. Perić, and D. Owen, *Computational methods for plasticity: Theory and applications*. John Wiley & Sons Ltd, 2008.

[56] T. R. Dhakal and D. Z. Zhang, "Material point methods applied to one-dimensional shock waves and dual domain material point method with sub-points," *Journal of Computational Physics*, vol. 325, pp. 301 – 313, 2016.

[57] Y. Dong, D. Wang, and M. F. Randolph, "A GPU parallel computing strategy for the material point method," *Computers and Geotechnics*, vol. 66, pp. 31–38, 2015.

[58] Y. Dong, D. Wang, and M. F. Randolph, "Runout of submarine landslide simulated with material point method," *Procedia Engineering*, vol. 175, pp. 357 – 364, 2017, proceedings of the 1st International Conference on the Material Point Method (MPM 2017).

[59] R. J. Dorgan, "A nonlocal model for coupled damage-plasticity incorporating gradients of internal state variables at multiscales," Ph.D. dissertation, 2006.

[60] A. C. Eringen, "On differential equations of nonlocal elasticity and solutions of screw dislocation and surface waves," *Journal of applied physics*, vol. 54, no. 9, pp. 4703–4710, 1983.

[61] A. Eringen, "Theories of nonlocal plasticity," *International Journal of Engineering Science*, vol. 21, no. 7, pp. 741 – 751, 1983.

[62] M. W. Evans, F. H. Harlow, and E. Bromberg, "The particle-in-cell method for hydrodynamic calculations," DTIC Document, Tech. Rep., 1957.

[63] F. Fatemizadeh and C. Moormann, "Investigation of the slope stability problem using the material point method," in *IOP Conference Series: Earth and Environmental Science*, vol. 26, no. 1. IOP Publishing, 2015, p. 012019.

[64] E. J. Fern and K. Soga, "Granular column collapse of wet sand," *Procedia Engineering*, vol. 175, pp. 14 – 20, 2017, proceedings of the 1st International Conference on the Material Point Method (MPM 2017).

[65] E. J. Fern and K. Soga, "The role of constitutive models in MPM simulations of granular column collapses," *Acta Geotechnica*, vol. 11, no. 3, pp. 659–678, 2016.

[66] N. Fleck and J. Hutchinson, "Strain gradient plasticity," *Advances in applied mechanics*, vol. 33, pp. 296–361, 1997.

[67] N. Fleck and J. Willis, "A mathematical basis for strain-gradient plasticity theory. part i: scalar plastic multiplier," *Journal of the Mechanics and Physics of Solids*, vol. 57, no. 1, pp. 161–177, 2009.

[68] N. Fleck and J. Willis, "A mathematical basis for strain-gradient plasticity theory. part ii: Tensorial plastic multiplier," *Journal of the Mechanics and Physics of Solids*, vol. 57, no. 7, pp. 1045–1057, 2009.

[69] Y. Gan, Z. Sun, Z. Chen, X. Zhang, and Y. Liu, "Enhancement of the material point method using b-spline basis functions," *International Journal for Numerical Methods in Engineering*, 2017.

[70] M. Gao, A. P. Tampubolon, C. Jiang, and E. Sifakis, "An adaptive generalized interpolation material point method for simulating elastoplastic materials," *ACM Transactions on Graphics*, vol. 36, no. 6, 2017.

[71] F. Gilabert, V. Cantavella, E. Sánchez, and G. Mallol, "Modelling fracture process in ceramic materials using the material point method," *EPL (Europhysics Letters)*, vol. 96, no. 2, p. 24002, 2011.

[72] A. Gilmanov and S. Acharya, "A hybrid immersed boundary and material point method for simulating 3d fluid–structure interaction problems," *International Journal for Numerical Methods in Fluids*, vol. 56, no. 12, pp. 2151–2177, 2008.

[73] M. Goodarzi and M. Rouainia, "Modelling slope failure using a quasi-static MPM with a non-local strain softening approach," *Procedia Engineering*, vol. 175, pp. 220 – 225, 2017, proceedings of the 1st International Conference on the Material Point Method (MPM 2017).

[74] C. Gritton, J. Guilkey, J. Hooper, D. Bedrov, R. M. Kirby, and M. Berzins, "Using the material point method to model chemical/mechanical coupling in the deformation of a silicon anode," *Modelling and Simulation in Materials Science and Engineering*, vol. 25, no. 4, p. 045005, 2017.

[75] X. Gu, C. Dong, T. Cheng, Y. Zhang, and Y. Bai, "The transient heat conduction MPM and GIMP applied to isotropic materials," *Engineering Analysis with Boundary Elements*, vol. 66, pp. 155–167, 2016.

[76] J. E. Guilkey and J. A. Weiss, "Implicit time integration for the material point method: Quantitative and algorithmic comparisons with the finite element method," *International Journal for Numerical Methods in Engineering*, vol. 57, no. 9, pp. 1323–1338, 2003.

[77] J. E. Guilkey, J. B. Hoying, and J. A. Weiss, "Computational modeling of multicellular constructs with the material point method," *Journal of Biomechanics*, vol. 39, no. 11, pp. 2074–2086, 2006.

[78] J. E. Guilkey, S. Bardenhagen, K. Roessig, J. Brackbill, W. Witzel, and J. Foster, "An improved contact algorithm for the material point method and application to stress propagation in granular material," *Computer Modeling in Engineering & Sciences*, vol. 2, no. 4, pp. 509–522, 2001.

[79] Y. Guo and J. Nairn, "Calculation of J-integral and stress intensity factors using the material point method," *Computer Modeling in Engineering & Sciences*, vol. 6, no. 3, pp. 295–308, 2004.

[80] Y. Guo and J. Nairn, "Three-dimensional dynamic fracture analysis using the material point method," *Computer Modeling in Engineering and Sciences*, vol. 16, no. 3, pp. 141–155, 2006.

[81] F. Hamad, "Formulation of the axisymmetric CPDI with application to pile driving in sand," *Computers and Geotechnics*, vol. 74, pp. 141–150, 2016.

[82] F. Hamad, D. Stolle, and C. Moormann, "Material point modelling of releasing geocontainers from a barge," *Geotextiles and Geomembranes*, vol. 44, no. 3, pp. 308–318, 2016.

[83] F. Hamad, D. Stolle, and P. Vermeer, "Modelling of membranes in the material point method with applications," *International Journal for Numerical and Analytical Methods in Geomechanics*, vol. 39, no. 8, pp. 833–853, 2015.

[84] C. C. Hammerquist and J. A. Nairn, "A new method for material point method particle updates that reduces noise and enhances stability," *Computer Methods in Applied Mechanics and Engineering*, vol. 318, pp. 724–738, 2017.

[85] Y. Higo, F. Oka, S. Kimoto, Y. Morinaka, Y. Goto, and Z. Chen, "A coupled MPM-FDM analysis method for multi-phase elasto-plastic soils," *Soils and Foundations*, vol. 50, no. 4, pp. 515–532, 2010.

[86] M. A. Homel, R. M. Brannon, and J. Guilkey, "Controlling the onset of numerical fracture in parallelized implementations of the material point method (MPM) with convective particle domain interpolation (cpdi) domain scaling," *International Journal for Numerical Methods in Engineering*, vol. 107, no. 1, pp. 31–48, 2016, nme.5151.

[87] W. Hu and Z. Chen, "A multi-mesh MPM for simulating the meshing process of spur gears," *Computers & structures*, vol. 81, no. 20, pp. 1991–2002, 2003.

[88] W. Hu and Z. Chen, "Model-based simulation of the synergistic effects of blast and fragmentation on a concrete wall using the MPM," *International Journal of Impact Engineering*, vol. 32, no. 12, pp. 2066–2096, 2006.

[89] P. Huang, X. Zhang, S. Ma, and X. Huang, "Contact algorithms for the material point method in impact and penetration simulation," *International journal for numerical methods in engineering*, vol. 85, no. 4, pp. 498–517, 2011.

[90] I. Ionescu, J. E. Guilkey, M. Berzins, J. A. Weiss, and R. M. Kirby, "Simulation of soft tissue failure using the material point method," *Journal of Biomechanical Engineering*, vol. 128, no. 6, pp. 917–924, 2006.

[91] I. Jassim, D. Stolle, and P. Vermeer, "Two-phase dynamic analysis by material point method," *International Journal for Numerical and Analytical Methods in Geomechanics*, vol. 37, no. 15, pp. 2502–2522, 2013.

[92] S. Jiang, Z. Chen, T. D. Sewell, and Y. Gan, "Multiscale simulation of the responses of discrete nanostructures to extreme loading conditions based on the material point method," *Computer Methods in Applied Mechanics and Engineering*, vol. 297, pp. 219–238, 2015.

[93] S. Jiang, J. Tao, T. D. Sewell, and Z. Chen, "Hierarchical multiscale simulations of crystalline β-octahydro-1,3,5,7-tetranitro-1,3,5,7-tetrazocine (β-hmx): Generalized interpolation material point method simulations of brittle fracture using an elasto-damage model derived from molecular dynamics," *International Journal of Damage Mechanics*, vol. 26, no. 2, pp. 293–313, 2017.

[94] D.-N. Kim, F. Montáns, and K. Bathe, "Insight into a model for large strain anisotropic elasto-plasticity," *Computational Mechanics*, vol. 44, no. 5, pp. 651–668, 2009.

[95] I. Kolo and R. de Borst, "An isogeometric analysis approach to gradient-dependent plasticity," *International Journal for Numerical Methods in Engineering*, 2017.

[96] S. Kularathna and K. Soga, "Implicit formulation of material point method for analysis of incompressible materials," *Computer Methods in Applied Mechanics and Engineering*, vol. 313, pp. 673–686, 2017.

[97] E. Lee, "Elastic-plastic deformation at finite strains," *Journal of Applied Mechanics*, vol. 36, pp. 1–6, 1969.

[98] E. Lee and D. Lu, "Finite-strain elastic-plastic theory with application to plane-wave analysis," *Journal of Applied Physics*, vol. 38, pp. 19–27, 1967.

[99] F. Li, J. Pan, and C. Sinka, "Modelling adhesive contact between fine particles using material point method," *Mechanics of Materials*, vol. 43, no. 3, pp. 157–167, 2011.

[100] F. Li, J. Pan, and C. Sinka, "Modelling brittle impact failure of disc particles using material point method," *International Journal of Impact Engineering*, vol. 38, no. 7, pp. 653–660, 2011.

[101] J. Li, Y. Hamamoto, Y. Liu, and X. Zhang, "Sloshing impact simulation with material point method and its experimental validations," *Computers & Fluids*, vol. 103, no. 1, pp. 86 – 99, 2014.

[102] S. Li and W. K. Liu, *Meshfree particle methods*. Springer Science & Business Media, 2007.

[103] Y. Lian, P. Yang, X. Zhang, F. Zhang, Y. Liu, and P. Huang, "A mesh-grading material point method and its parallelization for problems with localized extreme deformation," *Computer Methods in Applied Mechanics and Engineering*, vol. 289, pp. 291–315, 2015.

[104] Y. Lian, X. Zhang, and Y. Liu, "Coupling of finite element method with material point method by local multi-mesh contact method," *Computer Methods in Applied Mechanics and Engineering*, vol. 200, no. 47, pp. 3482–3494, 2011.

[105] Y. Lian, X. Zhang, and Y. Liu, "An adaptive finite element material point method and its application in extreme deformation problems," *Computer Methods in Applied Mechanics and Engineering*, vol. 241, pp. 275–285, 2012.

[106] Y. Lian, X. Zhang, F. Zhang, and X. Cui, "Tied interface grid material point method for problems with localized extreme deformation," *International Journal of Impact Engineering*, pp. –, 2014.

[107] Y. Lian, X. Zhang, X. Zhou, S. Ma, and Y. Zhao, "Numerical simulation of explosively driven metal by material point method," *International Journal of Impact Engineering*, vol. 38, no. 4, pp. 238–246, 2011.

[108] C. Liu, Q. Sun, F. Jin, and G. G. Zhou, "A fully coupled hydro-mechanical material point method for saturated dense granular materials," *Powder Technology*, 2017.

[109] C. Liu, Q. Sun, and Y. Yang, "Multi-scale modelling of granular pile collapse by using material point method and discrete element method," *Procedia Engineering*, vol. 175, pp. 29 – 35, 2017, proceedings of the 1st International Conference on the Material Point Method (MPM 2017).

[110] G.-R. Liu, *Meshfree methods: moving beyond the finite element method.* Taylor & Francis, 2009.

[111] G.-R. Liu and Y.-T. Gu, *An introduction to meshfree methods and their programming.* Springer Science & Business Media, 2005.

[112] P. Liu, Y. Liu, X. Zhang, and Y. Guan, "Investigation on high-velocity impact of micron particles using material point method," *International Journal of Impact Engineering*, vol. 75, pp. 241–254, 2015.

[113] M. Llano and M. Farias, "Use of generalized material point method (gimp) to simulate shallow wedge penetration," 06 2014.

[114] C. Long, D. Zhang, C. Bronkhorst, and G. Gray III, "Representing ductile damage with the dual domain material point method," *Computer Methods in Applied Mechanics and Engineering*, vol. 300, pp. 611–627, 2016.

[115] E. Love and D. L. Sulsky, "An energy-consistent material-point method for dynamic finite deformation plasticity," *International Journal for Numerical Methods in Engineering*, vol. 65, no. 10, pp. 1608–1638, 2006.

[116] E. Love and D. Sulsky, "An unconditionally stable, energy-momentum consistent implementation of the material-point method," *Computer Methods in Applied Mechanics and Engineering*, vol. 195, no. 33, pp. 3903 – 3925, 2006.

[117] H. Lu, N. Daphalapurkar, B. Wang, S. Roy, and R. Komanduri, "Multiscale simulation from atomistic to continuum–coupling molecular dynamics (MD) with the material point method (MPM)," *Philosophical Magazine*, vol. 86, no. 20, pp. 2971–2994, 2006.

[118] L. B. Lucy, "A numerical approach to the testing of the fission hypothesis," *The Astronomical Journal*, vol. 82, pp. 1013–1024, 1977.

[119] J. Ma, D. Wang, and M. Randolph, "A new contact algorithm in the material point method for geotechnical simulations," *International Journal for Numerical and Analytical Methods in Geomechanics*, vol. 38, no. 11, pp. 1197–1210, 2014.

[120] S. Ma, X. Zhang, and X. Qiu, "Comparison study of MPM and SPH in modeling hypervelocity impact problems," *International Journal of Impact Engineering*, vol. 36, no. 2, pp. 272 – 282, 2009.

[121] X. Ma, P. T. Giguere, B. Jayaraman, and D. Z. Zhang, "Distribution coefficient algorithm for small mass nodes in material point method," *Journal of Computational Physics*, vol. 229, no. 20, pp. 7819 – 7833, 2010.

[122] Z. Ma, X. Zhang, and P. Huang, "An object-oriented MPM framework for simulation of large deformation and contact of numerous grains," 2010.

[123] P. Mackenzie-Helnwein, P. Arduino, W. Shin, J. A. Moore, and G. R. Miller, "Modeling strategies for multiphase drag interactions using the material point method," *International Journal for Numerical Methods in Engineering*, vol. 83, no. 3, pp. 295–322, 2010.

[124] C. M. Mast, P. Arduino, P. Mackenzie-Helnwein, and G. R. Miller, "Simulating granular column collapse using the material point method," *Acta Geotechnica*, vol. 10, no. 1, pp. 101–116, 2015.

[125] C. Mast, P. Mackenzie-Helnwein, P. Arduino, G. Miller, and W. Shin, "Mitigating kinematic locking in the material point method," *Journal of Computational Physics*, vol. 231, no. 16, pp. 5351 – 5373, 2012.

[126] C. Miehe, "Comparison of two algorithms for the computation of fourth-order isotropic tensor functions," *Computers & Structures*, vol. 66, pp. 37–43, 1998.

[127] R. D. Mindlin, "Micro-structure in linear elasticity," *Archive for Rational Mechanics and Analysis*, vol. 16, no. 1, pp. 51–78, 1964.

[128] R. Mindlin, "Influence of couple-stresses on stress concentrations," *Experimental Mechanics*, vol. 3, no. 1, pp. 1–7, 1963.

[129] R. Mindlin and N. Eshel, "On first strain-gradient theories in linear elasticity," *International Journal of Solids and Structures*, vol. 4, no. 1, pp. 109–124, 1968.

[130] T. K. Molstad, "Finite deformation analysis using the finite element method," Ph.D. dissertation, University of British Columbia, 1977.

[131] L. Moresi, F. Dufour, and H.-B. Mühlhaus, "A Lagrangian integration point finite element method for large deformation modeling of viscoelastic geomaterials," *Journal of Computational Physics*, vol. 184, no. 2, pp. 476 – 497, 2003.

[132] Y. G. Motlagh and W. M. Coombs, "An implicit high-order material point method," *Procedia Engineering*, vol. 175, pp. 8 – 13, 2017, proceedings of the 1st International Conference on the Material Point Method (MPM 2017).

[133] A. Nair and S. Roy, "Implicit time integration in the generalized interpolation material point method for finite deformation hyperelasticity," *Mechanics of Advanced Materials and Structures*, vol. 19, no. 6, pp. 465–473, 2012.

[134] J. Nairn, "Modeling imperfect interfaces in the material point method using multimaterial methods," *CMES: Computer Modeling in Engineering & Sciences*, vol. 92, no. 3, pp. 271–299, 2013.

[135] J. A. Nairn, "Material point method calculations with explicit cracks," *Computer Modeling In Engineering & Sciences*, vol. 4, no. 6, pp. 649–663, 2003.

[136] J. A. Nairn, "Material point method simulations of transverse fracture in wood with realistic morphologies," *Holzforschung*, vol. 61, no. 4, pp. 375–381, 2007.

[137] J. A. Nairn, "Numerical simulation of orthogonal cutting using the material point method," *Engineering Fracture Mechanics*, vol. 149, pp. 262–275, 2015.

[138] J. A. Nairn and J. E. Guilkey, "Axisymmetric form of the generalized interpolation material point method," *International journal for numerical methods in engineering*, 2014.

[139] G. D. Nguyen, "An enriched constitutive model for fracture propagation analysis using the material point method," *arXiv preprint arXiv:1311.3739*, 2013.

[140] V. P. Nguyen, C. T. Nguyen, T. Rabczuk, and S. Natarajan, "On a family of convected particle domain interpolations in the material point method," *Finite Elements in Analysis and Design*, vol. 126, pp. 50–64, 2017.

[141] C. Nilsson, "On nonlocal rate-independent plasticity," *International Journal of Plasticity*, vol. 14, no. 6, pp. 551 – 575, 1998.

[142] J. Pamin, "Computational modelling of localized deformations with regularized continuum models," *Mechanics and Control*, vol. 30, no. 1, 2011.

[143] J. Pamin, H. Askes, and R. de Borst, "Two gradient plasticity theories discretized with the element-free galerkin method," *Computer Methods in Applied Mechanics and Engineering*, vol. 192, no. 20, pp. 2377 – 2403, 2003.

[144] X. Pan, A. Xu, G. Zhang, and J. Zhu, "Generalized interpolation material point approach to high melting explosive with cavities under shock," *Journal of Physics D: Applied Physics*, vol. 41, no. 1, p. 015401, 2007.

[145] N. Phuong, A. van Tol, A. Elkadi, and A. Rohe, "Modelling of pile installation using the material point method (MPM)," *Numerical Methods in Geotechnical Engineering*, vol. 271, 2014.

[146] N. Phuong, A. van Tol, A. Elkadi, and A. Rohe, "Numerical investigation of pile installation effects in sand using material point method," *Computers and Geotechnics*, vol. 73, pp. 58–71, 2016.

[147] S. J. Raymond, B. Jones, and J. R. Williams, "A strategy to couple the material point method (MPM) and smoothed particle hydrodynamics (SPH) computational techniques," *Computational Particle Mechanics*, pp. 1–10, 2016.

[148] A. Rodríguez-Ferran, T. Bennett, H. Askes, and E. Tamayo-Mas, "A general framework for softening regularisation based on gradient elasticity," *International Journal of Solids and Structures*, vol. 48, no. 9, pp. 1382 – 1394, 2011.

[149] A. Rohe, K. Soga, H. Teunissen, and B. Z. Coelho, Eds., *Proceedings of the 1st International Conference on the Material Point Method (MPM 2017)*, ser. Procedia Engineering, vol. 175, 2017.

[150] C. Ru and E. Aifantis, "A simple approach to solve boundary-value problems in gradient elasticity," *Acta Mechanica*, vol. 101, no. 1-4, pp. 59–68, 1993.

[151] A. Sadeghirad, R. M. Brannon, and J. Burghardt, "A convected particle domain interpolation technique to extend applicability of the material point method for problems involving massive deformations," *International Journal for Numerical Methods in Engineering*, vol. 86, no. 12, pp. 1435–1456, 2011.

[152] A. Sadeghirad, R. M. Brannon, and J. Guilkey, "Second-order convected particle domain interpolation (CPDI2) with enrichment for weak discontinuities at material interfaces," *International Journal for Numerical Methods in Engineering*, vol. 95, no. 11, pp. 928–952, 2013.

[153] H. Schreyer, D. Sulsky, and S.-J. Zhou, "Modeling delamination as a strong discontinuity with the material point method," *Computer Methods in Applied Mechanics and Engineering*, vol. 191, no. 2324, pp. 2483 – 2507, 2002.

[154] L. Shen and Z. Chen, "A silent boundary scheme with the material point method for dynamic analyses," *Computer Modeling in Engineering and Sciences*, vol. 7, pp. 305–320, 2005.

[155] W. Shin, G. R. Miller, P. Arduino, and P. Mackenzie-Helnwein, "Dynamic meshing for material point method computations," *World Academy of Science, Engineering and Technology*, vol. 4, pp. 64–72, 2010.

[156] J. Simo, "Algorithms for static and dynamic multiplicative plasticity that preserve the classical return mapping schemes of the infinitesimal theory," *Computer Methods in Applied Mechanics and Engineering*, vol. 99, no. 1, pp. 61–112, 1992.

[157] J. Simo and R. Taylor, "Consistent tangent operators for rate-independent elastoplasticity," *Computer Methods in Applied Mechanics and Engineering*, vol. 48, pp. 101–118, 1985.

[158] S. Sinaie, V. P. Nguyen, C. T. Nguyen, and S. Bordas, "Programming the material point method in Julia," *Advances in Engineering Software*, vol. 105, pp. 17 – 29, 2017.

[159] W. Sołowski and S. Sloan, "Modelling of sand column collapse with material point method," in *Proceedings of the 3rd international symposium on computational geomechanics (ComGeo III)*, 2013, pp. 698–705.

[160] W. Sołowski and S. Sloan, "Evaluation of material point method for use in geotechnics," *International Journal for Numerical and Analytical Methods in Geomechanics*, vol. 39, no. 7, pp. 685–701, 2015.

[161] M. Steffen, P. C. Wallstedt, J. E. Guilkey, R. M. Kirby, and M. Berzins, "Examination and analysis of implementation choices within the material point method," *Computer Modeling In Engineering & Sciences*, vol. 31, no. 2, pp. 107–127, 2008.

[162] M. Steffen, R. M. Kirby, and M. Berzins, "Analysis and reduction of quadrature errors in the material point method," *International Journal for Numerical Methods in Engineering*, vol. 76, no. 6, pp. 922–948, 2008.

[163] M. Steffen, R. M. Kirby, and M. Berzins, "Decoupling and balancing of space and time errors in the material point method," *International Journal for Numerical Methods in Engineering*, vol. 82, no. 10, pp. 1207–1243, 2010.

[164] A. Stomakhin, C. Schroeder, L. Chai, J. Teran, and A. Selle, "A material point method for snow simulation," *ACM Trans. Graph.*, vol. 32, no. 4, pp. 102:1–102:10, Jul. 2013.

[165] A. Stomakhin, C. Schroeder, C. Jiang, L. Chai, J. Teran, and A. Selle, "Augmented MPM for phase-change and varied materials," *ACM Transactions on Graphics (TOG)*, vol. 33, no. 4, p. 138, 2014.

[166] D. Sulsky and A. Kaul, "Implicit dynamics in the material-point method," *Computer Methods in Applied Mechanics and Engineering*, vol. 193, pp. 1137 – 1170, 2004.

[167] D. Sulsky and L. Schreyer, "MPM simulation of dynamic material failure with a decohesion constitutive model," *European Journal of Mechanics-A/Solids*, vol. 23, no. 3, pp. 423–445, 2004.

[168] D. Sulsky, Z. Chen, and H. L. Schreyer, "A particle method for history-dependent materials," *Computer Methods in Applied Mechanics and Engineering*, vol. 118, no. 1, pp. 179–196, 1994.

[169] D. Sulsky, H. Schreyer, K. Peterson, R. Kwok, and M. Coon, "Using the material-point method to model sea ice dynamics," *Journal of Geophysical Research: Oceans*, vol. 112, pp. 1–18, 2007.

[170] D. Sulsky and H. L. Schreyer, "Axisymmetric form of the material point method with applications to upsetting and taylor impact problems," *Computer Methods in Applied Mechanics and Engineering*, vol. 139, pp. 409 – 429, 1996.

[171] D. Sulsky, S.-J. Zhou, and H. L. Schreyer, "Application of a particle-in-cell method to solid mechanics," *Computer Physics Communications*, vol. 87, no. 1, pp. 236–252, 1995.

[172] Z. Sun, H. Li, Y. Gan, H. Liu, Z. Huang, and L. He, "Material point method and smoothed particle hydrodynamics simulations of fluid flow problems: a comparative study."

[173] H. Tan and J. A. Nairn, "Hierarchical, adaptive, material point method for dynamic energy release rate calculations," *Computer Methods in Applied Mechanics and Engineering*, vol. 191, no. 19, pp. 2123–2137, 2002.

[174] J. Tao, Y. Zheng, Z. Chen, and H. Zhang, "Generalized interpolation material point method for coupled thermo-mechanical processes," *International Journal of Mechanics and Materials in Design*, vol. 12, no. 4, pp. 577–595, 2016.

[175] F. S. Tehrani, P. Nguyen, R. B. Brinkgreve, and A. F. van Tol, "Comparison of press-replace method and material point method for analysis of jacked piles," *Computers and Geotechnics*, vol. 78, pp. 38 – 53, 2016.

[176] R. Tielen, E. Wobbes, M. Mller, and L. Beuth, "A high order material point method," *Procedia Engineering*, vol. 175, pp. 265 – 272, 2017, proceedings of the 1st International Conference on the Material Point Method (MPM 2017).

[177] S. P. Timoshenko and S. Woinowsky-Krieger, *Theory of plates and shells*. McGraw-hill, 1959.

[178] R. A. Toupin, "Elastic materials with couple-stresses," *Archive for Rational Mechanics and Analysis*, vol. 11, no. 1, pp. 385–414, 1962.

[179] R. A. Toupin, "Theories of elasticity with couple-stress," *Archive for Rational Mechanics and Analysis*, vol. 17, no. 2, pp. 85–112, 1964.

[180] L. Tran, J. Kim, and M. Berzins, "Solving time-dependent PDEs using the material point method, a case study from gas dynamics," *International journal for numerical methods in fluids*, vol. 62, no. 7, pp. 709–732, 2010.

[181] P. C. Wallstedt and J. E. Guilkey, "A weighted least squares particle-in-cell method for solid mechanics," *International Journal for Numerical Methods in Engineering*, vol. 85, no. 13, pp. 1687–1704, 2011.

[182] P. Wallstedt and J. Guilkey, "Improved velocity projection for the material point method," *CMES: Computer Modeling in Engineering & Sciences*, vol. 19, no. 3, pp. 223–232, 2007.

[183] P. Wallstedt and J. Guilkey, "An evaluation of explicit time integration schemes for use with the generalized interpolation material point method," *Journal of Computational Physics*, vol. 227, no. 22, pp. 9628–9642, 2008.

[184] B. Wang, M. Hicks, and P. Vardon, "Slope failure analysis using the random material point method," *Geotechnique Letters*, vol. 6, pp. 113–118, 2016.

[185] B. Wang, P. Vardon, and M. Hicks, "Investigation of retrogressive and progressive slope failure mechanisms using the material point method," *Computers and Geotechnics*, vol. 78, pp. 88–98, 2016.

[186] B. Wang, P. J. Vardon, M. A. Hicks, and Z. Chen, "Development of an implicit material point method for geotechnical applications," *Computers and Geotechnics*, vol. 71, pp. 159–167, 2016.

[187] L. Wang, W. M. Coombs, C. E. Augarde, M. Brown, J. Knappett, A. Brennan, D. Richards, and A. Blake, "Modelling screwpile installation using the MPM," *Procedia Engineering*, vol. 175, pp. 124 – 132, 2017, proceedings of the 1st International Conference on the Material Point Method (MPM 2017).

[188] Y. Wang, H. Beom, M. Sun, and S. Lin, "Numerical simulation of explosive welding using the material point method," *International Journal of Impact Engineering*, vol. 38, no. 1, pp. 51 – 60, 2011.

[189] Z. Wieckowski, "The material point method in large strain engineering problems," *Computer Methods in Applied Mechanics and Engineering*, vol. 193, pp. 4417 – 4438, 2004.

[190] S. I. Woo and R. Salgado, "Simulation of penetration of a foundation element in tresca soil using the generalized interpolation material point method (gimp)," *Computers and Geotechnics*, 2017.

[191] P. Xiao-Fei, X. Ai-Guo, Z. Guang-Cai, Z. Ping, Z. Jian-Shi, M. Shang, and Z. Xiong, "Three-dimensional multi-mesh material point method for solving collision problems," *Communications in Theoretical Physics*, vol. 49, no. 5, p. 1129, 2008.

[192] L. Xu, H. Schreyer, and D. Sulsky, "Blast-induced rock fracture near a tunnel," *International Journal for Numerical and Analytical Methods in Geomechanics*, vol. 39, no. 1, pp. 23–50, 2015.

[193] L. Xue, O. Borodin, and G. D. Smith, "Modeling of enhanced penetrant diffusion in nanoparticle-polymer composite membranes," *Journal of Membrane Science*, vol. 286, no. 1, pp. 293–300, 2006.

[194] L. Xue, O. Borodin, G. D. Smith, and J. Nairn, "Micromechanics simulations of the viscoelastic properties of highly filled composites by the material point method (MPM)," *Modelling and Simulation in Materials Science and Engineering*, vol. 14, no. 4, p. 703, 2006.

[195] A. Yerro, E. Alonso, and N. Pinyol, "Run-out of landslides in brittle soils," *Computers and Geotechnics*, vol. 80, pp. 427 – 439, 2016.

[196] A. Yerro, E. Alonso, and N. M. Pinyol, "The material point method for unsaturated soils," *Géotechnique*, vol. 65, no. 3, pp. 201–217, 2015.

[197] A. R. York, D. Sulsky, and H. L. Schreyer, "The material point method for simulation of thin membranes," *International Journal for Numerical Methods in Engineering*, vol. 44, no. 10, pp. 1429–1456, 1999.

[198] A. R. York, D. Sulsky, and H. L. Schreyer, "Fluidmembrane interaction based on the material point method," *International Journal for Numerical Methods in Engineering*, vol. 48, no. 6, pp. 901–924, 2000.

[199] Y. Yue, B. Smith, C. Batty, C. Zheng, and E. Grinspun, "Continuum foam: A material point method for shear-dependent flows," *ACM Trans. Graph.*, vol. 34, no. 5, pp. 160:1–160:20, Nov. 2015.

[200] F. Zabala and E. Alonso, "Progressive failure of Aznalcóllar dam using the material point method," *Géotechnique*, vol. 61, no. 9, pp. 795–808, 2011.

[201] D. Z. Zhang, X. Ma, and P. T. Giguere, "Material point method enhanced by modified gradient of shape function," *Journal of Computational Physics*, vol. 230, no. 16, pp. 6379 – 6398, 2011.

[202] D. Z. Zhang, Q. Zou, W. B. Vander Heyden, and X. Ma, "Material point method applied to multiphase flows," *Journal of Computational Physics*, vol. 227, no. 6, pp. 3159–3173, 2008.

[203] F. Zhang, X. Zhang, K. Y. Sze, Y. Lian, and Y. Liu, "Incompressible material point method for free surface flow," *Journal of Computational Physics*, vol. 330, pp. 92 – 110, 2017.

[204] H. Zhang, K. Wang, and Z. Chen, "Material point method for dynamic analysis of saturated porous media under external contact/impact of solid bodies," *Computer Methods in Applied Mechanics and Engineering*, vol. 198, pp. 1456 – 1472, 2009.

[205] X. Zhang, K. Sze, and S. Ma, "An explicit material point finite element method for hyper-velocity impact," *International Journal for Numerical Methods in Engineering*, vol. 66, no. 4, pp. 689–706, 2006.

[206] Y. Zheng, F. Gao, H. Zhang, and M. Lu, "Improved convected particle domain interpolation method for coupled dynamic analysis of fully saturated porous media involving large deformation," *Computer Methods in Applied Mechanics and Engineering*, vol. 257, pp. 150–163, 2013.

[207] S. Zhou, J. Stormont, and Z. Chen, "Simulation of geomembrane response to settlement in landfills by using the material point method," *International Journal for Numerical and Analytical Methods in Geomechanics*, vol. 23, no. 15, pp. 1977–1994, 1999.